Characterization of the Imaging Performance of the Simultaneously Counting and Integrating X-ray Detector CIX

Dissertation

zur

Erlangung des Doktorgrades (Dr. rer. nat.)

der

Mathematisch-Naturwissenschaftlichen Fakultät

der

Rheinischen Friedrich-Wilhelms-Universität Bonn

vorgelegt von

Johannes Fink

aus

Neuwied

Bonn 2009

Angefertigt mit Genehmigung der Mathematisch-Naturwissenschaftlichen Fakultät der Rheinischen Friedrich-Wilhelms-Universität Bonn

1. Referent: Prof. Dr. N. Wermes
2. Referent: Prof. Dr. H. Schmieden.
Tag der Promotion: 23.10.2009
Erscheinungsjahr: 2010

Abstract

The CIX detector is a direct converting hybrid pixel detector designed for medical X-ray imaging applications. Its defining feature is the simultaneous operation of a photon counter as well as an integrator in every pixel cell. This novel approach offers a dynamic range of more than five orders of magnitude, as well as the ability to directly obtain the average photon energy from the measured data. Several CIX 0.2 ASICs have been successfully connected to CdTe, CdZnTe and Si sensors. These detector modules were tested with respect to the imaging performance of the simultaneously counting and integrating concept under X-ray irradiation. Apart from a characterization of the intrinsic benefits of the CIX concept, the sensor performance was also investigated. Here, the two parallel signal processing concepts offer valuable insights into material related effects like polarization and temporal response. The impact of interpixel coupling effects like charge-sharing, Compton scattering and X-ray fluorescence was evaluated through simulations and measurements.

Contents

1. Introduction . . . 5

2. X-ray imaging . . . 7
- 2.1 Fundamental principles of medical X-ray imaging . . . 7
  - 2.1.1 Photoelectric effect and X-ray fluorescence . . . 8
  - 2.1.2 Compton scattering . . . 9
- 2.2 Medical X-ray imaging techniques . . . 10
  - 2.2.1 Projection radiography . . . 10
  - 2.2.2 Computed tomography . . . 11
- 2.3 X-ray detector concepts . . . 13
- 2.4 Signal formation in direct converting pixel detectors . . . 16
- 2.5 Direct converting sensor materials . . . 19
  - 2.5.1 Silicon . . . 19
  - 2.5.2 CdTe and CdZnTe . . . 20
- 2.6 Additional considerations for hybrid pixel detectors . . . 26

3. CIX 0.2 detector . . . 29
- 3.1 Concept . . . 29
- 3.2 CIX 0.2 ASIC specifications . . . 29
- 3.3 CIX 0.2 pixel cell concept . . . 32
  - 3.3.1 Photon counter . . . 32
  - 3.3.2 Integrator . . . 34
  - 3.3.3 Feedback . . . 37
  - 3.3.4 Static leakage current compensation . . . 38
  - 3.3.5 Dynamic leakage current compensation . . . 39
  - 3.3.6 Issues with the leakage current compensation . . . 40
- 3.4 CIX 0.2 modules . . . 43
  - 3.4.1 Sensor overview . . . 43
  - 3.4.2 Module assembly . . . 44
  - 3.4.3 Module overview . . . 46
- 3.5 Chip periphery . . . 46

4. ASIC performance - Electrical tests on bumped CIX 0.2 modules . . . 49
- 4.1 Measurement conditions . . . 49
- 4.2 Calibration of the charge injection circuits . . . 49
  - 4.2.1 Current chopper . . . 49
  - 4.2.2 Bipolar switched capacitance chopper . . . 51
  - 4.2.3 Other charge injection circuits . . . 54
- 4.3 Dynamic range . . . 54
  - 4.3.1 Counter . . . 54
  - 4.3.2 Integrator . . . 59

4.4 Noise . . . 60
4.4.1 Counter . . . 60
4.4.2 Integrator . . . 62

5. CIX X-ray test setup . . . 67
5.1 X-ray tube . . . 67
5.2 X-Y stage . . . 68
5.3 Mechanical chopper . . . 68

6. Sensor material characterization . . . 71
6.1 Leakage current . . . 71
6.1.1 Bias dependence . . . 71
6.1.2 Temperature dependence . . . 73
6.1.3 Photon flux dependence . . . 74
6.2 Temporal response . . . 76
6.2.1 Long-term response . . . 77
6.2.2 Short-term response . . . 84
6.2.3 Concluding remarks on the temporal response . . . 85
6.3 Module homogeneity and lateral polarization . . . 85
6.3.1 Potential chip-based inhomogeneities . . . 85
6.3.2 Sensor-based inhomogeneities . . . 87
6.4 Spectroscopic performance . . . 91
6.4.1 ^{241}Am spectra . . . 91
6.4.2 Charge collection efficiency . . . 93
6.4.3 Tube spectra . . . 93

7. CIX module performance under X-ray irradiation . . . 97
7.1 Dynamic range . . . 97
7.1.1 Counter dynamic range . . . 99
7.1.2 Integrator dynamic range . . . 106
7.2 Noise . . . 107
7.2.1 Counter noise . . . 107
7.2.2 Integrator noise . . . 109
7.2.3 Noise correlations . . . 110
7.3 Average photon energy . . . 112

8. X-ray images . . . 117
8.1 Raw data and flatfield corrections . . . 117
8.2 Beam hardening . . . 119
8.3 Oversampling . . . 120
8.4 Average photon energy and contrast enhancement . . . 121

9. Conclusion and outlook . . . 127
9.1 Conclusion . . . 127
9.2 Outlook . . . 129

Appendix 131

A. Differential current logic . . . 133

B. CIX 0.2 readout 135

C. Threshold scans and tuning 137

Bibliography 139

Acknowledgements 142

1. Introduction

In high energy physics pixellated semiconductor detectors have evolved into a standard tool for the reconstruction of particle tracks. Owing to the small physical dimensions of the detector's pixel[1] cells, these detectors offer very high position resolutions. However, as standard high energy physics particle detectors are equipped with Si sensors, they suffer from a low X-ray absorption probability. Thus, alternative sensor materials are required in order to transfer the pixel detector concept into X-ray detection. In order to overcome this limitation, highly X-ray absorbing sensor materials like CdTe and CdZnTe are under research since the mid 1970's. Still, only recent years have seen a large increase in the availability as well as the material quality of these sensors, such that CdTe or CdZnTe based detectors can be realized.
Against this background, a new detector concept for medical X-ray imaging has been developed in a joint research effort by the University of Bonn, the University of Heidelberg and the Philips Research Laboratories Aachen. The main feature of this detector is that it combines two, currently alternatively used, signal processing concepts in every pixel cell. So far medical X-ray detectors have either integrated the photon flux or counted individual photons. The *Counting and Integrating X-ray detector* CIX applies both concepts simultaneously and is thereby able to draw upon the strengths of both concepts, while at the same time balancing their individual weaknesses. For example, CIX offers a larger dynamic range than conventional counting or integrating only detectors and it furthermore profits from the fact that it takes both measurements on one X-ray beam. These two simultaneous measurements allow a determination of the average photon energy of the recorded spectrum and therefore give a direct handle of the changes in the X-ray spectrum introduced by the imaged object.
After the electrical performance of the second generation CIX ASIC had been characterized in a different work [1], the aims of this work were the assembly of a full CIX X-ray detector and the assessment of the potential benefits of the simultaneously counting and integrating concept in combination with different Cd-based sensor materials. For this, a number of CIX ASICs were outfitted with semiconductor sensors. These modules were qualified with respect to the influence of the sensor on the electrical performance of the system, the quality of the semiconductor sensors and finally the imaging performance of the detector under X-ray irradiation.

[1] "picture element"

This work is structured as follows:

Chapter 2 - *X-ray imaging*
In this chapter the fundamental physical processes of X-ray matter interactions are described. Existing medical imaging techniques as well as currently available X-ray detector systems are presented. Furthermore, a special focus is placed on the description of direct converting hybrid pixel detectors including the underlying principles of the signal generation. At the end of this section some commonly used direct converting X-ray sensor materials are introduced.

Chapter 3 - *CIX detector concept*
The third chapter contains a detailed description of the CIX 0.2 detector system. After a motivation of the detector concept an overview over the ASIC is given. In the course of this discussion each basic building block of the CIX 0.2 pixel cell is addressed individually. This is followed by a description of the sensor side of the hybrid detector including the sensor design and the detector assembly. A final section covers the peripheral systems necessary for the operation of the ASIC.

Chapter 4 - *ASIC performance*
The electrical performance of the CIX 0.2 ASIC has been evaluated in detail in [1]. Nevertheless, with the addition of a direct converting sensor, key features of the electrical performance like dynamic range, linearity and noise are reevaluated on fully assembled detector modules.

Chapter 5 - *CIX X-ray test setup*
This chapter describes the measurement equipment, which was used to characterize the CIX 0.2 detector.

Chapter 6 - *Sensor material characterization*
The material characterization is one of the main aspects of this work as the detector performance depends crucially on that of the sensor material. This section therefore addresses the temporal response and the homogeneity of the different sensor types. The observed effects are qualified in terms of different models. Furthermore, the spectroscopic performance of the sensors is evaluated with the spectra of a radioactive source and an X-ray tube. A full simulation of the detector response including several sensor effects like X-ray fluorescence, Compton scattering and charge sharing concludes the discussion of the material quality.

Chapter 7 - *CIX module performance under X-ray irradiation*
While chapter 4 described the electrical performance of the assembled detector modules, this section evaluates the modules under X-ray irradiation. Topics like the dynamic range and the detector's noise are revisited. Finally, the average photon energy reconstruction is demonstrated.

Chapter 8 - *X-ray images*
At the end of this work, chapter 8 presents different X-ray images, which were taken with the CIX 0.2 system. These images illustrate the effects of two data correction methods on the raw detector data and they also investigate the potential benefits of the average photon energy measurement in terms of a contrast enhancement.

Some parts of this work were previously published in [2–5].

2. X-ray imaging

2.1 Fundamental principles of medical X-ray imaging

Since their discovery in December 1895 X-rays have turned into a major analytic tool for science and medicine. But even considering advancements like the invention of the computed tomography, the general principle of X-ray imaging remains unchanged since the days of Wilhelm Conrad Röntgen. It is based on the attenuation of an X-ray beam of intensity I_0 by the imaged object and the subsequent detection of the transmitted intensity I. This intensity reduction as a function of the absorption coefficient μ of the absorber is described by the Lambert-Beer law:

$$I = I_0 \cdot e^{-\int \mu(\vec{x}) d\vec{x}} \tag{2.1}$$

The underlying principles of photon-matter interactions are grouped into three basic processes: photoelectric or photo effect, Compton scattering and pair production. However, as photons above 250 keV are usually referred to as gamma rays, pair production with its minimum photon energy requirement of 1022 keV is excluded for X-rays. Hence, the total absorption coefficient for X-rays μ_{Tot} is given by a sum of the photoelectric and the Compton components:

$$\mu_{Tot} = \mu_P + \mu_C \tag{2.2}$$

Fig. 2.1 shows the absorption coefficients for Si and CdTe as a function of the X-ray energy.

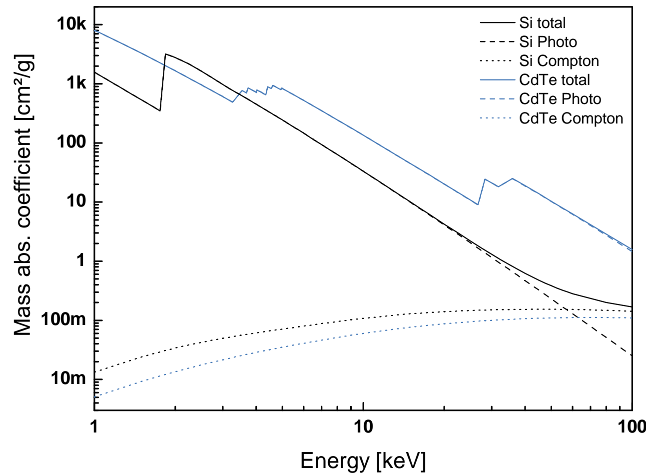

Fig. 2.1: Total mass absorption coefficients $\widetilde{\mu}_{Tot}$ for photons in Si and CdTe (solid lines) as a function of the photon energy [6]. According to its definition ($\widetilde{\mu} = \frac{\mu}{\rho}$), the mass absorption coefficient allows a comparison of different materials independent of their density ρ. The dashed lines show the photoelectric $\widetilde{\mu}_P$ and the dotted lines show the Compton $\widetilde{\mu}_C$ components. The characteristic lines of the atomic energy levels can be identified as bumps in the photoelectric absorption coefficient.

2.1.1 Photoelectric effect and X-ray fluorescence

At the lowest energies photons interact primarily through the photoelectric effect. In this interaction the absorbed photon transfers all its energy to the atomic shell. As a consequence, the atom is ionized and it emits a so called photoelectron, which carries away the energy difference $E_e = E_\gamma - E_{Ion}$ between the photon energy E_γ and the energy E_{Ion} necessary for the electron to leave its shell. The E_{Ion} minimum energy constraint means that, if the photon energy surpasses the binding energy of an individual electron state in the atomic shell, the cross section for the photoelectric effect exhibits a characteristic increase. The three, highest energetic steps are labeled K, L, M edge according to the atomic energy levels of the electrons.
The calculation of the photoelectric cross section σ and with it the photoelectric absorption coefficient μ_P is highly non-trivial. Therefore these two parameters are, for practical purposes, best obtained from empirical databases like [6].
Still, at energies larger than the K-edge of an atom and below the electron mass a non-relativistic approximation can achieve a good description of the photoelectric effect [7,8]:

$$\mu_P = \rho \frac{N_A}{A} \sigma_P \tag{2.3}$$

$$\sigma_P^{NR} = \sqrt{32}\alpha^4 \epsilon^{-3.5} Z^5 \frac{8\pi r_e^2}{3} f(\xi) \tag{2.4}$$

$$f(\xi) = 2\pi Z \alpha \sqrt{\frac{1}{2\epsilon}} \frac{exp(-4\xi arccot\xi)}{1 - exp(-2\pi\xi)} \tag{2.5}$$

$$\xi = \sqrt{\frac{\epsilon_K}{\epsilon - \epsilon_K}}; \quad \epsilon = \frac{E_\gamma}{m_e c^2}; \quad \epsilon_K = \frac{E_K}{m_e c^2} \tag{2.6}$$

This formula is based on the Born approximation including the correction factor f(ξ), which reflects the angular momentum transfer between photon and photoelectron. The remaining constants in (2.4) are the electron mass m_e, the classical electron radius r_e, the energy of the K-edge E_K and the fine structure constant α. Equation 2.4 furthermore shows that the photoelectric cross section σ_P^{NR} is dominated by the absorber's atomic number Z and the energy of the incident photon E_γ.
At high photon energies the cross section is described by the following equation [7]:

$$\sigma_P^{HR} = \frac{3}{2}\alpha^4 \frac{Z^5}{\epsilon} \frac{8\pi r_e^2}{3} \tag{2.7}$$

It is evident that in this highly relativistic case the cross section drops only with 1/E. However, note that in this energy regime the photon matter interactions are dominated by Compton scattering and pair production.
Following the interaction with the photon, the photoelectron subsequently deposits its kinetic energy inside the detector through inelastic collisions with electrons of neighboring atoms. In a semiconductor this can be described in terms of the band model, which means that in these collisions electrons are shifted from the valence band into the conduction band. However, as a considerable amount of the energy is transferred into crystal lattice vibrations (phonons) and finally into heat, the average electron-hole pair production energy is higher than the band gap energy.
As mentioned above, part of the photon's energy was used to ionize the atom which absorbed the photon. This means that a vacancy is created in the atomic shell and this vacancy is filled immediately with a free electron from the conduction band or a bound electron from the atom itself. During this relaxation process the excess energy can be

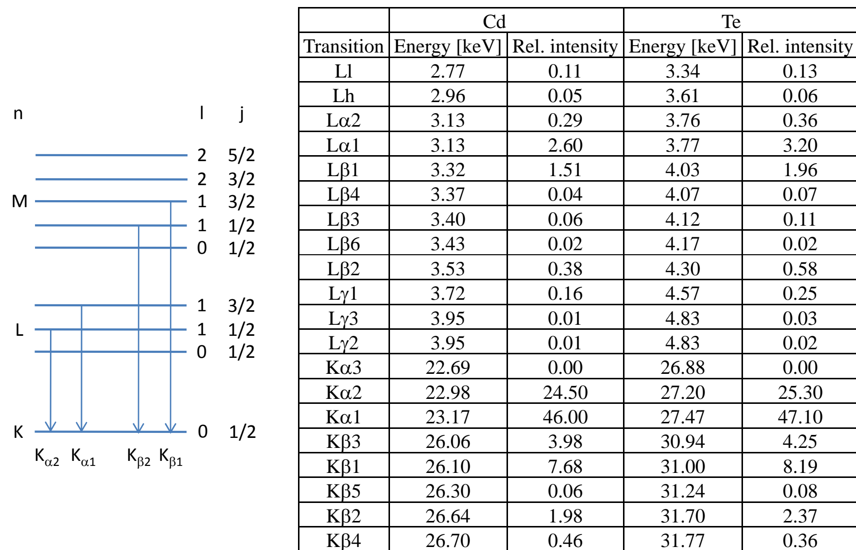

	Cd		Te	
Transition	Energy [keV]	Rel. intensity	Energy [keV]	Rel. intensity
Ll	2.77	0.11	3.34	0.13
Lh	2.96	0.05	3.61	0.06
Lα2	3.13	0.29	3.76	0.36
Lα1	3.13	2.60	3.77	3.20
Lβ1	3.32	1.51	4.03	1.96
Lβ4	3.37	0.04	4.07	0.07
Lβ3	3.40	0.06	4.12	0.11
Lβ6	3.43	0.02	4.17	0.02
Lβ2	3.53	0.38	4.30	0.58
Lγ1	3.72	0.16	4.57	0.25
Lγ3	3.95	0.01	4.83	0.03
Lγ2	3.95	0.01	4.83	0.02
Kα3	22.69	0.00	26.88	0.00
Kα2	22.98	24.50	27.20	25.30
Kα1	23.17	46.00	27.47	47.10
Kβ3	26.06	3.98	30.94	4.25
Kβ1	26.10	7.68	31.00	8.19
Kβ5	26.30	0.06	31.24	0.08
Kβ2	26.64	1.98	31.70	2.37
Kβ4	26.70	0.46	31.77	0.36

Fig. 2.2: Diagram of the inner atomic shell energy levels (left). Table of the most common X-ray fluorescence lines in Cd and Te in the energy range between 2 keV and 32 keV (right) [10]. The transitions are labeled in the format V_w with V detailing the final level and w the orbital number difference.

emitted via fluorescence photons, whose energy is determined by the atomic levels of the absorber material. Apart from X-ray fluorescence, atomic relaxation can also happen via the emission of an Auger electron. However, at atomic numbers above 60 the fluorescence yield is larger than 90 %, i.e. only 10 % of the relaxations happen through the Auger process [9]. Fig. 2.2 shows a schematic view of the innermost energy levels in the atomic shell in addition to a list of the highest energy X-ray transitions in Cd and Te.

2.1.2 Compton scattering

Compton scattering describes the inelastic scattering of an electron with a quasi-free atomic electron (see Fig. 2.3). In contrast to elastic or coherent scattering in which the photon only changes its direction, Compton scattering also changes the photon energy. The resulting photon energy $E_\gamma^{'}$ after the collision is determined by the scattering angle Θ of the outgoing photon with respect to the direction of the incident photon and can be

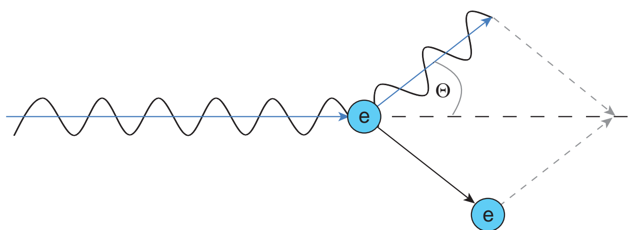

Fig. 2.3: Schematic view of Compton scattering. The incident photon is scattered inelastically off a loosely bound atomic electron. The energy transfer between photon and electron depends on the scattering angle Θ.

described by the following formula:

$$E'_\gamma = \frac{E_\gamma}{1 + \frac{E_\gamma}{m_e c^2}(1 - cos\Theta)} \tag{2.8}$$

A quantum mechanical calculation of the scattering process yields the cross-section σ_C for a photon to be scattered into the solid angle $d\Omega$. This equation is known as the Klein-Nishina formula [11].

$$\begin{aligned} \frac{d\sigma_C}{d\Omega} &= r_e^2 \left(\frac{1}{1 + \frac{E_\gamma}{m_e c^2}(1 - cos\Theta)} \right)^2 \left(\frac{1 + cos^2\Theta}{2} \right) \\ &\cdot \left(1 + \frac{\frac{E_\gamma}{m_e c^2}^2 (1 - cos\Theta)^2}{(1 + cos^2\Theta)(1 + \frac{E_\gamma}{m_e c^2}(1 - cos\Theta))} \right) \end{aligned} \tag{2.9}$$

The absorption of photons through the Compton effect, i.e. the removal of these photons from the incident beam, is then given by an integration of (2.9) over all angles.

$$\mu_C = \rho \frac{N_A}{A} Z \int \frac{d\sigma_C}{d\Omega} d\Omega \tag{2.10}$$

Note that (2.9) only describes the interaction with a single electron, such that (2.10) has to be multiplied by the atomic number Z, if the scattering off whole atoms is to be described.

2.2 Medical X-ray imaging techniques

At its beginning X-ray detection was solely based on photographic films. With the invention of new detector concepts, modern computers and the accompanying image enhancement capabilities new imaging techniques were developed. In general the existing imaging techniques can be divided into two categories.

2.2.1 Projection radiography

A classical X-ray image, as shown in Fig. 2.4(a), represents a two-dimensional intensity map of a three-dimensional object. The two-dimensional projection implies that the absorption coefficient μ is integrated along one axis. This is one of the essential problems of projection radiography. It means that, for example, a successful tumor identification can only happen if the contrast between the anomaly and the total integrated background of the patient's body is high. However, as illustrated in Tab. 2.1 the absorption coefficients of human tissue are rather similar. Considering the example of a chest image, the table shows that the absorption coefficients of breast tissue, lung tissue and muscle at 60 keV photon energy vary only by less than one percent. One solution for the low contrast problem is the administration of a contrast agent with a high atomic number like iodine ($Z = 53$), which accumulates in certain regions and thus enhances the image contrast. This technology is called angiography and is mainly used for the imaging of perfused body sections like blood vessels and the heart.

A photograph of a modern projection imager can be found in Fig. 2.4(b). Here, tube and detector are mounted along one axis, which can be moved horizontally and vertically when imaging different sections of a patient's body. In order to improve the image quality such systems are often equipped with a beam collimator close to the X-ray tube and an anti-scatter grid above the detector. The anti-scatter grid consists of a metal collimator, which eliminates X-rays that enter the detector at an angle, i.e. X-rays that were scattered by the object itself and therefore degrade the image contrast.

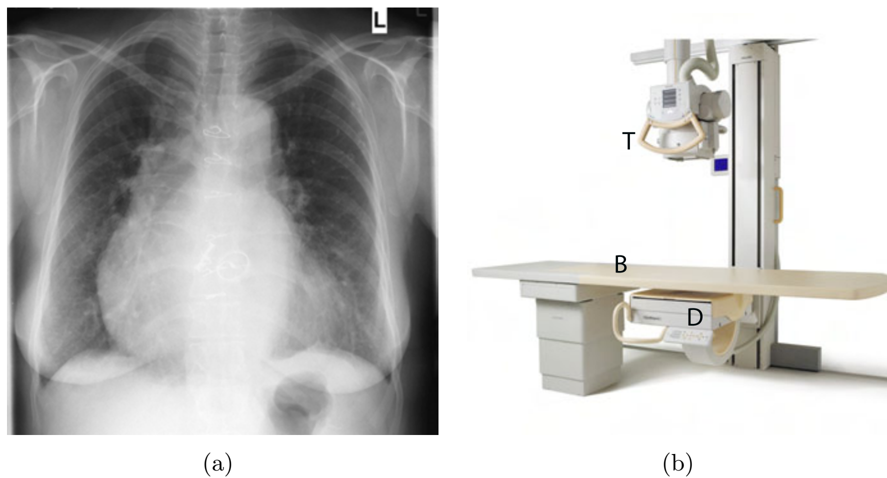

(a) (b)

Fig. 2.4: (a): Projection radiography image of a human chest (taken with Philips Digital Diagnost) [12].
(b): Photograph of a 2D projection radiography imager (Philips Digital Diagnost). The picture shows the X-ray tube (T), the patient bed (B) and the detector (D) [12].

Material	Mean atomic number	Mass absorption coeff. [cm^2/g]	Density [g/cm^3]	Absorption coeff. [cm^{-1}]
Air, dry	8	0.1875	0.0012	0.0002
Aluminum	13	0.2778	2.699	0.7498
Brain	8	0.2058	1.040	0.2140
Breast tissue	7	0.2006	1.020	0.2046
Bone	10	0.3148	1.920	0.6044
Fat	7	0.1974	0.950	0.1875
Lung tissue	7	0.2053	1.050	0.2156
Muscle	8	0.2048	1.050	0.2150
Plastic	6	0.1924	1.190	0.2290
Water	8	0.2059	1.000	0.2059

Tab. 2.1: Absorption properties of various substances commonly found in medical imaging at a photon energy of 60 keV. The table also contains substances like aluminum and plastic as their absorption properties are similar to human tissue. Hence, these materials allow a convenient testing of imaging systems under laboratory conditions.

2.2.2 Computed tomography

A more general way of dealing with the limitations of classical radiography is a full three-dimensional reconstruction of the object with a computed tomography (CT) scanner. Such an imaging system acquires many views of the object under different angles and then computes a three-dimensional representation built from three-dimensional volume elements, called voxels. The voxelized map of the absorption coefficients makes for a greatly improved image quality as even low-contrast regions can be distinguished from the background. An example of this can be found in Fig. 2.5(a), which shows a CT image of the human heart.
In a modern CT scanner (see Fig. 2.5(b)) detector and X-ray source are mounted on opposite sides of a quickly rotating (typ. 3 Hz) gantry. In order to increase the imaged section of the patient the tube emits a cone-shaped X-ray beam, which hits several identical

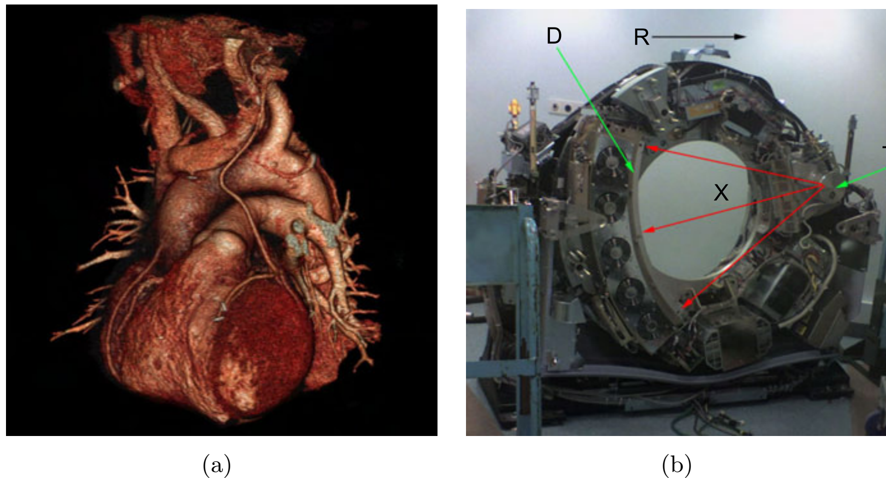

(a) (b)

Fig. 2.5: (a): CT image of a human heart including the coronary artery (taken with Philips Brilliance CT 40-channel) [14]. (b): Photograph of an open CT gantry. The picture shows the X-ray tube (T), the detector banana (D) and the fan-shaped X-ray beam (X). The direction of rotation is also indicated (R) [15].

detector rows (currently up to 256 slices [13]) placed next to each other. Furthermore, the patient is moved slowly through the center of the gantry resulting in a helical motion of the detector-tube assembly. Like this it is possible to acquire large volume scans of the patient at a time-scale of seconds, keeping motion artifacts, e.g. respiratory motion, to a minimum.
However, this increased resolution comes at the cost of a significantly increased dose. A typical chest CT scan exposes the patient to approximately 8 mSv compared to the 0.02 mSv of conventional two-dimensional chest projection image [16]. In comparison, the accumulated average yearly dose including natural as well as anthropogenic sources is about 2.14 mSv. These dose considerations have a major impact on the quality of medical X-ray examinations because they directly affect the achievable image contrast. It can be shown that the X-ray dose necessary to obtain a given contrast and signal to noise ratio for a quadratic object placed in front of a homogeneous background is inversely proportional to the squared area of that object [16]. Therefore the design goal of any X-ray imaging system is always to find a balance between the lowest possible patient dose and the minimum image contrast necessary to identify anomalies in the human body.
The specifications of different medical X-ray imaging modalities in Tab. 2.2 reflect these dose and image contrast considerations in terms of the average photon flux and the typical energies of the X-rays. The table illustrates that mammography systems for example need only to count $5 \cdot 10^7$ photons/(mm^{2}s) at relatively low energies below 40 keV. In contrast to the static image acquisition of the mammography system, a CT imager has to acquire its single scans in rapid succession due to the quickly revolving gantry. This results in photon fluxes which are typically 20 times higher. Furthermore, in order to penetrate the thicker and denser objects a CT scanner is operating at higher X-ray energies compared to a mammography imager.
Regardless of the rate considerations, the demand for high resolution projection images in mammography requires typical pixel sizes smaller than 100 μm, whereas the three dimensional reconstruction algorithm allows modern CT scanners to operate with 1 mm pixels.

	Mammography	General X-ray radiography	Computed Tomography
Count rate (photons/(mm^2·s))	$5 \cdot 10^7$	10^6 to $5 \cdot 10^8$	typ. 10^9
Equiv. current per pixel (nA)	0.2	0.03 - 20	2000
Pixel size (μm)	typ. 85	typ. 150	typ. 1000
Detector area (m^2)	0.072	0.12	0.14 (128 slices)
Highest energy (kVp)	28 - 40	70 - 120	80 - 140

Tab. 2.2: Typical requirements of different X-ray imaging applications [4]. Tube energies given in kVp refer to the acceleration voltage of the X-ray tube. This value sets the upper boundary for the photon energies in the generated X-ray spectrum. Typical tube settings: Mammography: 28 kVp, 144 mA, 65 cm; Radiography: 70 - 120 kVp, 2 - 300 mA, 1.5 m; Tomography: 140 kVp, 400 mA, 1.04 m, including filters.

2.3 X-ray detector concepts

Medical X-ray detectors have diversified into a number of different concepts. The selection of a particular type of detector for a special application like mammography, dental imaging or computed tomography is influenced by essential features like photon detection efficiency, image noise and real time capability. Nevertheless other aspects like the price of the imager and the ease of use have to be considered as well.

Photographic film

The earliest detector concept, which is still widely used, is the X-ray sensitive photographic film. These relatively cheap and easy to handle detectors are based on the darkening of a X-ray sensitive emulsion, which is applied to a base carrier. X-ray images are obtained through chemical processing of the films, which also prevents real time imaging with these detectors. Although the quantum detection efficiency of photographic film is only on the order of a few percent, very high spatial resolutions (μm) can be achieved by using fine grained emulsions. For reduced patient exposure it is possible to increase the X-ray sensitivity of the film by placing a thin scintillator foil on top of it. This however reduces the spatial resolution of the detectors. Apart from the lacking real time capability, the major drawback of photographic films is their non-linear response characteristic, i.e. the detectors are prone to suffer from under- and over-exposure. Typical dynamic ranges are on the order 40 dB [17].

Image intensifiers

Image intensifiers are real-time imaging devices in which incident X-rays are converted first into visible light with the help of a scintillating material. A commonly used substance is CsI, which can be grown in columnar structures that effectively guide the generated optical photons onto a photocathode. This second conversion layer is placed directly on top of the scintillator and converts the incoming photons into electrons. The following amplification stage accelerates the electrons onto a small anode target, which converts the

electrons back into optical light. Finally, a CCD[1] camera records the resulting image. Essential benefits of this imaging concept are real-time capability and dose reduction due to the amplification stage, which greatly increases the optical light yield by up to a factor of 10^4 [16].

Indirect conversion flat panel imagers

Indirect conversion flat panel imagers evolved from image intensifiers. The initial X-ray detection is again based on the conversion of X-rays into optical light through a scintillator material. However, instead of the bulky electron optics of the amplification stage indirect conversion flat panel imagers use semiconductor detectors. In these detectors segmented photodiodes register the light intensity and thereby allow a position sensitive measurement of the incident X-rays (see Fig. 2.6). The name indirect conversion detectors is a reference to the intermediary step, which is necessary to transform X-rays into electrical signals. Modern flat panel imagers use compact, anorganic scintillator materials like gadolinium oxysulphide (GOS) and bismuth germanate (BGO) in order to achieve an optimum between light yield and signal decay times. An overview of common scintillator materials and their properties can be found in Tab. 2.3. Note that the response time of a scintillator is in general influenced by two effects. The first time constant is the decay time of the excited electron states, which are activated in the photon-matter interaction. This determines how fast the signals are generated after an X-ray photon has interacted with the sensor. The second effect, that has to be considered, is the signal generation due to the delayed release of charge carriers from defect states. As this second effect usually happens on much longer time scales compared to the regular deexcitation, scintillator detectors are known to show a phosphorescent behavior. This effect is also called afterglow.
Compared to image intensifiers, flat panel devices offer a reduced thickness, higher X-ray sensitivity and an increased dynamic range.

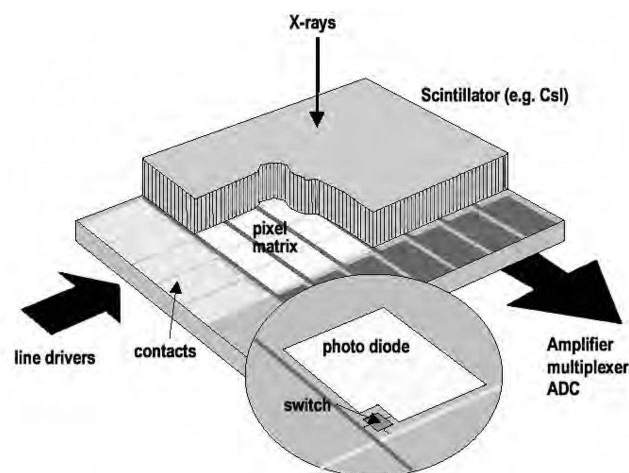

Fig. 2.6: Schematic view of an indirect flat panel detector [18]. Impinging X-rays are converted into visible light (e.g. 550 nm in CsI). The columnar structure of the CsI crystals then acts as a light guide towards the active pixel matrix. During readout individual pixels are connected to the readout chain by means of thin-film-transistors (TFT) located in the picture elements. In this example the high ohmic switches are controlled by the line drivers, which are connected to bond pads in the lower left corner of the figure.

[1]"Charge coupled device"

	CsI:Tl	GOS	BGO
Peak emission [nm]	550	510	480
Photons/keV	52	42	8.5
Decay time [μs]	1	3	0.3
After glow % after 100 ms	0.3	<0.01	<0.01

Tab. 2.3: Properties of different scintillators [19, 20].

Direct conversion flat panel imagers

Unlike scintillator-based flat panel imagers, direct converting flat panel imagers use a sensor material, which directly converts absorbed X-rays into electrical signals. One such direct converting sensor material is amorphous selenium (a-Se). In X-ray detectors a-Se is typically evaporated onto a segmented arrays of TFTs[2], which reads out the sensor signals [21,22]. This way it is possible to cover a larger active area compared to crystalline sensor materials. Amorphous Se generates about 20 electron-hole pairs per 1 keV photon and therefore offers signal-to-noise ratios comparable to those of scintillator based flat panel imagers [23].
An alternative imager concept, which is currently under research in medical X-ray imaging, is the hybrid pixel detector. A hybrid pixel detector consists of a direct converting sensor and a separate readout chip (see Fig. 2.7). Both the sensor surface and the readout electronics are segmented into so-called pixel cells, which are connected by small solder balls, i.e. the bump bonds. The sandwich-like structure of sensor and chip gives the concept its name. Initially hybrid pixel detectors were mainly outfitted with Si sensors

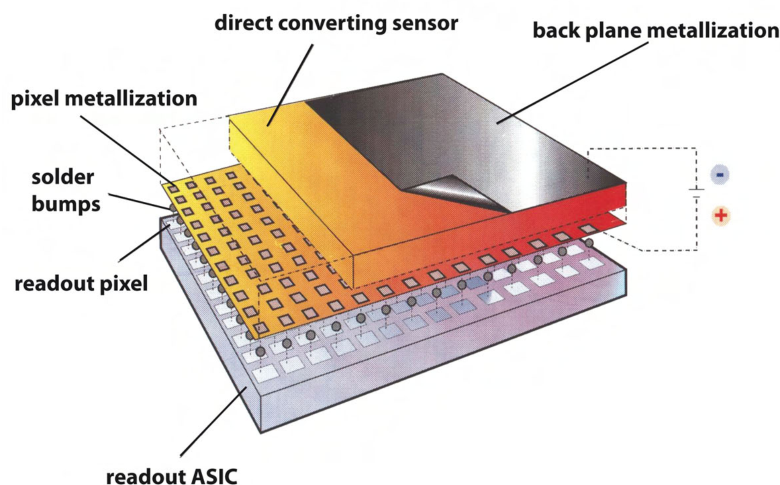

Fig. 2.7: Schematic edge-on view of a hybrid pixel detector. Impinging X-rays are converted into moving electric charges inside the sensor material. Solder bumps with typical dimensions between only a few micrometers and several dozen micrometers connect one pixel electrode on the sensor side with one readout cell on the ASIC. Unlike flat panel imagers, which are based on the transmission of light in the sensor, hybrid pixel detectors require a potential difference across the sensor material to guide the generated electric charges toward the pixel electrodes.

[2]"Thin-film-transistor"

and were used in high energy physics experiments to register the passage of high energetic particles. The low X-ray absorption of the Si sensors makes the detection of X-rays difficult. However, due to the increased availability of highly absorbing sensor materials like CdTe, CdZnTe and GaAs X-ray imaging with hybrid pixel detectors becomes a viable concept. Compared to indirect converting flat panel detectors, hybrid pixel detectors have the big advantage that instead of producing a few photons per keV of absorbed energy, direct converting semiconductor sensors produce several hundred electron-hole pairs per keV, e.g. 280 per 1 keV in Si. This translates into a superior signal-to-noise ratio. Furthermore, the columnar structure of the scintillation detectors limits the effective pixel size in these detectors, whereas hybrid pixel detectors can reach pixel sizes on the order of 50 $\mu\mathrm{m}^2$ [24] allowing higher spatial resolutions. An additional advantage of hybrid pixel detectors is their capability of counting single X-ray photons. More information on the photon counting concept will be given in section 3.1.
Recently a number of direct-converting detector demonstrator systems for X-ray imaging have been introduced [25–27].

2.4 Signal formation in direct converting pixel detectors

In general, the signal formation in a direct converting pixel detector can be described by a two step process. First the photons create electron-hole pairs inside the sensor material via the photon-matter interactions described in section 2.1. The second stage of the signal formation is based on the movement of the charge carriers in the electric field of the sensor. If no further steps are taken, the electron-hole pairs that were created by the incident photon recombine and the signal charge is lost. This mutual recombination can be avoided by supplying the direct converting sensor with an external bias voltage. The electric field separates the electrons and holes immediately after their generation and guides them towards the readout electrodes. For the typically 10,000 electron-hole pairs created by the absorption of an X-ray photon the charge carrier movement and thereby the signal formation starts instantaneously. Note that in the case of heavy charged particles like α-particles, the shielding effect of the dense charge cloud (typically 10^6 electron-hole pairs) can delay the charge carrier movement for several nanoseconds [2].
An important feature of the signal generation is that it starts immediately once the generated charge carriers begin to move. According to Gauss's law, the introduction of charge carriers into the detector volume changes the electric field inside the sensor. The change of the electric field in turn induces mirror charges at the detector electrodes, whose magnitude changes as the charge carriers travel through the sensor volume. This time-dependent change of the mirror charges at the detector electrodes then constitutes the sensor current signal, which is processed by the readout chip.

Ramo's theorem

The mathematical treatment of the signal formation is given by the Ramo-Shockley theorem [28]. It describes the current signal $i(t)$ at a detector electrode based on the motion of the electron charge q_e and the hole charge q_h in the detector's electric field.

$$i(t) = q_e \vec{v_e} \vec{E_w} + q_h \vec{v_h} \vec{E_w} \tag{2.11}$$

The weighting field $\vec{E_w}$ is a mathematical tool that represents the coupling of the charge carrier movement to a given electrode. It should not be confused with the electric field $\vec{E}$ which determines the velocity via the charge carrier mobilities μ_e and μ_h [29].

$$\vec{v} = \mu_{e/h} \vec{E} \tag{2.12}$$

In most cases the upper limit of the charge collection time for a detector of thickness D at a bias V can be estimated by the following formula.

$$t_{e/h} = \frac{D^2}{\mu_{e/h} \cdot V} \tag{2.13}$$

The formula neglects sensor effects like the build-up of space charge, which can cause large deviations of the electric field from the externally applied one. Still, typical charge collection times in thin Si detectors (300 μm at 100 V) are on the order of 3 ns for electrons and 9 ns for holes. Thicker CdZnTe sensors typically have transit times on the order of several dozen nanoseconds.

Parallel plate detector

Fig. 2.8(a) shows the signal generation for a parallel plate detector under the assumptions of a constant electric field and an electron mobility, which is three times higher than the respective value for holes. In this particular detector geometry the weighting field is constant as indicated by the evenly spaced equipotential lines in Fig. 2.8(a). If a photon creates a number of electron hole pairs right in the middle of this detector, the resulting mirror charge $Q(t)$ at the cathode has a quickly rising electron and a slowly rising hole component (see Fig 2.8(a) middle). The current flowing through the anode is shown in the bottom left plot in Fig 2.8(a) and it consists of a short-lived but strong electron

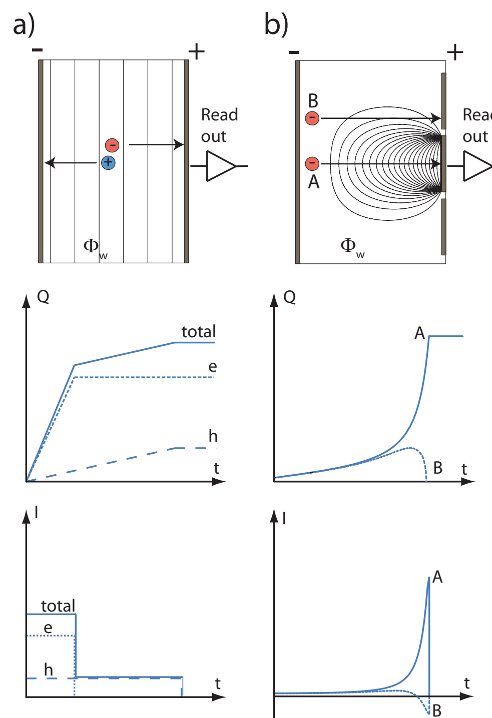

Fig. 2.8: Weighting potential (top), induced mirror charge Q(t) (middle) and generated signal current i(t) (bottom) in a parallel plate detector (a) and a pixel detector (b). Both (a) and (b) assume a constant electric field inside the sensor. The three images in (a) illustrate the different duration and magnitude of the electron and hole components of the sensor signal, if the charge carriers are created in the middle between the detector electrodes. (b) shows the small pixel effect using the example of two different electron trajectories through the detector. In this case hole signals are neglected.

component and a smaller, longer lasting hole component. The difference in the electron and hole components of the signal can be explained by Ramo's theorem (2.11). The high mobility of the electrons causes them to quickly travel through the detector inducing a rapidly changing charge at the anode. As the holes progress more slowly, the hole signal lasts longer but at the same time has a smaller amplitude. Overall, the charge collection is complete once the carriers arrive at the respective electrodes. Note that this example treats only the signals at the anode. Still, it is evident that a negative charge, which moves away from the cathode, is equal to a positive charge moving closer to said electrode. Hence, the signal can be observed at both sides of the detector with the sole difference of inverted polarities. However, this is only true if no charge is lost inside the sensor and if the charges are created right in the middle of the sensor. In case the electron-hole pairs are not created in the middle of the sensor volume, the electron and hole components contribute to the constant total collected charge according to their distance of travel.

Pixel detector

In contrast to this simple example, a special situation arises for pixel detectors in which the pixel dimensions are small compared to the sensor thickness. Fig. 2.8(b) illustrates the so-called *small-pixel effect* in one dimension. The weighting potential is given by the following formula [29]:

$$\Phi_w = \frac{1}{\pi} arctan\left(\frac{sin(\pi y)sinh(\pi \frac{a}{2})}{cosh(\pi x) - cos(\pi y)cosh(\pi \frac{a}{2})}\right) \tag{2.14}$$

The x coordinate gives the position in the anode plane and the y coordinate parameterizes the distance from the anode. The thickness of the sensor is set to one and the width of the anode pixel electrodes is given by the constant a. In this example the starting point of the charge carrier movement is chosen close to the cathode, so that only the electrons have a significant contribution to the signals. Holes reach their collecting electrode almost instantly and thus induce only a negligible signal on the anode. Fig. 2.8(b) shows the induced signals for two different paths through the detector. One electron (A) is generated directly above the central read-out pixel and the second (B) starts its translation above the neighboring electrode. At the starting point of both movements the weighting field of the central electrode is weak. Therefore the induced charge and the current signals increase only slowly as the carriers move towards the anode. At the end of the charge carrier movement, when electron A approaches the central pixel, the steep increase in the weighting potential causes a strong coupling of the movement to this particular electrode. The figure also illustrates that the weighting potential of the central pixel extends into the space above the neighboring pixels. This means that a charge carrier movement towards a neighboring electrode (electron B) also induces a current signal on the central electrode. As shown, the signal from electron B does not differ from that of electron A during the initial phase of the charge carrier movement. Nevertheless, once electron B approaches its collecting pixel the sign of the current signal is inverted and the induced charge on the central electrode returns to zero.
In summary this means that due to the small pixel effect the largest part of the signal is generated when the charge carriers are close to the pixel electrodes, e.g. at a 250 μm electrode on a 3 mm thick sensor 90 % of the charge is collected in only 40 % of the charge carrier's transit time. Furthermore, only charges that are collected at the read-out electrode yield a net charge signal.

2.5 Direct converting sensor materials

The selection of the direct converting sensor material plays an important role on the detector performance. Therefore this section will introduce three different sensor materials, which were used in this work. A special focus will be placed on the discussion of material related effects.

2.5.1 Silicon

Silicon is a widely used and well understood elementary semiconductor material. This and the lack of unwanted material effects make it a very good reference for the testing of hybrid pixel detector concepts.
Concerning its physical properties, Si is a tetravalent metalloid with an atomic number of 14, i.e. it is situated in the carbon group of the periodic table of elements. In its crystalline form Si is arranged in a face-centered cubic lattice with the base $\left[(0,0,0),(^1/_4,^1/_4,^1/_4)\right]$. This structure is also called a diamond lattice. The relevant material properties of Si are given in Tab. 2.4. At room temperature the free charge carrier density in high purity Si is approximately 10^{10} cm^3. Compared to the other sensor materials in Tab. 2.4 this constitutes a relatively low resistance, which is also the reason why Si sensors have to be doped. In the doping process elements with three (p-dopant e.g. In) and five (n-dopant e.g. As) valence electrons are implanted into the Si crystal, resulting in additional acceptor (p-dopant) and donator (n-dopant) energy levels in the band gap. The combination of such p- and n-doped zones then establishes a p-n junction whose schematic representation is shown in Fig. 2.9. The major feature of this junction is the depletion zone, which is created by the diffusion of majority carriers from one zone into the oppositely doped region. In this context, the term majority carriers refers to electrons in the n-doped zone and holes in the p-doped zone. The diffusion of the charge carriers causes the build-up of a positive space charge inside the n-type Si and a negative space charge in the p-type section. This introduces an electric field, which counteracts the diffusion process and thus causes a thermal equilibrium across the junction. Fig. 2.9(b) gives a schematic view of the space charge distribution with N_A (p-type) and N_D (n-type) describing the acceptor and

Element	Si	CdTe	CZT
Atomic number Z	14	48,52	48,30,52
Average Z	14	50	49.1
Density [g/cm^3]	2.33	5.85	5.78
Band gap [eV]	1.12	1.50	1.57
e^- - h^+ creation energy [eV]	3.61	4.43	4.64
Typ. resistance [Ωcm]	$2.3 \cdot 10^5$	10^9	$>10^{10}$
Radiation length X_0 [cm]	9.36	1.52	1.52
Dielectric constant [As/Vm]	11.7	11	10.9
Mobility e^- [cm^2/Vs]	1400	1000	1000-1300
Mobility h^+ [cm^2/Vs]	480	100	50-80
Average lifetime e^- [s]	10^{-3}	$3 \cdot 10^{-6}$	$3 \cdot 10^{-6}$
Average lifetime h^+ [s]	$2 \cdot 10^{-3}$	$2 \cdot 10^{-6}$	10^{-6}
$\mu\tau$ e^- [cm^2/V]	1.4	$3.3 \cdot 10^{-3}$	$(3-5) \cdot 10^{-3}$
$\mu\tau$ h^+ [cm^2/V]	1	$2 \cdot 10^{-4}$	$5 \cdot 10^{-5}$

Tab. 2.4: Material constants of Si, CdTe and CdZnTe.

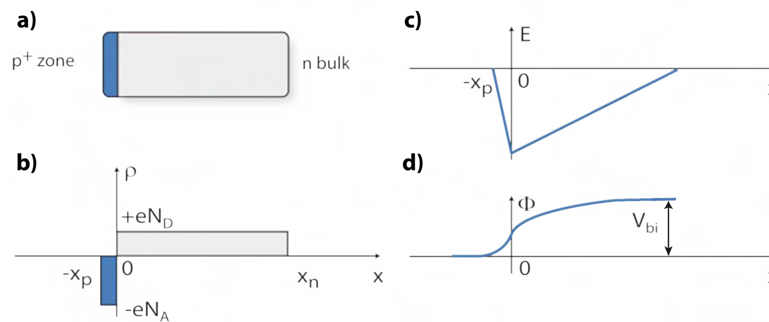

Fig. 2.9: The p-n junction. a) Schematic view. b) Space charge distribution with acceptor density N_A, donator density N_D, depletion widths x_p and x_n. c) Electric field profile. d) Electrostatic potential.

donator densities and x_p and x_n detailing the lateral dimensions of the depletion zone. The resulting electric field profile and electrostatic potential at the p-n junction are shown in Figs. 2.9(c) and 2.9(d), respectively. Within the depletion zone the number of free charge carriers is reduced by several orders of magnitude compared to intrinsic Si. Thus electron hole pairs created in a photon-matter interaction can be effectively separated before they recombine.

2.5.2 CdTe and CdZnTe

Cadmium-Telluride (CdTe) and Cadmium-Zinc-Telluride (CdZnTe or CZT) are compound II-VI semiconductor materials with a high atomic number and a relatively high density. The crystals are arranged as a combination of two face-centered cubic lattices shifted by a Miller index of $(^1/_4, {}^1/_4, {}^1/_4)$ which constitutes a so-called zincblende structure. Compared to Si the band gap energy is larger and therefore the intrinsic resistivity of CdTe and CdZnTe is higher. This makes the doping of p-n structures unnecessary. Nevertheless, the more complex crystal growth of the compound material reduces the crystal quality as lattice defects are a major issue in CdTe and CdZnTe. Two very common crystal defects are the Cd vacancy (V_{Cd}) and the Te substitution defect (Te_{Cd}). Considering the band gap model, V_{Cd} acts as an acceptor state due to the missing electrons from the Cd-atom. Likewise, the excess electrons of a Te_{Cd} mark this substitution defect as a donor. Hence, both defect states introduce additional energy levels between valence and conduction band

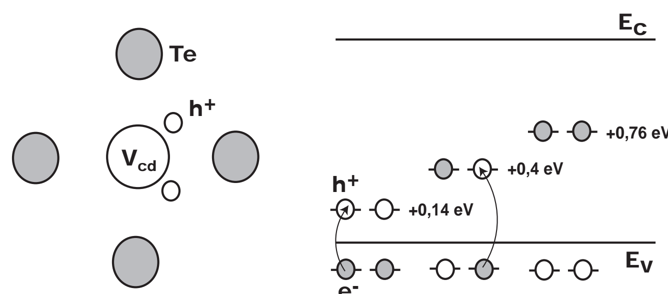

Fig. 2.10: Schematic representation of a Cd vacancy defect V_{Cd} surrounded by Te atoms. The defect introduces an acceptor state close to the valence band, which can be filled by electrons. In this process the simultaneously generated holes in the valence band increase the hole conductivity of the sample.

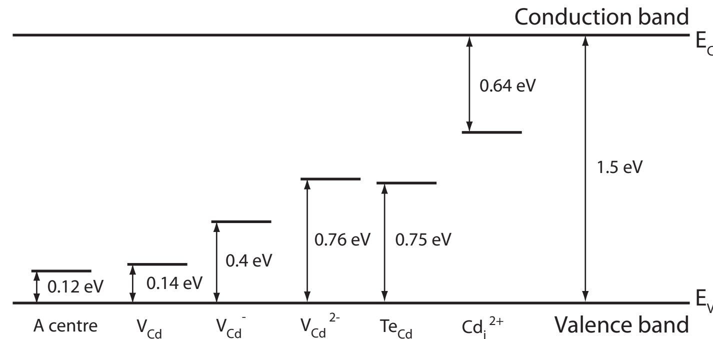

Fig. 2.11: Energy band diagram of CdTe in [eV] including some common trap levels. V_{Cd} stands for a Cd vacancy and Te_{Cd} stands for a Te interstitial defect. The figure is taken from [36].

and thereby reduce the resistivity of the crystal.
Fig. 2.10 illustrates this for a V_{Cd}. In this case electrons from the valence band can be transferred into the acceptor state. This leaves a hole in the valance band and thus the hole conductivity of the sample is increased. In order to balance the defect induced low resistivity of the CdTe samples, they are typically doped with Cl atoms whose unbound valence electrons compensate the acceptor states introduced by the V_{Cd} defects. A schematic representation of the energy levels of some atomic defect levels in CdTe is given in Fig. 2.11.
A different situation arises for CdZnTe. These ternary compound crystals are usually grown at Zn-Te ratios of 10 % Zn and 90 % Te, which increases the band gap of the material and thereby reduces the conductivity by roughly a factor of 10. An additional compensation like in the CdTe samples is therefore not necessary. Nevertheless, it has been shown [30] that the Zn concentration has a significant impact on the conductivity of the material. The authors of this paper argue that a high Zn concentration reduces the Te_{Cd} (donator) concentration and thus increases the importance of the V_{Cd} defects (acceptors). Hence, the Zn concentration effectively determines wether a sample exhibits a weakly n-doped (< 7 % Zn) or a p-doped behavior (> 7 % Zn).
In addition to the lattice defects the charge carrier transport and the charge collection efficiency is also affected by macroscopic effects like grain boundaries [31], prismatic punch dislocations [32] and Te-inclusions [33].
Standard manufacturing processes for CdTe and CdZnTe are the traveling-heater method (THM) [34] in addition to the high pressure and the vertical Bridgman methods (HPB and VBM) [35].

Metal contacts

Metal-semiconductor interfaces play a crucial role in the resistive behavior of the sensor material. Depending on the work function $e\Phi_m$ of the metal and the electron affinity $e\chi$ of the semiconductor an ohmic or a diode-like (Schottky-contact) current voltage characteristic is observed. In CdTe the electron affinity is 3.35 eV and for a common electrode material like Au or Pt the work functions are 5.1 eV or 5.8 eV, respectively. If these materials are brought into contact, charge carriers move from the metal into the semiconductor and introduce a space charge close to the electrode. This space charge causes a

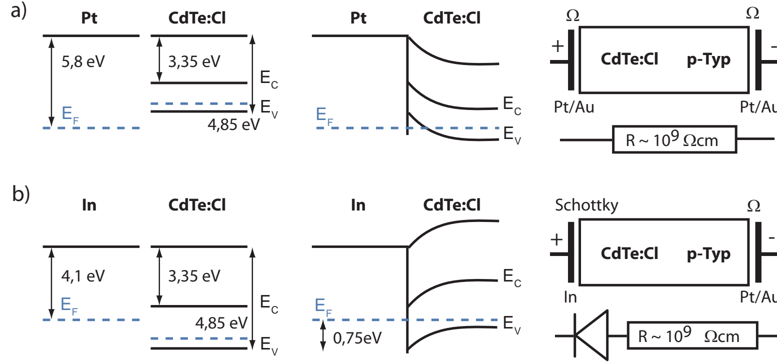

Fig. 2.12: Formation of ohmic (a) and Schottky (b) contacts in Cl-compensated CdTe. The leftmost plots show a band diagram representation of the valence band E_V, the conduction band E_C and the Fermi level E_F in the materials. The band bending, which happens if semiconductor and metal are brought into contact, is shown in the two plots in the middle. The two rightmost plots show the equivalent circuit diagram of the resulting metal semiconductor contacts.

bending of the energy levels in the band gap model as detailed in Fig. 2.12. For a weakly p-doped, Cl-compensated CdTe detector this means that the majority carriers (holes) do not experience a potential barrier at the metal-semiconductor interface. Thus, an ohmic contact is established. This can be changed if the Pt or Au contact is replaced with In. Due to the very low work function of In (4.1 eV), a potential barrier is created, which acts as a rectifying junction. When applying a reverse bias this reduces the leakage current through the detector and increases the resistivity of the device by roughly a factor of 10 to a total of approximately 10^{10} Ωcm [37]. A positive potential at the In contact with respect to the CdTe bulk material enhances the height of the potential barrier.

Charge carrier trapping

The introduction of defect levels in the band gap of a semiconductor has direct consequences for the signal generation in these detectors as charge carriers can be trapped in the defect levels. Depending on the position of the levels in the band gap, shallow and deep traps are distinguished.
Shallow traps lie close to the valence or conduction band and although their trapping probability is high due to the low potential difference, their detrapping probability is equally high for the same reasons. This means that charge carriers stay only for a short time (some ns) in these traps, which reduces the overall carrier mobility due to the constant trapping and detrapping.
Deep traps have a larger impact on the signals coming from the sensor as the charges stay considerably longer (some 100 ns up to μs) in these traps. This way the charges are generally lost for the current pulse in which they were originally created and the charge collection efficiency of the sensor is reduced. Assuming a simple case of a detector with a constant electric field and neglecting the additional charge loss due to electron-hole recombination, these trapping losses can be parameterized in terms of the total number of free charge carriers $N(t)$ [38].

$$\frac{N(t)}{N_0} = \frac{1}{\tau_T + \tau_D} \cdot \left[\tau_T + \tau_D \cdot exp\left(-\frac{(\tau_T + \tau_D) \cdot t}{\tau_T \cdot \tau_D} \right) \right] \tag{2.15}$$

Note that N_0 is the total number of electrons or holes that are created in the photon sensor interaction. τ_T is the trapping time and τ_D the detrapping time.

An additional effect of the deep traps is that the continuous detrapping causes a current to flow through the detector, which is only weakly related to the momentary absorption of X-rays. This can be observed after the X-ray irradiation of the detector is stopped because then the detrapping current manifests itself in an exponentially decaying afterglow signal. The term afterglow is adapted from the phosphorescence of scintillators at the end of an irradiation period.

Charge carrier mobility

Fig. 2.13 shows the average electron and hole mobilities in different Si, CdTe and CdZnTe samples as a function of the electric field. The values were obtained with the transient current technique (TCT). This method is based on the analysis of individual current pulses generated in a direct converting semiconductor sensor under irradiation with a pulsed laser beam or a radioactive α-particle source [2,3]. The measurements shown in Fig. 2.13 were obtained using α-particles from a ^{241}Am source with an energy of 3.9 MeV. The short penetration depth of 10-20 μm of these particles guarantees that the charge carrier cloud is generated close to the irradiated electrode. Therefore, as described in section 2.4, the resulting current signals are always based on the movement of only one type of charge carriers, i.e. electrons or holes. For the further analysis these current pulses are amplified by a 2 GHz amplifier (Miteq AM-1607-2000) and recorded with a fast digital oscilloscope (Tektronix TDS5140B).
The following equation is used to calculate the charge carrier mobilities in Si [39].

$$\mu_{Si} = \frac{D^2}{2 \cdot t_{Drift} \cdot V_{FD}} \cdot ln \left[\frac{V + V_{FD}}{V - V_{FD}} \cdot \left(1 - \frac{x_0}{D} \frac{2V_{FD}}{V + V_{FD}} \right) \right] \tag{2.16}$$

V_{FD} parameterizes the full depletion voltage of the Si p-n diodes (here 96 V), i.e. the voltage necessary to extend the depletion zone throughout the bulk material (see also Fig. 2.9). V is the externally applied bias, D the detector thickness, t_{Drift} the transit time of the charge carriers obtained from the TCT current pulses and x_0 the known starting point of the charge carrier movement. Equation (2.16) can be derived by solving

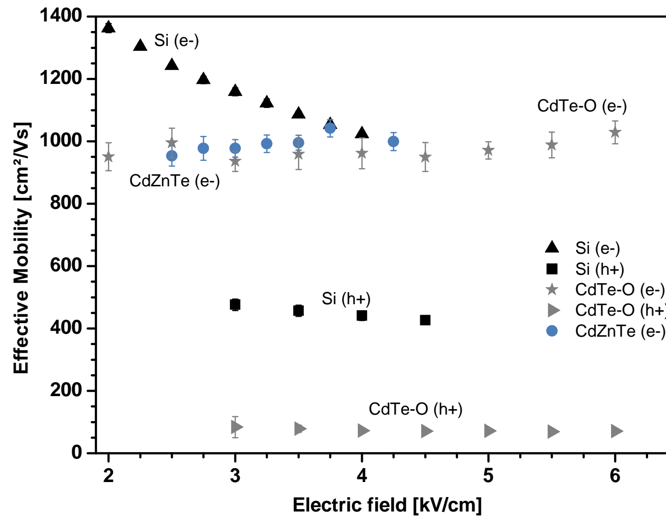

Fig. 2.13: Measured electron (e-) and hole (h+) mobilities as a function of the electric field for 1 mm thick Si, 0.5 mm thick CdTe and 2 mm thick CdZnTe crystals [2].

the following differential equation under the condition $x(0) = x_0$.

$$v_{Drift} = \frac{dx}{dt} = \mu_{Si} \cdot E_{Si}(x) = \mu \cdot \left[\frac{V + V_{FD}}{D} - \frac{2 \cdot V_{FD} \cdot x}{D^2}\right] \tag{2.17}$$

In case of CdTe and CdZnTe the mobilities are calculated neglecting any possible space charge inside the material, i.e. a constant electric field is assumed.

$$\mu_{CdTe/CdZnTe} = \frac{D^2}{t_{Drift} \cdot V} \tag{2.18}$$

The field dependent electron mobility, which is observed in the Si samples, is an effect of lattice scattering. In case of CdTe and CdZnTe this only occurs at field strengths beyond the experimental parameters (>12 kV/cm) [40].

Internal electric field

Apart from the direct impact on the charge carrier movement through the local fixation of charge carriers, trapping also influences the signal generation via the build-up of space charges. Without internal space charges the electric field inside a CdZnTe or CdTe detector should be constant and its magnitude should be given by the externally applied bias. However, measurements on 500 μm thick CdTe and 2 mm thick CdZnTe sensors yield electric field profiles similar to that of a Si p-n diode, where the field is governed by space charges (see Fig. 2.14).
Like the charge carrier mobilities, these electric field profiles were obtained from TCT measurements of the current signals induced by the absorption of α-particles in the sensor crystals. The prerequisite for this reconstruction of the electric field along the charge carrier trajectory is a time-dependent description of the charge carrier's position [41]. This relation can be established based on the integrated charge $Q(t)$ of the TCT current

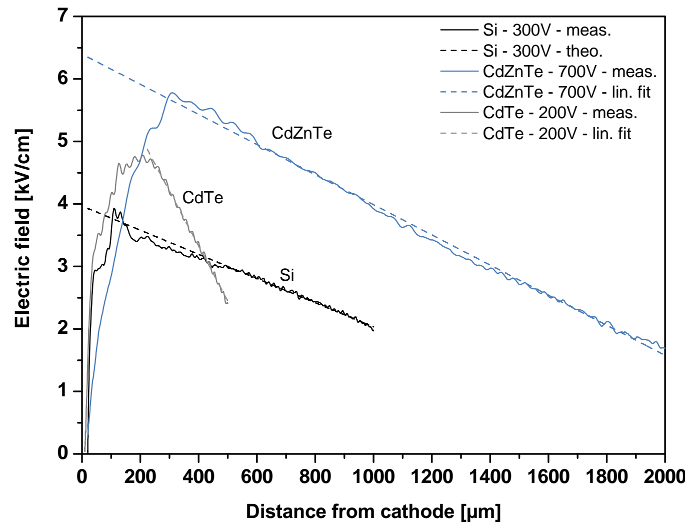

Fig. 2.14: Electric field distribution as a function of the distance from the cathode. The measurements were performed on 1 mm thick Si (400 V), 0.5 mm thick CdTe (200 V) and 2 mm thick CdZnTe (700 V) crystals using the transient current technique [2]. The dashed lines indicate linear fits to the experimental data of the CdTe and CdZnTe crystals. In case of the Si sensor, the dashed line is a result of a simulation of the internal electric field.

signals $i(t)$, where Q_0 is the total generated charge, which is known from the energy of the impinging α-particles.

$$Q(t') = \int_0^{t'} i(t)dt = \frac{Q_0}{D} \cdot (x(t') - x(0)) \quad (2.19)$$

$$\Rightarrow x(t') = \frac{Q(t') \cdot D}{Q_0} - x(0) \quad (2.20)$$

In combination with (2.11), these equations yield a position-dependent description of the electric field in a single channel detector.

$$E(x(t)) = \frac{i(x(t)) \cdot D}{Q_0 \cdot \mu} \quad (2.21)$$

The electric field in the Si p-n diode shows the expected linear decrease, which furthermore agrees nicely with a theoretical calculation of the field profile at room temperature and 96 V depletion voltage [39].
Based on this validation of the experimental method the electric field profiles in CdTe and CdZnTe were analyzed. As shown in Fig. 2.14, CdZnTe has a field profile, which can be, over a large section of the detector, approximated by a linear decrease in field strength from cathode to anode. This infers that these detectors contain a homogeneous, positive space charge, which is most likely caused by trapped holes.
A similar situation is found for the 500 μm thick CdTe sensors. However, here the limitations of the TCT method become obvious as the the electric field profile close to the cathode shows an artificial breakdown. This artifact is a result of a delay in the charge carrier movement right after their generation. The dense electron-hole cloud partially shields the sensor's electric field [2] thus influencing the charge carrier velocities and as a consequence also the reconstruction of the field profile. This measurement induced origin of the breakdown is supported by a recent study [42], in which electric field profiles obtained with the TCT method were compared to measurements based on the Pockel's effect. While the TCT measurements yield field breakdowns similar to the ones shown in Fig. 2.14, the transmission of polarized laser light through the crystals reveals no such effects.
In summary, the electric field in CdTe as well as CdZnTe deviates from the idealized model of a solid state ionization chamber with a constant electric field. To be precise, both materials show a significant internal space charge and an accompanying non-constant electric field.

Polarization

In general polarization describes the decrease of a sensor's detection efficiency due to the accumulation of space charges inside the detector volume. A detailed model of this effect can be found in [43] from which Fig. 2.15 was taken. The figure shows that the trapped hole charge as a function of the position inside the detector follows the intensity profile of the impinging X-ray beam. In that case the large space charge close to the cathode causes a sharp drop in the electric field and thereby introduces a zero field pinch point. This weak field region greatly hinders the charge carrier movement and leads to electron-hole recombination, i.e. an additional charge loss or a reduced charge collection efficiency. Previous measurements [2, 44] have shown that these polarization effects are prominent in CdTe sensors with Schottky contacts.
In addition to this, recent measurements have also shown lateral polarization in CdZnTe

sensors [45]. Lateral polarization is based on the inhomogeneous distribution of macroscopic defects in the sensor plane. These defects cause an inhomogeneous distribution of space charges above the electrodes of a pixel detector. The lateral component of the electric field resulting from these charges can steer charge carriers horizontally from one pixel to another, thus changing the effective size of the individual detector pixels.

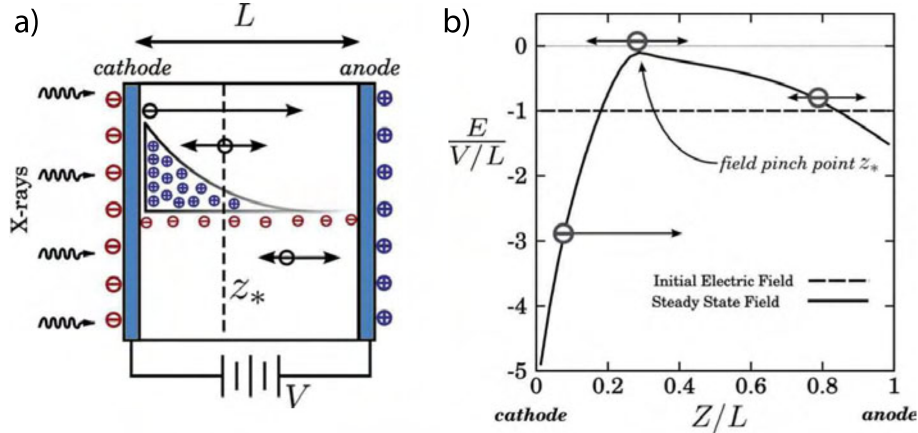

Fig. 2.15: Schematic view of the space charge distribution inside a CdZnTe sensor under X-ray irradiation (a) and the resulting electric field profile E(Z) including the field pinch-off point (b) [43]. V is the applied sensor bias and L gives the sensor's thickness.

2.6 Additional considerations for hybrid pixel detectors

Besides the already mentioned small pixel effect, charge loss, space charge build-up and polarization, the operation of a hybrid pixel detector is influenced by other sensor related effects.

Position resolution and spectral resolution

In position sensitive devices X-ray fluorescence can seriously decrease the detector performance because, depending on the sensor material, the fluorescence photons have absorption lengths on the order of 100 μm. As the photons are emitted isotropically, they can leave the pixel cell of the original photon interaction and lead to additional hits in the neighboring pixels, reducing the position resolution of the device. Furthermore, the spectral performance is negatively influenced, because the fluorescence photons carry energy away from the original pixel. A similar situation is found for elastic and inelastic photon scattering. Both effects again decrease the position and the energy resolution of a detector by distributing the initial photon energy over several pixels.
Fig. 2.16 illustrates this effect using the example of an idealized spectrum produced by a monoenergetic 90 keV X-ray source in one pixel of a CdZnTe detector. Apart from the full energy photo peak at 90 keV, the X-ray fluorescence lines at 23 keV, 27 keV, 63 keV and 67 keV are visible. The entries at 63 keV and 67 keV come from a partial energy deposition, i.e. when the fluorescence photons escape from the pixel. The low energy lines at 23 keV and 27 keV are the result of fluorescence photons entering the pixel from its neighbors. Fig. 2.16 also contains the Compton edge and the Compton background. In general the angle-dependent energy transfer between electron and photon leads to a continuous energy distribution ranging from zero up to the maximum transfer at a scattering angle of 180°. For 90 keV photons the maximum energy transfer to the electron is

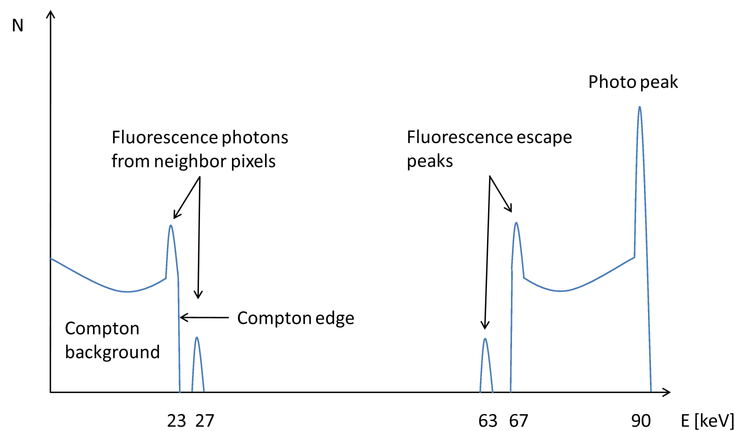

Fig. 2.16: Simplified spectrum of a monoenergetic 90 keV X-ray source including photo effect, Compton effect and X-ray fluorescence as measured with a single pixel of a pixel detector. The spectrum contains events where the photon escapes the pixel as well as events in which a photon is scattered into the observed pixel.

approximately 23 keV. Therefore the continuous Compton background below the 23 keV Compton edge results from scattered photons leaving the pixel and similarly the continuous section between 67 keV and 90keV is caused by photons being scattered into the pixel under investigation.

Beam hardening and dual energy imaging

Apart from their impact on the spatial as well as the spectral performance, the previously mentioned photon-matter interactions have further consequences for X-ray imaging. As can be seen from Fig. 2.1, the total cross section for X-ray absorption drops sharply with increasing X-ray energy. A direct result of this is the so-called *beam hardening*, which describes the gradual increase of the average photon energy in an X-ray spectrum as the photons travel through an absorber. This means that due to the high absorption coefficient, low energy photons have a higher absorption probability, leaving only higher energetic photons in the spectrum. Fig. 2.17 demonstrates this effect on a typical tube X-ray spectrum. It is evident that although both metal absorbers reduce the overall number of photons, they predominantly suppress the low energy section of the spectrum. A further consequence of beam hardening is that the total absorption coefficient of the object gets depth dependent. To illustrate this, one can consider a small object with constant density placed first on the surface of a thick absorber and secondly inside the same absorber. It is evident that the test object inside the absorber will not reduce the beam intensity as much as it does on the surface of the absorber due to the higher average energy of the X-ray spectrum inside the thick absorber. In CT scans, this beam hardening leads to unwanted image artifacts.
One method to compensate for beam hardening is the *dual energy* imaging approach proposed by Alvarez and Macovsky [46]. This method is based on the fact that X-ray matter interactions happen through two different processes whose cross sections are influenced by different absorber properties. Specifically, the photoelectric effect is mainly sensitive to the electron density, i.e. the atomic number of the absorber while the Compton cross section is influenced by the mass density.
Hence, if a detector system can provide two spectrally distinct measurements of the same object, a reconstruction of the individual absorption coefficients μ_P and μ_C and as a con-

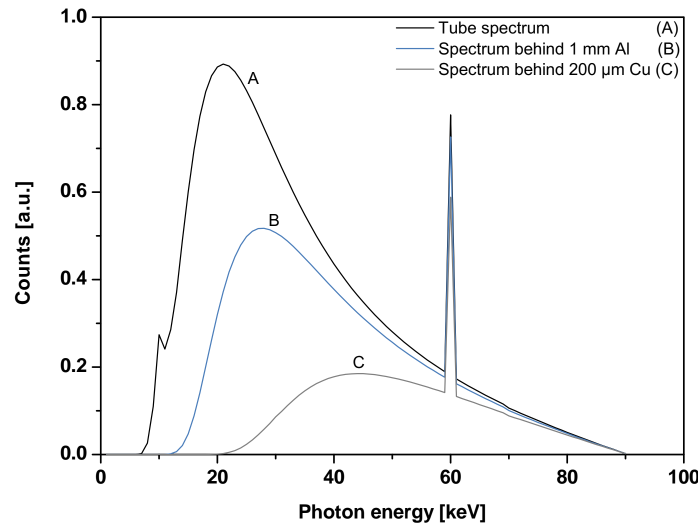

Fig. 2.17: Simulation of the beam hardening effect caused by two different metal absorbers. Due to the predominant absorption of low energy photons in the absorbers, the average energy of the transmitted spectrum is increased compared to the original tube spectrum. At 200 μm the higher absorption coefficient of Cu introduces a stronger beam hardening than that of the 1 mm Al absorber.

sequence tissue identification becomes possible. In this context "spectrally distinct" refers to two images of the same object along the same X-ray path, which are however based on different parts of the X-ray spectrum.
Several approaches for Photo-Compton reconstruction are currently under investigation. Among these are the irradiation of the object with two different X-ray spectra (tube energy switching) [47] and the imaging with a sandwiched detector where the first layer primarily detects low energy X-rays and the second layer the higher energetic ones (dual detector systems) [48]. Multi-threshold or simultaneously counting and integrating systems (see chapter 3), which perform two different measurements with one sensor in one image frame, are also suited for this task.
Recently an additional contrast agent identification has been proposed [49]. In this case a third spectrally distinct measurement is used to detect the characteristic K-edge of an applied marker, increasing the image contrast in perfused body regions, e.g. tumor centers. Here, multi-threshold systems could be of great advantage. In contrast to a tube energy switching approach, they acquire all three images in only one irradiation period. Thus, they potentially offer a reduced patient dose. When compared to a sandwiched detector, the multi-threshold systems could also profit from a reduced unit price because they require only one detector layer instead of several. Nevertheless, when choosing between a multi-threshold or a multi-layer approach, the complexity of the ASIC and the power consumption have to be considered as well.

3. CIX 0.2 detector

3.1 Concept

The simultaneously counting and integrating X-ray detector CIX was designed as a merger of two distinct signal processing concepts that are commonly used in X-ray imaging. The first concept is the photon counting or pulse mode approach. In this case detectors register individual photons by means of one or several thresholds. Depending on the number of thresholds per pixel, these devices permit tissue identification or contrast agent imaging without a variation of the X-ray beam energy. Regardless of this advantage, current ASIC[1] generations only allow single pulse counting up to rates of approximately 50 Mcps/mm^2 [4] because of pulse pile-up. Therefore current counting systems are not suited for high flux applications like computed tomography where the photon rates can exceed 1 Gcps/mm^2. In high flux conditions integrating systems are used. These detectors register the total amount of charge that is deposited inside the sensor instead of identifying individual photons. Hence, integrators can cope with very large photon fluxes but are on the other hand limited by electronic noise at low fluxes.
The CIX concept combines the individual advantages of the counting and integrating concepts in every single pixel cell. By using the photon counter in the low flux regime and by relying on the integrator data under high flux conditions, CIX offers an increased dynamic range compared to counting only or integrating only systems. The second advantage of a simultaneously counting and integrating detector is the ability to reconstruct the average energy $\overline{E}$ of the registered photons. This value is obtained by dividing the signal current I, measured with the integrator, by the number of photons N registered in the counter:

$$\overline{E} = \frac{I \cdot E_{e/h}}{N \cdot t_{Frame}^{-1} \cdot e} \tag{3.1}$$

In this equation $E_{e/h}$ denotes the electron-hole pair generation energy of the sensor material, t_{Frame} the measurement duration and e represents the elementary charge. Medical imaging could profit from this information in terms of an improved image quality as the average photon energy gives a direct measure of the beam hardening, which, if uncorrected, leads to unwanted image artifacts. Apart from the large dynamic range and the measurement of the average photon energy, the CIX detector can also be used for dual energy imaging, i.e. the reconstruction of the photoelectric and the Compton components of the total absorption coefficient (see section 2.6). As has been demonstrated in [50], the noise correlations between the counter and the integrator measurements reduce the image noise compared to dual energy imaging devices that lack this correlation, e.g. tube energy switching or dual layer systems.

3.2 CIX 0.2 ASIC specifications

At the moment of writing, the CIX chip is available in its second major revision. The design of CIX 0.2 introduced a number of changes compared to the predecessor generation

[1]"Application specific integrated circuit"

CIX 0.1. For more details on these changes as well as information on several other ASICs related to the design of CIX 0.2 see [1]. The most important feature with respect to this work is the addition of a sensor connection in every pixel cell. Hence, CIX 0.2 is the first simultaneously counting and integrating X-ray imager.
The following list gives an overview of the key specifications of CIX 0.2.

- Chip dimensions 5.7 x 4.1 mm^2
- Fabricated in AMS 0.35 μm technology
- 8 x 8 pixel matrix
- 500 x 250 μm^2 pixel area
- 138 wire bond pads (80 mandatory to connect, 58 optional)
- 64 bump bond pads for sensor connections
- 16 bump bond pads for guard ring connections
- 3.2 mW typical per pixel power consumption
- Three 16-bit counters per pixel
- Two 16-bit integrator latches per pixel
- Four 16-bit readout latches per pixel
- I^2C bus[2] interface for ASIC slow control
- Low swing differential current steering logic (DCL - see appendix A)
- Dead time free readout with double buffered readout (see appendix B)

Fig. 3.1 shows two photographs of a bare CIX 0.2 chip highlighting some of the ASIC's building blocks. As shown, the chip features wire bond pads along three edges. Out of these 138 connections only 80 pads in the lowermost two rows (g) are absolutely necessary for the operation of the chip. This geometry allows either a three side butting of several chips or leaves some room for sensors that partially exceed the ASIC dimensions. The control interface of CIX 0.2, which steers the chip register and 28 internal DACs[3] and bias cells, is implemented via an I^2C interface situated at the top edge of the chip (b). Another feature marked in Fig. 3.1 is the address sequencer (c), which is used in the chip readout. It grants all eight pixels of one row parallel access to the bus receiver elements (e) by means of the row select logic (d). The bus receiver elements can forward their contents to the chip's periphery via differential outputs that are controlled by LVDS[4] drivers.
The highlighted area in the center of Fig. 3.1 outlines a single CIX 0.2 pixel cell. A close-up of this layout is displayed in Fig. 3.2. The preamplifier and feedback circuits (a) of the pixel are located at a maximum distance away from the digital elements (e). This layout was chosen in order to minimize cross-talk in the sensitive analog part (a) of the pixel cell. By arranging the pixels in flipped pairs along the columns of the chip, this maximum separation is maintained in all pixels. A side effect of this geometry is the off-center placement of the bump bond pad (g), yielding a minimum distance of 150 μm between

[2]Inter-integrated circuit
[3]Digital to analog converter
[4]Low voltage differential signaling

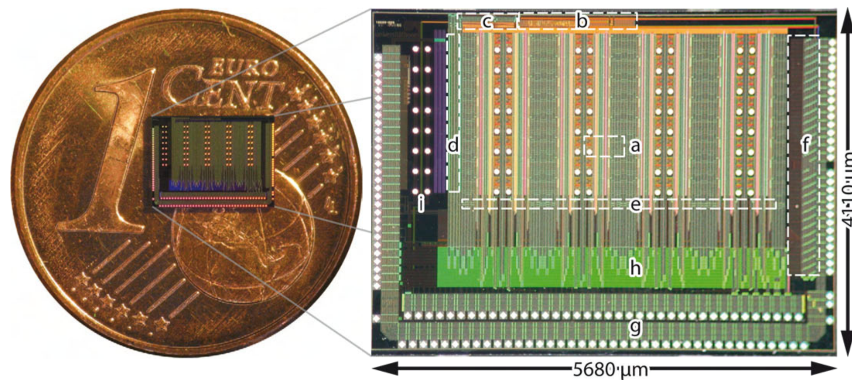

Fig. 3.1: Photographs of the CIX 0.2 ASIC. The enlarged view on the right shows some vital components: (a) single CIX pixel cell, (b) chip register and I^2C interface, (c) address sequencer, (d) row select elements, (e) bus receivers and LVDS output drivers, (f) bias cells and DACs, (g) wire bond pads necessary for the chip operation, (h) power and signal routing matrix, (i) guard ring bond pad connections [1].

two pads of a pixel pair. Furthermore, note that a significant part of the pixel area has to be dedicated to the storage of the measurement data. This can be seen by the relatively large size of the counter, latch and bus driver block (e), which amounts to roughly 40 % of the pixel area. It owes its size to the fact that each pixel contains three counters and six latches. The pixels also contain several alternative implementations of core elements such as the charge injection circuits and parts of the feedback and the integrator. These were introduced in order to evaluate different implementations for a simultaneously counting and integrating chip. All this then results in an overall pixel area of 500 x 250 μm^2.

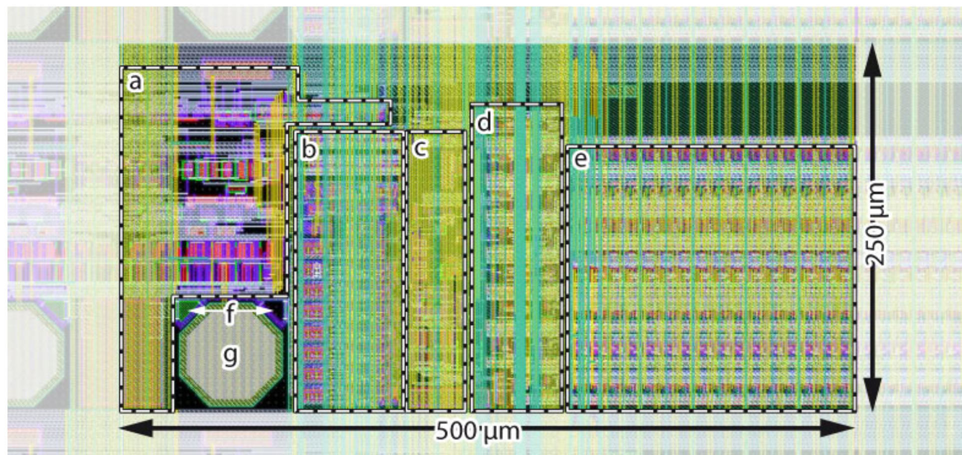

Fig. 3.2: Layout of a pixel cell. (a) preamplifier, feedback and charge injection circuits, (b) pixel register and tune DAC, (c) integrator and charge pumps, (d) pump logic and control logic, (e) counters, latches, multiplexers and bus drivers, (f) photo diodes, (g) sensor bump bond pad [1].

3.3 CIX 0.2 pixel cell concept

This section gives a condensed introduction into the key components of the CIX 0.2 ASIC. Additional information can be found in [1] from which most of the figures in this section were taken.
A general overview of the basic building blocks of a CIX 0.2 pixel cell can be seen in Fig. 3.3. In detail, these blocks are the photon counter, the integrator, the feedback circuit and various signal sources that are used for the characterization of the chip. Independent of which signal source is chosen, the current pulses enter the photon counter first. From there they are replicated by a complex feedback mechanism and subsequently fed to the integrator.

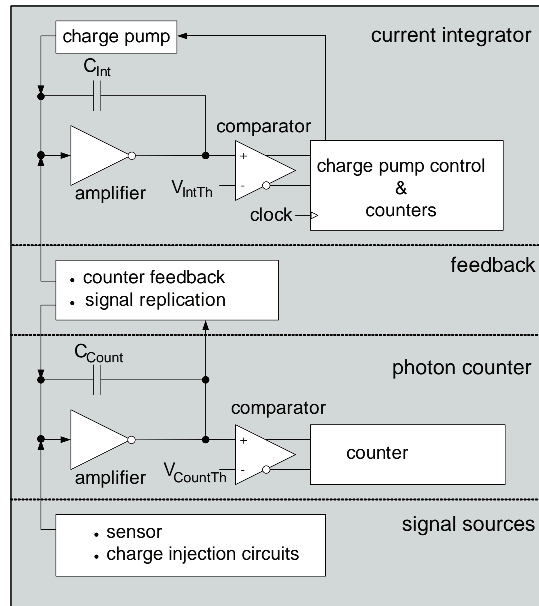

Fig. 3.3: Basic building blocks of a CIX 0.2 pixel cell.

3.3.1 Photon counter

Fig. 3.4 displays a schematic view of the photon counter. The initial stage of this circuit is a so-called *charge sensitive amplifier* (CSA), consisting of a preamplifier with a feedback capacitor C_{Fb}. As shown in the inlay in Fig. 3.4 the CSA's output voltage rises in proportion to the charge that is accumulated on C_{Fb}. A constant current feedback I_{Fb} removes the charge from the capacitor and thereby causes an approximatively linear return to baseline in the preamplifier. The CSA is followed by a comparator or discriminator stage, i.e. a circuit which compares the input voltage (here labeled OUT) to a reference potential $V_{CountTh}$. If OUT is larger than $V_{CountTh}$, the comparator switches to a logical high state. In CIX 0.2 the comparator is implemented as a two-stage element. The first stage handles the actual threshold comparison and the second stage increases the switching speed of the discriminator. As $V_{CountTh}$ controls the threshold above which a signal is registered by the counter, a fine granularity of the threshold levels is required. Therefore the $V_{CountTh}$ potential is generated off chip by an external 14-bit DAC with a step width of 0.3 mV. Furthermore, it is necessary to balance process variations in the preamplifiers and the discriminators of the individual pixels. In order to achieve this, every pixel is

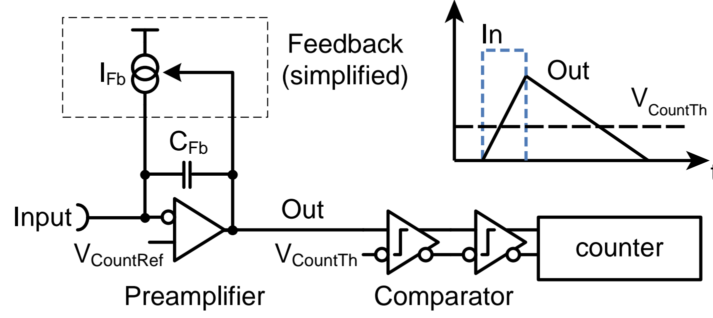

Fig. 3.4: Schematic view of the CIX 0.2 photon counter consisting of a charge-sensitive amplifier (preamplifier with the feedback capacitor C_{Fb}), a two-stage comparator, a counter and a simplified illustration of the feedback circuit. The design value of C_{Fb} is 10 fF. The inlay on the right shows an idealized system response (OUT) to a constant current signal (IN).

equipped with a 6-bit TuneDAC, which allows to slightly modify the $V_{CountTh}$ potential and thus balance the dispersion between the pixels. A global 6-bit TrimDAC controls the size of the stepping of the TuneDACs. The final component of the photon counter is a fast 16-bit counter.

The design of the counter follows that of a *paralyzable counter* [51]. This means that once a signal has passed the discriminator threshold, the counter is unable to process any further inputs until the preamplifier output drops again below the $V_{CountTh}$ threshold. Fig. 3.5 illustrates the *pile-up* behavior of such a paralyzable counter. If one or several input events occur before the preamplifier has returned to the baseline, the individual pulses are stacked on top of each other, prolonging the *time over threshold* (ToT). The paralyzability of the system lies in the fact, that at too high input rates the preamplifier output never falls below the discriminator threshold and the whole counting mechanism breaks down. Fig. 3.5 also shows the response of a nonparalyzable system. In this case a pulse, which falls into the dead time of a previous event, is simply ignored and the dead time is not extended. This causes a reduction in the observed count rate but not a total breakdown of the counting system.

The count rate N_{Meas} of a paralyzable counter, if exposed to monoenergetic, poisson-

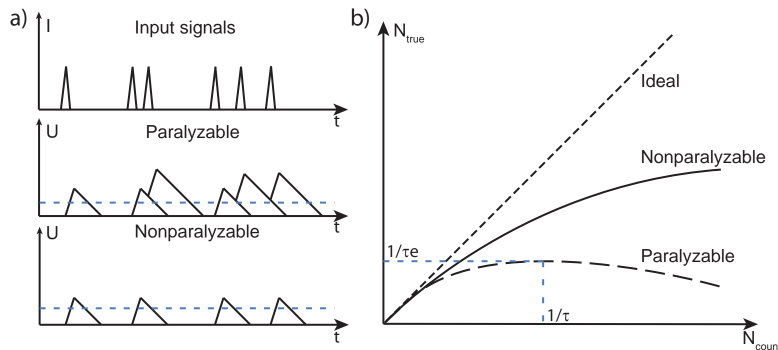

Fig. 3.5: (a): Response of a paralyzable and a nonparalyzable photon counter to a series of monoenergetic input pulses. The discriminator threshold is indicated by the dashed line. (b): Measured rate N_{Meas} as a function of the true incoming rate N_{True} for an ideal counter, a nonparalyzable and a paralyzable one. τ indicates the dead time of the system [51].

distributed pulses of rate N_{True}, is given by [51]:

$$N_{Meas} = N_{True} \cdot e^{-N_{True} \cdot \tau_{Dead}} \quad (3.2)$$

In reality the so called *dead time* τ_{Dead} is even a bit longer than the ToT as the discriminator needs some time after a signal has fallen below the threshold before it can register a new threshold crossing. One way to counter the pile-up effect is to increase the feedback current, i.e. to discharge C_{Fb} quicker and have a faster return to baseline. Although this allows higher count rates, it also introduces the problem of *ballistic deficit*. Ballistic deficit refers to the discharge of the feedback capacitor while the preamplifier is still integrating the incoming current pulse. Due to the continuous nature of the feedback in CIX 0.2 this happens all the time and for a large I_{Fb} this charge loss can become significant, resulting in a decreased pulse height of the output signal. Typical values for the ballistic deficit of CIX 0.2 range between 10 % at 10 nA feedback current up to 29 % at 91 nA [1].

3.3.2 Integrator

The CIX 0.2 integrator is implemented as a current to frequency converter. Fig. 3.6 illustrates that similar to the counter, the incoming charge is again stored on a capacitor (C_{Int}) of a charge sensitive amplifier. Yet, in contrast to the continuous feedback of the counter, the integrator is equipped with a clocked feedback. This circuit subtracts a configurable amount of charge Q_{Pump} from C_{Int} on the next positive edge of the $CKInt$ clock once the amplifier output passes the predefined V_{IntTh} threshold. The input current is measured by counting the number of charge pump events N_{Pump} and recording the time t between the first and the last pump event.

$$I = \frac{N_{Pump} \cdot Q_{Pump}}{t} \quad (3.3)$$

Fig. 3.7 shows the general principle of the current measurement using the example of a 100 *µs frame duration*. The term "frame" refers to the time during which the integrator counters are activated, i.e. in which the number of charge pump events are recorded. For illustrative purposes two assumptions are made in the upper plot. The first one is that the output voltage of the integrator at the beginning of the frame interval is close to the pump threshold. Note that this assumption can be made as the pump mechanism is not synchronized to the measurement frame. Moreover, the charge pumps are also operated outside a frame because otherwise a small input current would be sufficient to drive the integrator into saturation. Hence, this initial assumption represents just one particular

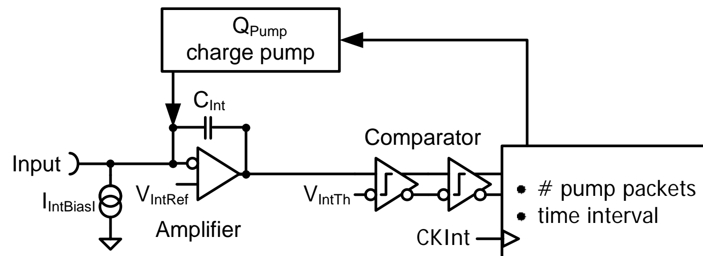

Fig. 3.6: Schematic view of the CIX 0.2 integrator. C_{Int} has a size of 50 fF. The clocked feedback subtracts a charge packet of size Q_{Pump} from the feedback capacitor C_{Int} once the V_{IntTh} threshold is passed. A counting logic registers the number of pump events and the time interval in which they took place.

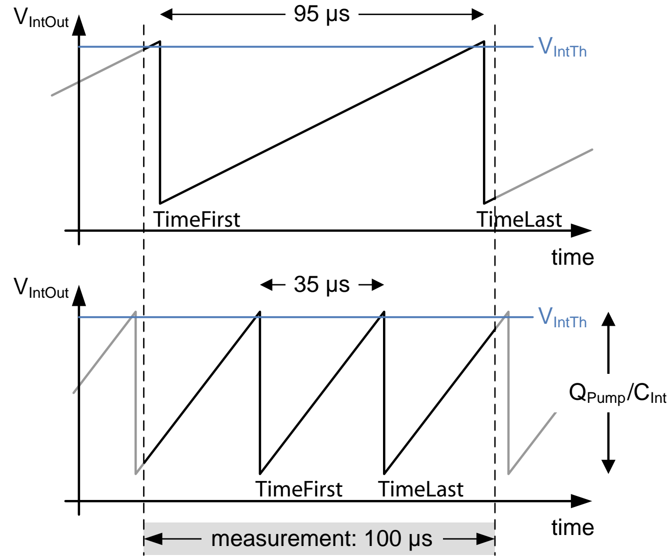

Fig. 3.7: Illustration of the integrator current measurement. The potential change at the integrator output caused by the charge pump is given by Q_{Pump}/C_{Int}. In both plots a frame time of 100 μs is assumed, however both currents produce only two pump events in the measurement frame. The correct measurement of the currents is obtained from the different TimeFirst and TimeLast time stamps of the pump events.

phase relation between the charge accumulated on the integrator's capacitor and the start of a measurement frame. The second assumption is that the input current in the upper plot happens to be so small that only two charge pump events fall into the 100 μs frame. With these assumptions the current measurement can be described as follows. Once the frame is started, a 16-bit time counter begins to record the $CKInt$ pulses. At the first charge pump event the respective time counter value is stored into the TimeFirst latch. A second latch, the TimeLast latch, updates its time stamp every time a subsequent pump event is triggered and thus keeps track of the clock cycle at which the last pump event occurred. The difference between these two time markers then allows the measurement of the time in which the charge pump events took place. Compared to a simpler current measurement concept based on a constant frame duration, this rather complex concept offers the advantage of a much higher measurement precision. To illustrate this point Fig. 3.7 shows a second graph with a three times larger current than the one in the plot above. Here, it is assumed that the last pump even happened shortly before the beginning of the frame and that again only two pump events fall into the measurement interval. Regardless of the identical number of pump events, the system now registers a larger current as the separation between the pump events is smaller in the second sample. Counting only the number of pump events and dividing these by the frame time would have yielded an identical current in both examples.
The use of the two time stamps necessitates that at least two pump events happen during a measurement frame. This sets a lower limit to the minimum input current of:

$$I_{Min} = \frac{2 \cdot Q_{Pump}}{t_{Frame}} \tag{3.4}$$

Equally the largest current is registered if the charge pump is triggered every $CKInt$ clock cycle, i.e. the pump is working at its maximum rate N_{max}:

$$\begin{aligned} I_{Max} &= Q_{Pump} \cdot N_{Max} \cdot t_{Frame} \\ &= Q_{Pump} \cdot t_{Frame} \cdot f_{CKInt} \cdot t_{Frame} \end{aligned} \tag{3.5}$$

In general the precision of one such integrator measurement is given by:

$$\frac{1}{t_{Frame} \cdot f_{CKInt}} \tag{3.6}$$

This means that a change in the time difference between TimeFirst and TimeLast by only one clock cycle already translates into a different current result. So in theory, neglecting the electronic noise and assuming the integrator is set to a clock rate of 10 MHz and a 1 ms frame duration, a change in the input current of only 1/1000 can be detected. A further consequence of this is that the system has an approximately constant measurement precision over its dynamic range. Approximately refers to the fact that the precision is slightly reduced at the lowest input currents (close to I_{Min}) as in that case the charge on C_{Int} at the beginning of a frame introduces some measurement uncertainty. For a more detailed treatment of the system's measurement precision refer to [1]. The basically constant measurement precision has to be compared to a current measurement based on an ADC[5]. Such devices usually determine the input signal by step-wise approximating the input with a reference signal. The minimum step-width of the ADC then determines the minimum input current as well as the precision. This results in a relative measurement precision, which depends on the size of the input signal.
In the case that CIX 0.2 has to measure currents smaller than I_{Min}, the chip is equipped with an internal *IntBiasI* bias current source. By using this *IntBiasI* current, it is possible to effectively shift the dynamic range of the integrator to lower input currents. At the same time, the upper limit of the dynamic range is also slightly lowered because the sum of signal and bias current still has to stay below the I_{Max} condition.
So, by selecting a particular f_{CKInt} integrator clock frequency, t_{Frame} frame duration and Q_{Pump} charge pump size, the integrator's precision and its dynamic range with the I_{Min} and I_{Max} limits can be tuned according to the application.

Integrator charge pumps

Fig. 3.8 shows a schematic of one of the three charge pump types available on the ASIC. This capacitive charge pump works by switching the potentials across the capacitor C_{Pump}

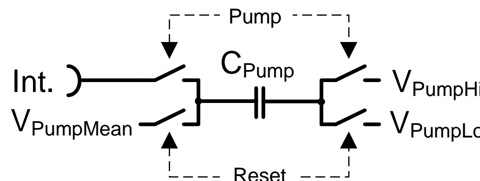

Fig. 3.8: Schematic of the CIX 0.2 capacitive charge pump. During the reset/recharging of the pump the switches at the nodes $V_{PumpMean}$ and $V_{PumpLow}$ are closed while the other two remain open. When the state of the switches is inverted a charge packet of $C_{Pump} \cdot (V_{PumpHi} - V_{PumpLo})$ is injected. C_{Pump} has a size of 25 fF.

[5]"Analog to digital converter"

and thus injects a configurable amount of charge into the *Int* node. The size of the charge packet is determined by the potential difference between V_{PumpHi} and V_{PumpLo}. The $V_{PumpMean}$ connection guarantees that the action of the switches themselves does not inject additional charges. Apart from the capacitive charge pump, the system also features a switched constant current source. This circuit discharges C_{Int} by enabling the I_{Pump} current source for half a $CKInt$ clock cycle. The size of the individual Q_{Pump} packets is controlled by the current source's DAC setting. More details on the charge pumps can be found in [1].

3.3.3 Feedback

The feedback circuit of CIX 0.2 is the heart of the simultaneously counting and integrating concept. Its task is to discharge the counter preamplifier and at the same time to reproduce the input current for the integrator. These at first glimpse conflicting requirements are met by using a number of differential pairs as illustrated in Fig. 3.9. Due to the high significance of the feedback for the simultaneous counting and integrating concept, the following paragraph will give a detailed description of the operation of the feedback circuit.
Assume that the sensor produces an electron signal, i.e. it draws current from the preamplifier input node. This current signal is integrated on the feedback capacitor C_{Fb} and produces an increase of the voltage of the inverting preamplifier. Since the preamplifier output is connected to the left p-MOS of the first differential pair, this transistor will close and hence allow less current from I_{Fb} to flow into the left branch of the pair. However, as the current sources situated at the bottom of the two branches both drain 50 % of the I_{Fb} current, the imbalance in the p-MOS switches will also cause the current source in the left branch to draw current from node 1. Similarly, the right branch will be supplied with too large a current and hence it will deliver a net current to the input node of the preamplifier. This current cancels the electron signal of the sensor and thus steers the preamplifier into a dynamic equilibrium. In other words, a constant current like a leakage current, which flows into the input of the preamplifier, causes a constant offset at the preamplifier output *Out*. This deviation from the $V_{CountRef}$ reference potential shifts current from one branch of the first differential pair to the other such that the original constant current is canceled and the integrated charge on C_{Fb} reaches a constant value. At the same time this imbalance also causes a net current flow into or out of node 1 thereby achieving the replication of the input current. It is worth mentioning, that the baseline shift, i.e. the offset at the preamplifier output, that has to be maintained in order to cancel a constant current

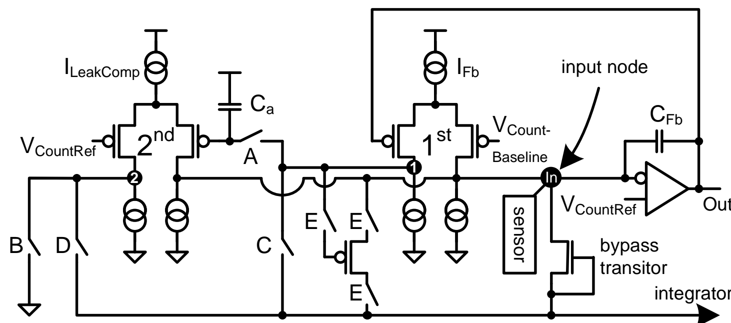

Fig. 3.9: Schematic view of the CIX 0.2 feedback. The sensor connection to the preamplifier is indicated by the arrow on the right side. A complex switching network allows different leakage current compensation mechanism to be applied.

flowing into the input node, influences the operation of the discriminator. To be more specific, the preamplifier output potential is compared to the constant $V_{CountTh}$ threshold voltage. Hence, if the baseline of the preamplifier is shifted permanently by an offset, the relative position of the discriminator threshold and thereby the counting statistics is altered.
In general, a constant current coming from a direct converting sensor is caused by the leakage current flowing through the material at high bias. This current is not related to the X-ray signals and should therefore be subtracted from the integrator measurement. For this CIX 0.2 is equipped with several leakage compensation circuits. The static and continuous leakage current compensation mechanisms will be described below.

3.3.4 Static leakage current compensation

As the name *static leakage current compensation* indicates, this feedback mode is geared towards the subtraction of a constant leakage current component. It requires the use of the second differential pair shown in Fig. 3.9. The first phase of the static leakage current compensation is the *sampling phase*. In this mode (see Fig. 3.10) the integrator is disconnected from the feedback through opening switches C and D in Fig. 3.9. Simultaneously, the potential at node 1 is stored on the capacitor C_a. As node 1 is now connected to the second differential pair, the potential at node 1 can control the right branch of this pair. So, similar to the operation of the preamplifier feedback (first pair), this imbalance at the second pair causes a net current flow into or out of the input node of the preamplifier, thereby canceling the leakage current. The major difference between the two differential pairs is that the second one is able to deliver roughly twice the current of the first one and that it also reacts more slowly due to the large time constant introduced by C_a. Once the sampling is complete and the leakage current is compensated by the second differential pair, switch A is opened and switch C is closed such that current can flow into the integrator (see Fig. 3.11). This second phase of the static leakage compensation is referred to as the *frame phase* because the system is able to measure the current with the integrator. Fig. 3.12 illustrates the static leakage current compensation using the example of a constant leakage current on which a photon absorption event is superimposed. In the sampling phase the second differential pair is set to cancel the leakage current, i.e. the current delivered by the feedback pair drops to zero. Following this, if a signal current enters the system during the frame phase (see static LC phase in Fig. 3.12), the finite slew rate of the first pair allows it to mirror this current signal. The second differential pair is disconnected from node 1 and hence still delivers its constant compensation current.
The first differential pair is able to provide a current of approximately 45 nA and the

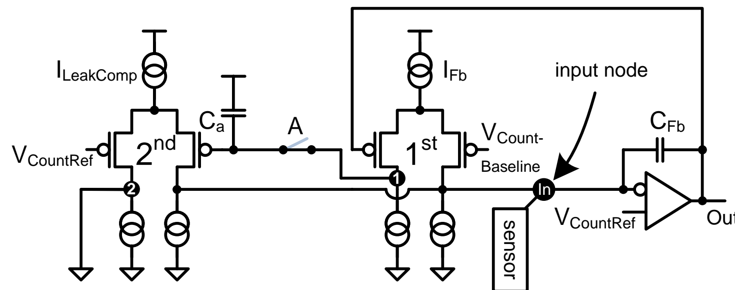

Fig. 3.10: Feedback configuration in the sampling phase of the static leakage compensation mode. Switch A connects node 1 to the input of the second differential pair and charges the sampling capacitor C_a.

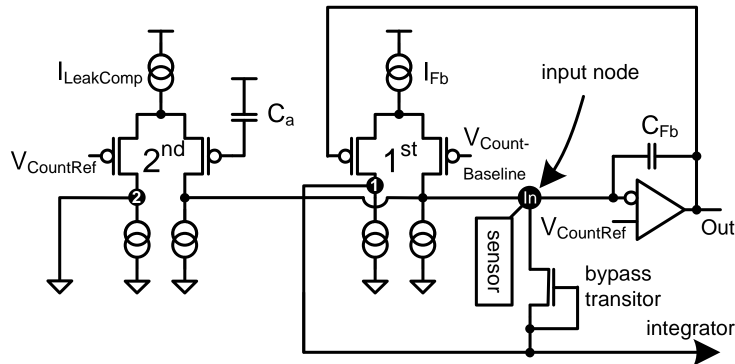

Fig. 3.11: Feedback configuration under measurement (frame) conditions of the static leakage current compensation. The second differential pair delivers a constant current, according to the potential stored on C_a into the preamplifier input node. Like this it can cancel a constant leakage current. The integrator is connected to node 1 of the first differential pair.

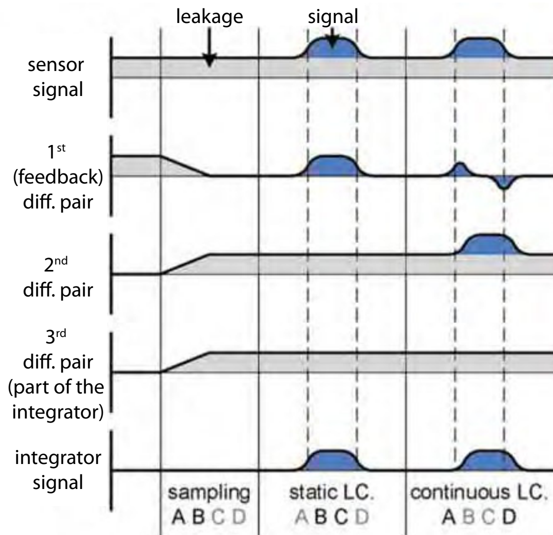

Fig. 3.12: Diagram of the currents delivered by the sensor, the differential pairs and the integrator in CIX 0.2 under static and dynamic leakage current compensation. The state of the switches in Fig. 3.9 is given at the bottom of the figure, with black letters indicating closed switches and gray letters showing the open ones.

second pair can deliver up to 91 nA. In case the input signal is larger than these currents the input node is equipped with a bypass transistor (see Fig. 3.9), which opens when the sensor currents exceed these limits. This allows even very large signal currents to reach the integrator.

3.3.5 Dynamic leakage current compensation

The *dynamic leakage current compensation* mechanism has been designed in order to achieve higher count rates than the static leakage current compensation. Its key concept is to lower the preamplifier baseline according to the effective DC-component of an incoming pulse train. This increases the relative discriminator threshold and should in principle allow higher count rates.

Dynamic leakage current compensation requires the switches A and D in Fig. 3.9 to be

closed and switches B, C and E to be open. In this way the first differential pair is only connected to capacitive loads and hence can only carry AC signals (see. Fig. 3.12). It therefore controls the current flowing out of the second pair by opening or closing the p-MOS transistor in the right branch of the second differential pair. Hence, the second differential pair is responsible for the compensation of leakage and signal current. However, since C_a is very large, this effectively induces a low pass filtering of the input signals. As a result, the baseline at the preamplifier output is shifted at high rates because these signals carry a higher effective DC component. A third differential pair, located in the integrator and not shown in Fig. 3.9, takes care of the unwanted leakage current component. The low pass filtering of the input currents is not considered to be an issue for the integrator as the integration times are larger than the time constant of the filtering.

3.3.6 Issues with the leakage current compensation

During the test phase of CIX 0.2 several issues were identified that finally led to a selection of the optimal leakage current compensation mode. Based on the promised feature, the dynamic leakage current compensation would be the first choice as a compensation mode. Nevertheless, a more detailed inspection reveals that the compromise of a higher rate capability through a rate-dependent baseline shift is not necessarily advantageous. In a detector which aims at determining the average photon energy the number of photons should be recorded as precisely as possible. Pulse pile-up already imposes a limit to the counting performance but if the count rate further has to be corrected for a per pixel baseline shift and the subsequent change in the counting statistics, the initial benefit of a high rate capability is lost. This and the fact that the noise of the dynamic leakage current compensation is approximately twice as large as that of the static leakage current compensation [1] mark the dynamic compensation method as the less favorable one.

Feedback detuning

The static leakage current compensation is also not performing flawlessly. Due to a small design error (see Fig. 3.13) switch A, which is tasked with the connection of the sampling capacitor C_a to the first feedback pair, is not as tight as desired. Instead of retaining its charge for several minutes, the capacitor loses its charge in a few seconds (see Fig. 3.14). This has the effect that the second feedback pair is detuned and then delivers an additional time-dependent current component instead of canceling the leakage current. The

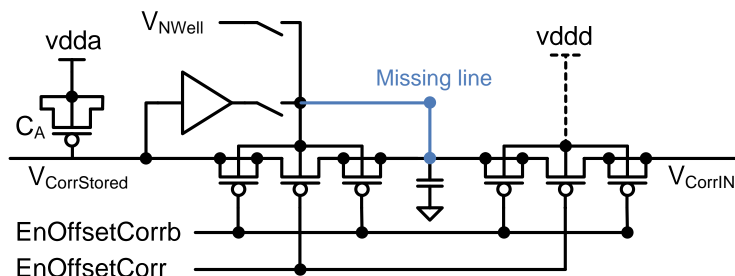

Fig. 3.13: Implementation of the sampling switch A including the missing connection (blue). Due to this design flaw the switch allows a significant current to flow even in its closed state and thus prevents the use of the static leakage compensation in X-ray measurement conditions.

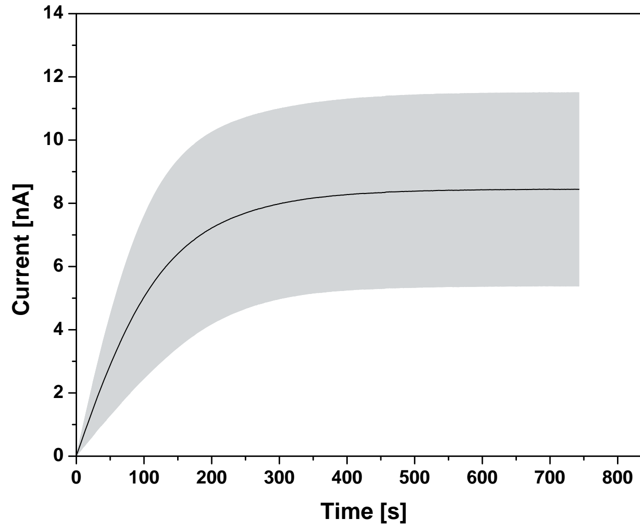

Fig. 3.14: Detuning of the compensation current in static leakage current compensation as measured with the CIX 0.2 integrator. The black line indicates the average and the gray ribbon shows the standard deviation for the 64 pixels. The discharge of C_A closes the p-MOS transistor in the right branch of the second differential pair. As a consequence the second pair draws current from the input node, which is equivalent to an electron signal coming from the sensor. The inverting output of the integrator then yields a positive current.

error basically prevents the use of the static leakage current compensation in combination with an X-ray tube as the sampling has to take place when the X-ray tube is switched off. However, even if the tube is switched on immediately after the sampling phase, the powering up process of the tube (a few seconds) is long enough for the discharge of C_a to have a significant impact on the measurement. The feedback deviates for example by approximately 300 pA from the original current after only 5 s of operation. Previous measurements based on on-chip injection circuits [1] were not influenced as strongly as the measurements presented in this work due to the ns or μs time scales on which the injection circuits can be activated and deactivated.

Feedback mismatch currents

A second type of offset current is introduced by the differential pairs. Process variations on the chip can cause imbalances in the current drains at the bottom of the differential pairs in Fig. 3.9, i.e. the two branches do not draw exactly the same current. In this case the imbalance is forwarded to the preamplifier input node in the form of a constant mismatch current. Fig. 3.15 shows an example of these mismatch currents in the first differential pair as a function of the applied feedback current. It is found that the feedback produces on average a negative current of approximately 2 nA at maximum feedback settings. Since the integrator can in principle only measure positive currents, this means that any input current of the integrator has to be larger than 2 nA. Therefore, in order to measure small input currents an additional positive bias current has to be applied. Apart from the negative average input current, Fig. 3.15 illustrates that the spread between individual pixels is very large (roughly 5 nA). Hence, the globally applied *IntBiasI* current has to be much larger than 2 nA in order to cancel the negative mismatch currents in all pixels. Unfortunately this limits the dynamic range of the detector in some pixels as pixels with a positive mismatch current will be supplied with an offset current of several nA.

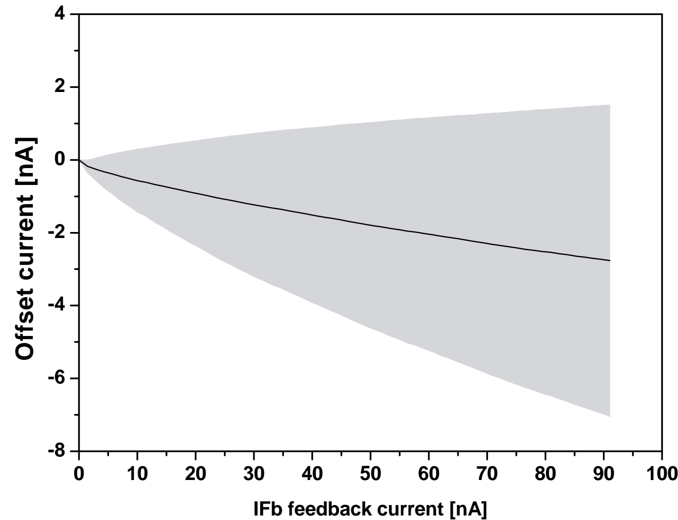

Fig. 3.15: Average mismatch currents of the first differential feedback pair as a function of the feedback current measured with the CIX 0.2 integrator. The black line indicates the module-wide average and the gray ribbon shows the standard deviation of the 64 pixels. The leakage current compensation is deactivated in this measurement.

Workaround and baseline shift

The only solution for these problems is to disable the leakage current compensation for the X-ray measurements. This means that the second differential pair has to be disconnected and its current source $I_{LeakComp}$ has to be deactivated (see Fig. 3.16). In this way the whole feedback and input signal replication is handled by the first differential pair. Constant offset currents, like the sensor leakage current and the feedback mismatch current, are forwarded to the integrator and have to be corrected offline by sampling the current prior to a measurement and storing the pixel values on the PC. Still, the offset currents cause a baseline shift at the preamplifier output and as a consequence they alter the relative threshold of the pixels (see section 3.3.3). A so-called threshold tuning algorithm,

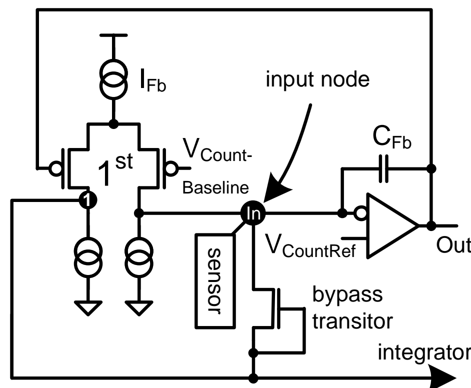

Fig. 3.16: Feedback configuration under X-ray imaging conditions. The fast discharge of the sampling capacitor C_A on CIX 0.2 prevents the use of a more complex leakage current compensation mechanism when a stability over several seconds, e.g. typical turn-on time of an X-ray tube, is required.

described in appendix C, takes the individual baseline shifts into account and sets the discriminator thresholds of the pixels accordingly. Baseline changes that occur after the threshold tuning are a potential source for errors in the counting channel of the detector. Considering all of the aforementioned effects, the chip can be operated successfully in the simultaneous counting and integrating mode but it relies crucially on stable bias and temperature conditions. This is guaranteed by the installation of a small fan next to the detector and heat-up times of larger than one hour. The leaking switches have to be considered as an unwanted feature that would need to be fixed in a future version of the chip.

3.4 CIX 0.2 modules

In the course of this work the CIX 0.2 ASIC has been connected to different Si, CdTe and CdZnTe pixel sensors. This section gives an overview of the sensor types, the module assembly and the obtained CIX 0.2 modules.

3.4.1 Sensor overview

Tab. 3.1 summarizes the sensor's physical dimensions, their metallization and their origin. As indicated, the layout of all sensors is designed to match the CIX 0.2 pixel geometry. All three types include one or several guard rings in order to shield the pixel matrix from unwanted surface currents along the conductive edges of the crystals. The contact metallization, i.e. the first metal layer to be in contact with the actual sensor surface, is made of Pt in the case of the CdTe and CdZnTe sensors. Hence, according to section 2.5.2, the contacts of the Cd(Zn)Te sensors are ohmic.
The Si sensors can be considered a novelty in the field of Si particle detectors as they are made of a high resistivity, p-doped bulk material with highly doped n-implants (labeled n+ in p). Traditionally Si detectors are fabricated from high resistivity n-type bulk material because until recently it was difficult to obtain p-doped bulk material with a high resistivity suited for the fabrication of Si pixel detectors. The bulk resistivity of the Si sensors, used in this work, is above 10 $k\Omega/cm$. The major advantage of such n+ in p sensors is that they are inherently radiation hard as they are immune to type inversion, i.e. the change of p-doped material to n-doped Si due to radiation damages. Fig. 3.17 shows the layout of the CIX 0.2 pixel sensors.

	CdTe	CdZnTe	Si
Pixel number	8 x 8		
Pixel size (mm^2)	500 x 250		
Pixel metal (mm^2)	435 x 185		
Sensor size (mm^2)	5.37 x 2.77		5.3 x 2.9
Guard rings	1		1 top / 11 back
Contact metal	Pt		Al
Thickness (mm)	1.0	3.0	0.3
Surface coating	No	Yes	No
Manufacturer	Acrorad, JP	eVProducts, US	CIS, DE
Date of purchase	2006	2005	2008

Tab. 3.1: Technical specifications of the three CIX 0.2 sensor types.

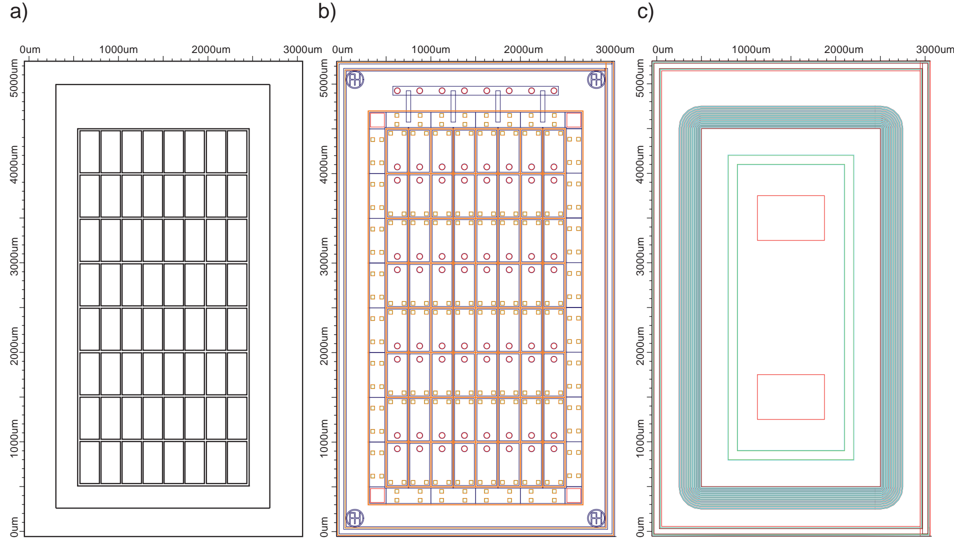

Fig. 3.17: CIX 0.2 sensor layouts. a) Pixel metallization of the CdTe and CdZnTe sensors. b) Pixel-side layout of the Si sensors. The red circles are the openings in the passivation for the gold stud bumps. c): Backside layout of the Si sensors with multi-guard ring structure. Red squares indicate the passivation openings for the HV contacts.

3.4.2 Module assembly

Working with CdTe and CdZnTe sensors places several constraints on the applicable chip-sensor interconnect technologies. First, both materials are temperature sensitive to the extent that the exposure to temperatures above 150°C for longer periods of time (> several minutes) can already significantly decrease the material quality [52]. Therefore conventional solder-based bump bonding techniques with process temperatures in excess of 250°C are ruled out. Secondly, the ASICs and the sensors were shipped in the form of single dies. This constraint makes the use of low temperature Indium bump bonding very difficult as In bump bonding is a wafer-scale process.
A suited interconnect method is the so-called *gold stud bumping technique*. Fig. 3.18 shows the general steps that are involved in this procedure. It starts with the deposit of small gold studs onto the ASIC surface. Typically these studs have diameters on the order of several dozen micrometers with a small section of the original gold wire (typ. 10-20 μm wide) protruding from the top. In some cases the top of the bumps is smoothed by compressing the bump with a flat object (called *coining*). The placement of the individual bumps can be performed on either single die or whole wafers but in the case of wafer scale fabrication throughput becomes an issue. After the bumps are in place, the sensor is positioned above the ASIC and pressed down with a certain force (*flip-chip*), depending on the number of bumps. The forces, which are typically utilized, range on the order of 0.2 N/bump. The tip of the gold studs then forms a permanent bond with the surface of the sensor metallization, which is further facilitated by heating the whole module up to well below the melting point of gold but still high enough to slightly soften the material.
However, CdTe and CdZnTe complicate matters significantly not only due to their thermal constraints, but also because of their mechanical tolerances. If too high forces are applied to the metallization of the sensors, the electrodes can break or loose contact with the sensor surface. This is the reason why the bumps have to be deposited on the chips and why the additional application of ultrasonic vibrations to improve the adhesion of the bumps is prohibited. These low force and low temperature requirements make it

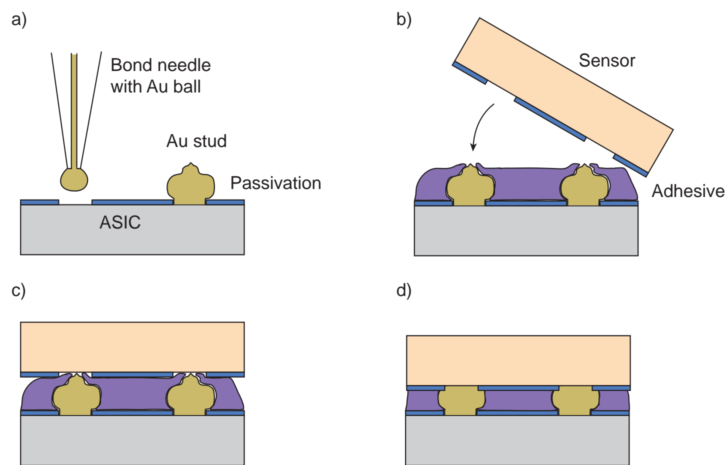

Fig. 3.18: Illustration of the gold stud bump interconnect technology. a) Au stud deposition. b) Optional deposition of an adhesive underfill and flip chip assembly of sensor and ASIC. c) Aligned ASIC and sensor before curing. d) Finished module after curing at low temperature. In case of the CIX 0.2 modules the non-conductive adhesive shrinks and pulls chip and sensor together, improving the contact quality.

almost impossible to achieve a reliable 100 % interconnect yield with the Au studs alone. Therefore an additional underfill in the form of a strong adhesive, which is applied to the chips surface, becomes necessary. The bonding technique used by IZM[6] relies on a non-conductive adhesive that shrinks during curing and thus presses chip and sensor together. This also causes the glue to be pushed away from the contact area between gold bump and sensor metal, establishing a solid electrical connection. The curing of the glue was performed over a long time at low temperature settings, with the maximum value of 150°C only being applied for 2 min. Fig. 3.19 shows a photograph of one of these modules.

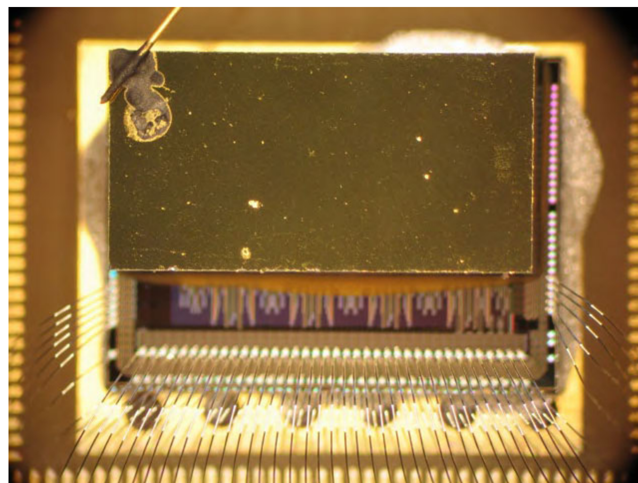

Fig. 3.19: Photograph of a CIX 0.2 module with a 1 mm thick CdTe sensor. The double bond row can be seen at the bottom of the picture. The backside high voltage contact is established with a small gold wire and a carbon based colloid glue.

[6]Fraunhofer Institute for Assembly and Packaging Technologies for Microsystems

Alternatively a so-called *z-axis* adhesive could be used. In this case the glue contains small Ag flakes or small quartz balls (several μm diameter) encased with Ag that form a conductive bond along the axis of force, i.e. between sensor and chip.
A further critical point with respect to the module assembly is the sensor metallization, which should ideally be at least 300 nm thick in order to form a good connection and to resist the mechanical stress during the bonding. Additionally the large height of some of the sensors used in this work (up to 3 mm) makes the flip-chip deposition difficult as it is hard to avoid a tilting of the sensor during the positioning. This can result in unconnected bumps on one side of the chip and totally flattened and therefore shortened bumps on the other side. Hence, only high-precision machines that deposit the sensors vertically are suited for this task. Finally, some manufacturers encase the diced surfaces of their sensors with a hard resin to reduce surface leakage currents and to prevent potential health risks posed by the Cd. Although this prevents Cd-contamination, the resin can melt during the bonding and pose a certain risk to the module when it sticks to the assembly machine.

3.4.3 Module overview

During the course of this work a total of 22 CIX 0.2 modules were assembled. The individual ID-codes, the bump yield and any pecularities of the working modules are given in Tab. 3.2. While the fabrication of the Cd-based modules proved to be rather uncomplicated, the assembly of a working Si module was very difficult. It was found that the Au studs could not establish a reliable mechanical contact on the sensor metallization. Several attempts at chemically and mechanically cleaning the sensor surface yielded no satisfactory result. Different bond parameters and even different bond facilities could not solve this problem. In the end, the measurements had to be performed on a single module with a rather poor bump yield of only 5 %.

Sensor	ID	Bump yield [%]	Remarks
CdZnTe	CZT01	100	instable
	CZT02	75	2 rows defect
	CZT03	100	ok
	CZT04	100	best
CdTe	CdTe01	100	tilted sensor
	CdTe02	100	tilted sensor
	CdTe10	100	no fast r/o
	CdTe11	100	ok
	CdTe12	100	ok
Si	Si03	5	ok

Tab. 3.2: List of the individual IDs and bump yields of the CIX 0.2 modules.

3.5 Chip periphery

The readout system used for the operation of the CIX 0.2 ASIC is a custom design developed by the University of Bonn. It consists of three separate PCBs, namely the USB[7] board, the FPGA[8] board and the supply board, all of which can be seen in Fig. 3.20. The first two PCBs are general purpose devices and are used in several projects of the

[7]Universal serial bus
[8]Field programmable gate array

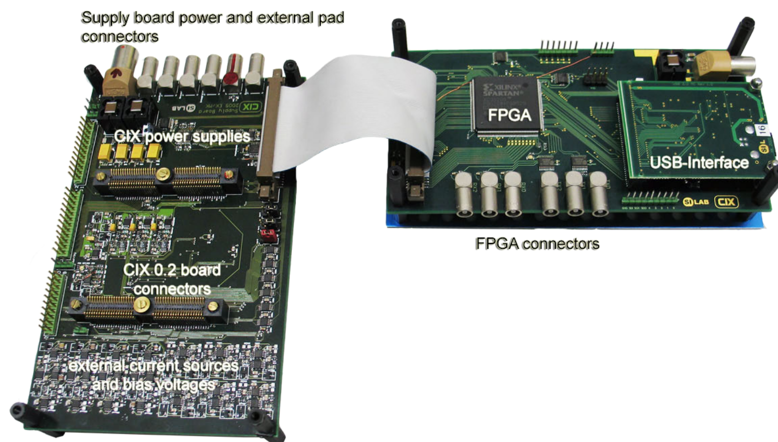

Fig. 3.20: Photograph of the CIX 0.2 readout system. The right-hand side of the picture shows the USB interface board placed on top of the FPGA board. The gray ribbon cable connects the supply board to the FPGA board. A CIX 0.2 sensor can be attached to the supply board by placing its adapter board on spring-mounted connectors and screwing it tight.

laboratory. They provide a sophisticated test bench for an attached ASIC via an USB interface and a C++ software running on a standard PC. The programming of the Spartan III FPGA was done in Verilog HDL[9]. The last component, i.e. the supply board, is custom designed for each type of ASIC and therefore features a number of CIX 0.2 specific components (see left part of Fig. 3.20). As indicated, it includes a number of bias and current source cells, a special socket for the connection of the CIX 0.2 chips, as well as a 32-channel, 14-bit DAC and a dual channel, 16-bit ADC (both located at the backside of the PCB). Furthermore, it is equipped with a number of test pins and external pad connectors for the characterization of the CIX 0.2 ASIC. The chips are fixed to the supply board by means of a three layer adapter PCB (shown in Fig. 3.21). The dense integration of the bond pads of CIX 0.2 with its double pad row at the bottom of the chip is accommodated by two layers of bond pads on the PCB side.
All communications between the readout PC and the chip are handled via the USB interface, which in turn controls three separate bus systems on the PCBs. Fast control signals are generated in the FPGA and routed directly to their respective pins at the ASIC. Slow control signals are sent by two different busses. The SPI[10] carries control signals for the external reference voltages and current sources on the supply board. The ASIC's I^2C interface finally handles the chip register states and the setting of the on-chip DACs. The following list gives an overview of the important features of the readout system:

- Four separate PCBs: USB interface board, FPGA board, supply board and adapter board.
- USB 2.0 protocol
- Xilinx Spartan-III FPGA
- Two 128 kB readout RAMs on FPGA board
- 32-channel, 14-bit DAC on supply board

[9] Hardware description language
[10] Serial peripheral interface

- Dual channel, 16-bit ADC on supply board
- On-board temperature measurement
- Four chip supply voltages
- 8 configurable source monitoring or voltage supply units

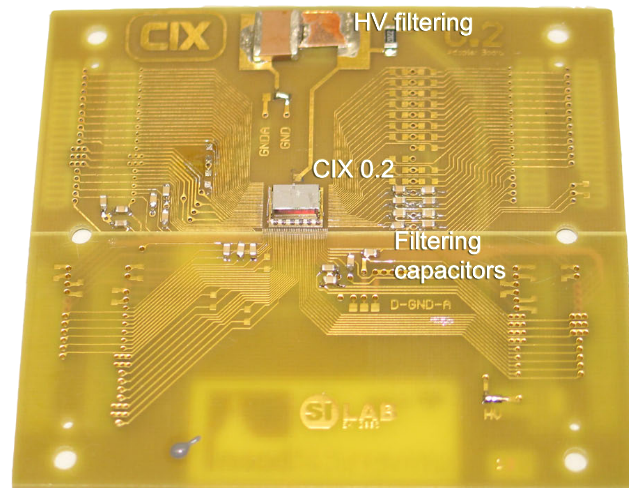

Fig. 3.21: Photo of the CIX 0.2 adapter board equipped with a CIX 0.2 module (middle of the picture). The high voltage is filtered on the board with a 10 nF high voltage capacitor. The remaining passive components on the board are filtering capacitors.

4. ASIC performance - Electrical tests on bumped CIX 0.2 modules

4.1 Measurement conditions

The first step in characterizing the CIX 0.2 sensor modules is to evaluate the impact that the addition of the sensor has on the chip's performance. Therefore the following sections will present measurements that were all performed on bumped CIX 0.2 modules, using on-chip signal generation circuits. This means that the biased sensors acted as a real input load to the ASIC, providing a detector capacitance and a leakage current.
All measurements were performed inside the X-ray cabinet in total darkness and under stable temperature conditions. The variations of the chip's ambient temperature were recorded with a PT100 thermo sensor placed at the backside of the supply board right underneath the chip. All measurements were preceded by a heat-up period of one hour such that the variations of the cabin temperature were below 0.5 K.

4.2 Calibration of the charge injection circuits

One of the design goals of CIX 0.2 was to implement several key components redundantly in order to find the optimal design solutions for specific elements of the chip. This concept was also applied to the charge injection circuits. Fig. 4.1 shows the five different injection blocks that can all be connected to the injection node of a pixel cell. In detail these elements are a constant current source (*leakage simulation*), four clocked injection elements (*net charge switched capacitor*, *current chopper* and two *bipolar switched capacitors*) and two small photo diodes. Normally, under the regular simultaneous counting and integrating condition the integrator is connected to the preamplifier output via the differential feedback. However, if some part of the pixel cell is to be tested individually, the injection network can provide the necessary multiplexing of the signals. For example it is possible to directly test the integrator and bypass the counter feedback by opening switch *EnInjAmp* and at the same time closing switch *EnInjInt*. If the dynamic range of the on-chip signal sources is not sufficient, an additional external pad connector makes it possible to inject signals from external sources. Furthermore, the external pad can also be used to connect the output of the signal sources to off-chip measuring equipment, thus allowing a characterization of the injection circuits independent of the counter or the integrator. As shown in Fig. 4.1, all injection circuits, apart from the sensor connection itself, can be disconnected from the preamplifier input node.
The following sections will introduce the various injection circuits and point out their relevance for the testing and calibration of the CIX 0.2 sensor modules.

4.2.1 Current chopper

The current choppers in the CIX 0.2 pixels are implemented as current sources that can be connected to the pixel's injection node with the help of the *StrCurr* switches. The

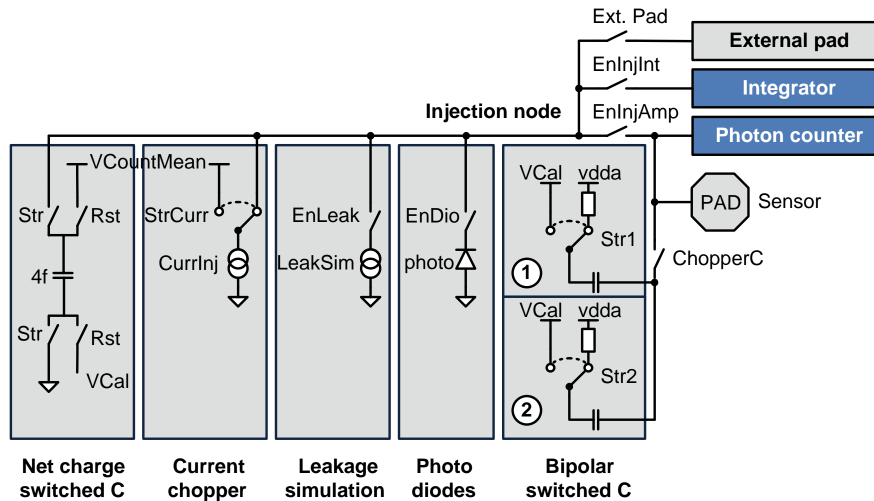

Fig. 4.1: Schematic view of the CIX 0.2 pixel cell charge injection elements. Each pixel includes one circuit that generates a constant current (*leakage simulation*), four clocked injection elements (*net charge switched capacitor*, *current chopper* and two *bipolar switched capacitors*) and two small photo diodes. The sensor pad is directly connected to the photon counter input of the pixel cell. Furthermore, the injection node of one pixel cell can be connected to a separate pad of the ASIC. This pad can be probed with a connector on the supply board.

time during which the switch is closed and the value of the current source determine the injected charge. This simple design makes it possible to achieve very high repetition rates (several MHz) because the maximum injection frequency is essentially only limited by the switching speed of *StrCurr*. As a consequence, this injection circuit was used to measure the chip's maximum count rate.

Fig. 4.2(a) shows the size of the injected charge packets as a function of the *ICurrInj DAC* setting. The values given in the graph represent the average of all 64 *ICurrInj* DACs measured directly with the integrator at a pulser rate of 1 MHz and a duty cycle of 1.5%, i.e. the *StrCurr* switches were closed for 15 ns. These measurements show that the minimum and maximum pulse sizes, which can be generated at these charge pump settings are approximately 1.1 fC and 15.0 fC. The minimum and maximum pulse sizes correspond to *ICurrInj* currents of 66 nA and 1 μA, respectively. Measurements with varying injection times show that a stable operation of the current chopper requires the *StrCurr* switch to be closed for at least 15 ns. For times below this value the switch does not fully open and the injected charge fluctuates.

A second feature of the current chopper is the rate dependence of the pulse size at high pulser frequencies. This is demonstrated in Fig. 4.2(b) using the example of a *ICurrInj DAC* setting of 7 (1.85 fC at 1 MHz) and a 15 ns injection duration. The pulse size gradually decreases as the chopper rate is increased and above 15 MHz a sharp drop in the injected charge can be observed. Below 15 MHz the decrease in the pulse size compared to a frequency of 1 MHz stays below 10%. A possible explanation for this frequency-dependence is a shift of the integrator input node at higher input currents, i.e. pulser rates. In that case, the difference between this integrator input potential and the $V_{CountRef}$ potential at the current chopper could lead to a rate-dependent charge injection. From this it can be concluded that the current chopper has an overall minimum pulse size of approximately 1.1 fC. In addition, the current chopper should only be used to characterize

the maximum count rate of the system up to a repetition rate of 15 MHz. Above this limit the impact of the charge losses on the preamplifier output pulses and thereby on the maximum rate is not negligible.

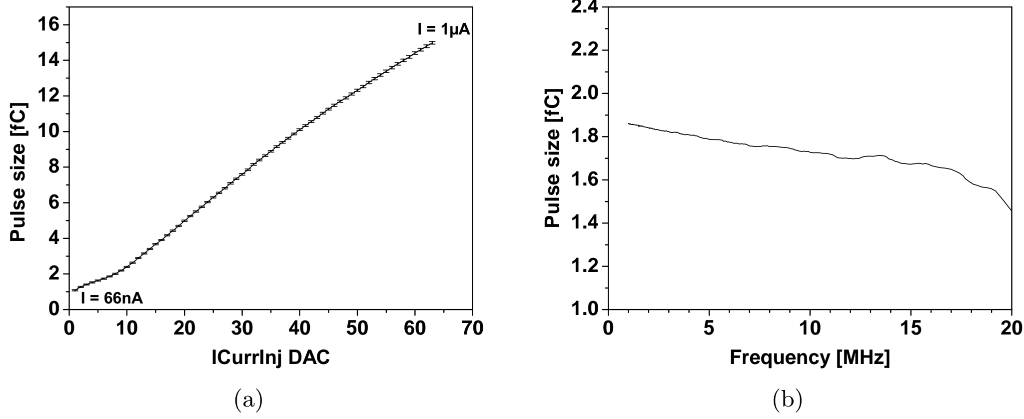

(a) (b)

Fig. 4.2: Calibration of the *ICurrInj* current chopper. The pulse size was measured directly with the integrator by injecting 5000 15 ns pulses.
(a): Average pulse size as a function of the DAC setting at a repetition rate of 1 MHz. The error bars indicate the standard deviation of all 64 pixels.
(b): Pulse size as a function of the pulser frequency at a DAC setting of 7.

4.2.2 Bipolar switched capacitance chopper

The bipolar switched capacitance charge pump can be found in the lower right part of Fig. 4.1. Each pixel features two of these choppers as one of their purposes is the measurement of the chip's double pulse resolution.
The schematic representation shows that the two capacitive choppers in each pixel operate by switching the potential on one side of a capacitor C_{Inj} between $VDDA$ and V_{Cal}. Like this, these choppers generate a bipolar current signal with an integral charge of zero. However, as the current in the $VDDA$ branch is limited by a resistor, the injected bipolar pulses have an asymmetric shape. The long recharge time limits the maximum frequency of this pulser to approximately 10 kHz but it also allows the counter to register the fast component Q_{Inj} of the pulses alone.

$$Q_{Inj} = C_{Inj} \cdot (VDDA - V_{Cal}) \tag{4.1}$$

During the characterization of the CIX 0.2 sensor modules the bipolar switched capacitance charge pump was used primarily for the tuning of the counter thresholds. This tuning procedure is necessary to balance pixel-to-pixel variations in the discriminator thresholds, which are introduced by process variations on the chip. In general the tuning algorithm is based on a threshold scan in which the number of hits that are produced by a fixed number of charge packets of constant size Q_{Inj} as a function of the discriminator threshold Q_{Thr} is registered. A detailed description of a threshold scan and the tuning method can be found in appendix C. Still, it is evident that for this tuning to be successful the precise knowledge of the injected charge Q_{Inj} is required. Ideally Eqn. 4.1 should define the correct amount of charge, however the switching of *Str1* and *Str2* can introduce an additional, unknown amount of charge.
The easiest way to calibrate the injection circuit is to compare its pulse size to the known

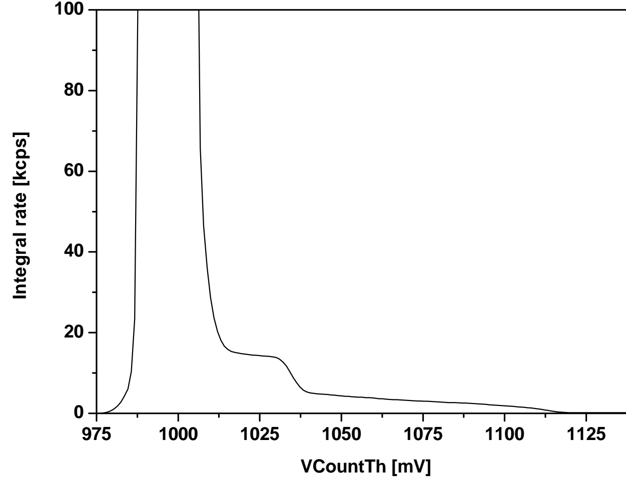

Fig. 4.3: Integral spectrum of capacitive chopper pulses under simultaneous irradiation by 59.45 keV X-ray photons from an ^{241}Am source. The spectrum was recorded by sweeping the discriminator threshold voltage $V_{CountTh}$ at 900 V bias and at a V_{Cal} voltage of 2300 mV.

charge of a radioactive isotope. In this work the 59.45 keV X-ray line of an ^{241}Am (Americium) source served as the charge reference and the capacitive chopper was operated simultaneously to the irradiation. Fig. 4.3 shows the resulting integral spectrum of the capacitive chopper and the ^{241}Am X-ray source. The term integral spectrum refers to the fact that for this type of measurement the discriminator threshold is scanned and at each threshold setting the number of hits is recorded. As indicated in Fig. 4.3, the count rate is dominated by the preamplifier noise at low threshold voltages but as the threshold increases, the capacitive chopper pulses become visible as a plateau. The end of this plateau is marked by a s-shaped threshold curve just like the one described in appendix C. At even higher threshold settings the photon signals can be found.
A derivative of this integral spectrum yields the real energy dependent spectrum as registered by the CIX 0.2 system (see Fig. 4.4). In this plot the chopper peak can be easily identified. Nevertheless, without a reference point it would be impossible to determine the absolute charge of these chopper pulses. This is where the ^{241}Am X-ray signals come into play because the 59.45 keV Am-peak and the 0 keV noise peak set the energy scale of the $V_{CountTh}$ threshold. As will be shown in section 6.4.2, the CdZnTe sensor achieves a charge collection efficiency of 97 % at 900 V bias, i.e. approximately 57.7 keV of the initial 59.45 keV are collected by the detector. The resulting energy calibration is then given by:

$$E[keV] = -495keV + 0.496\frac{keV}{mV} \cdot V_{CountTh}[mV] \tag{4.2}$$

Considering the error on the Gaussian fits to the peaks and the charge collection efficiency, an overall error on the energy scale of 5 % has to be assumed. At this point it is necessary to convert the energy deposition of the photons E_{Dep} into an equivalent deposited charge Q_{Dep}. This is readily archived with the help of the average electron-hole pair production energy $E_{e/h}$ of the sensor material, e.g. 4.64 eV in CdZnTe (see bottom scale in Fig. 4.4).

$$Q_{Dep}[fC] = \frac{0.1602aC}{E_{e/h}[eV]} \cdot E_{Dep}[keV] \tag{4.3}$$

Hence, by measuring the $V_{CountTh}$ positions of the chopper peak as a function of the V_{Cal} voltage, the injected pulse size Q_{Inj} can be interpolated in terms of charge or deposited

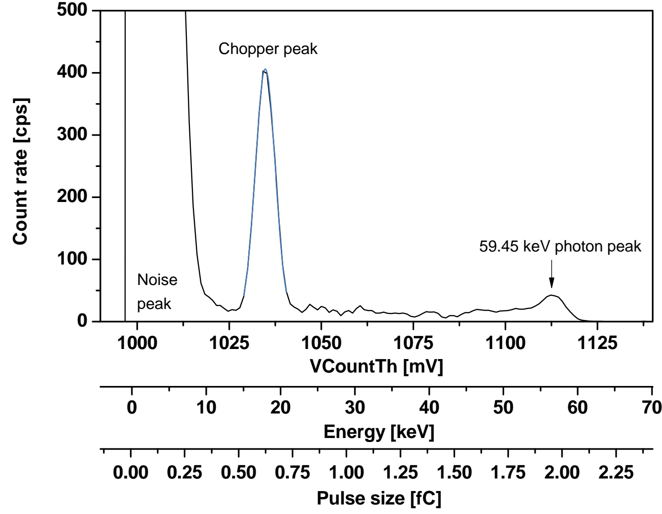

Fig. 4.4: Spectrum of the capacitive chopper and an ^{241}Am X-ray source. The spectrum was obtained by differentiating the integral spectrum shown in Fig. 4.3. The noise peak and the 59.45 keV photon peak determine the energy scale of the $V_{CountTh}$ sweep. The pulse size is given for a CdZnTe sensor based on an $E_{e/h}$ of 4.64 keV.

energy (see Fig. 4.5).

$$Q_{Inj}[fC] = 8.045fC - 3.22 \cdot 10^{-3}\frac{fC}{mV} \cdot V_{Cal}[mV] \tag{4.4}$$

The resulting calibration infers that even if the potential difference between $VDDA$ and V_{Cal} is zero, the capacitive chopper still injects a charge signal of approximately 9 keV when switching.

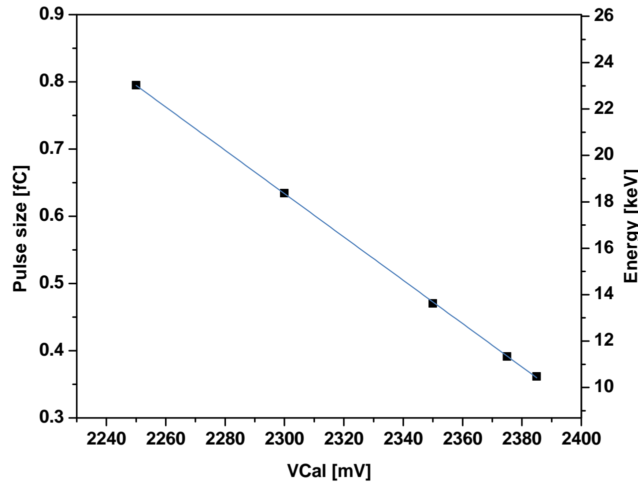

Fig. 4.5: Average switched capacitance chopper pulse size as a function of the V_{Cal} voltage. The pulse size was obtained by measuring the position of the chopper pulses in a spectrum as a function of the V_{Cal} voltage. The right axis shows the pulse size in terms of the energy deposited inside a CdZnTe sensor.

4.2.3 Other charge injection circuits

For reasons of completeness the following gives a short overview of the remaining charge injection circuits.

- *Leakage simulation*
  As the name indicates, this constant leakage current source has been used to simulate the constant leakage current of a semiconductor sensor.

- *Photo diodes*
  Next to each bump bond pad the ASIC features two small photo diodes with areas of approximately 200 μm^2. The purpose of these diodes is enable tests of the bare chips without a sensor. With the addition of the sensors these diodes are covered and inaccessible.

- *Net charge switched chopper*
  The net charge delivering switched chopper circuit is designed to generate unipolar pulses. Compared to the bipolar switched capacitance chopper it consists of a more complex network (see Fig. 4.1), which guarantees that no additional charge is injected when switching. This chopper was not used in this work.

4.3 Dynamic range

The large dynamic range is one of the main advantages of the CIX concept. After the sensors had been connected to the ASICs, this feature was characterized again with the help of the on-chip charge injection circuits. Most of the pulse sizes in this section will be given in keV rather than fC as this facilitates the comparison with the X-ray measurements.

4.3.1 Counter

This section discusses the counter performance as measured with equidistant chopper pulses. The main questions which will be addressed are: How do the different leakage current compensation modes compare in terms of the maximum count rate? How does the workaround for the leaky sampling switches, detailed in section 3.3.6, influence the system's performance? What is the system's maximum count rate at typical settings and which conclusions can be drawn concerning the preamplifier pulse shape?
To start, Fig. 4.6 shows the behavior of the measured count rate as a function of the frequency of the equidistant current chopper pulses. According to the terminology commonly used in medical imaging, a count rate in Hz stands for artificially generated test signals, whereas a rate in counts per second (cps) indicates photon events. Fig. 4.6 illustrates that the number of registered test signals increases linearly with an increasing pulser rate. At an injection rate of approximately 8 MHz the count rate breaks down quickly and drops to zero. This can be understood in terms of pile-up because at a rate of 8 MHz the preamplifier does not discharge completely before the next pulse arrives. As a consequence, the next pulse is superimposed on the remainder of the previous one and the systems output voltage quickly adds up until it reaches the maximum preamplifier output voltage, i.e. the amplifier saturates. At this point the preamplifier output never drops below the discriminator threshold and no further counts are registered. This behavior is also referred to as *pile-up*. The thick line in the plot indicates the module-wide average and from it a maximum count rate of roughly 8 MHz at these specific current chopper and feedback settings can be derived.

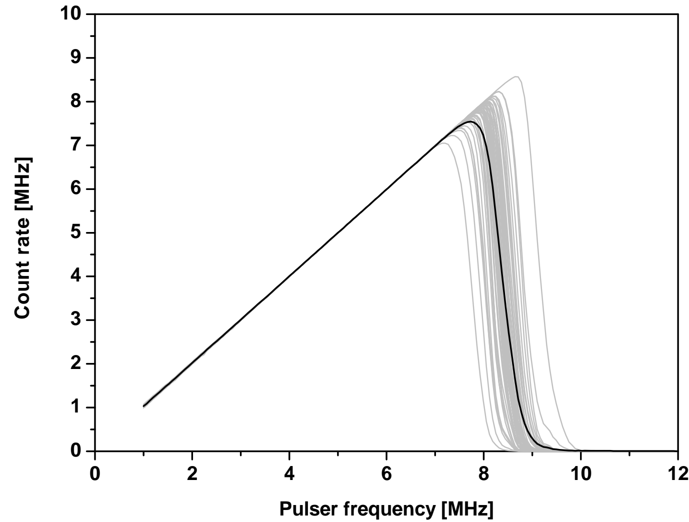

Fig. 4.6: Measured count rate as a function of the current chopper frequency in a 3 mm thick CdZnTe module at 900 V bias. The current chopper injects equidistant charge packets of 2 fC (15 ns on duration). The chip is operated in static leakage current compensation at maximum feedback current settings ($I_{Fb} = 63$) and a threshold of 0.34 fC.

Impact of the leakage compensation mode on the maximum rate

Section 3.3.3 described the different leakage current compensation mechanisms that are implemented on CIX 0.2. Their impact on the system's count rate performance was assessed by exposing them to a series of equidistant test pulses. The data shown in Fig. 4.7 were obtained with a single pixel in a CdTe module into which current chopper pulses with 15 ns duration and 2 fC charge were injected.

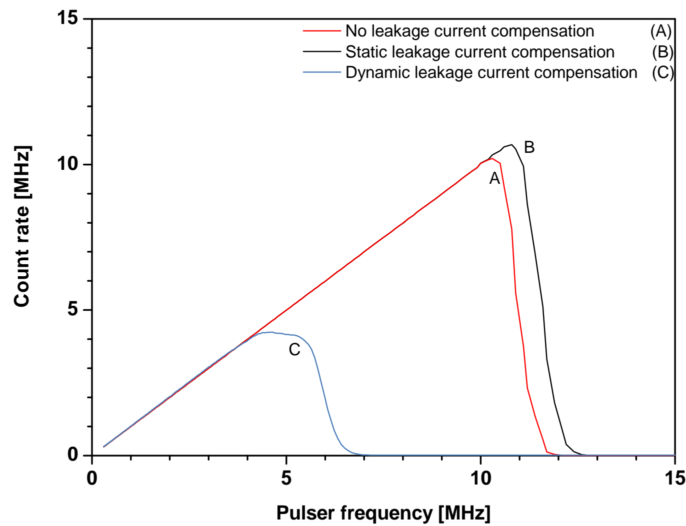

Fig. 4.7: Count rate versus current chopper frequency under different leakage current compensation modes measured with a 1 mm CdTe sensor module. The equidistant charge packets have a size of 2 fC and the discriminator threshold is set to approximately 1.3 fC. The first differential pair is set to $I_{Fb} = 63$ in order to achieve the highest maximum rate performance. $I_{LeakComp}$ settings: 10 (static), 58 (dynamic and controlled redirection).

Starting with the static leakage compensation it is found that the system behaves exactly as expected for a paralyzable counter. The only difference between the static and a deactivated leakage current compensation lies in the achievable maximum count rate, which is slightly higher in the case of the static leakage compensation. This nicely illustrates the advantage of an active leakage compensation as the sensor's leakage current at 400 V bias causes a constant offset at the preamplifier output. The offset effectively lowers the discriminator threshold, which in turn entails a larger time over threshold for the preamplifier signals and thereby a lower maximum count rate.
The lowest maximum count rates are observed with the dynamic leakage compensation. In this case the negative baseline shift (see section 3.3.5) actually overcompensates the signal rate and therefore at higher rates the effective threshold is set too high to register the incoming pulses.
This comparison of the different leakage current compensation modes leads to the conclusion that the static leakage current compensation offers the best performance as it achieves the highest count rates. Still, the difference between static and deactivated leakage compensation is small, such that the workaround for the leaky sampling switches mentioned in section 3.3.6 only slightly reduces the system's performance.

Maximum count rate with equidistant pulses

With the impact of the leakage current compensation qualified, the maximum count rate of the system was evaluated as a function of the pulse size and the discriminator threshold. These measurements were performed with a biased sensor and with deactivated leakage current compensation circuits in order to mirror the detector settings under X-ray irradiation. The feedback was again set to its maximum DAC value of 63 (91 nA) in order to guarantee the highest rate capability. The minimum pulse sizes and threshold settings in these measurements are given by the minimum pulse sizes of the current chopper and the capacitive chopper, respectively.
Fig. 4.8 shows the maximum count rate N_{Max} as a function of the equivalent pulse size E_{Inj} of the injected charge packets in keV. Under the assumption that a counter has a linear relation between the time over threshold and the incoming signal charge or deposited energy, the maximum count rate should decrease linearly for an increasing pulse size. Both curves in Fig. 4.8 are in perfect agreement with this expectation. Linear fits to the data yield the following results:

$$\begin{aligned} &10\ keV\ threshold: \\ &\qquad N_{Max} = (9.84 \pm 0.04) MHz - (0.034 \pm 7 \cdot 10^{-4}) \frac{MHz}{keV} \cdot E_{Inj} \qquad (4.5) \\ &24\ keV\ threshold: \\ &\qquad N_{Max} = (12.2 \pm 0.18) MHz - (0.049 \pm 0.003) \frac{MHz}{keV} \cdot E_{Inj} \qquad (4.6) \end{aligned}$$

Alternatively, a higher threshold should result in a lower time over threshold and a higher maximum rate. As shown in Fig. 4.9 the measurements also confirm this second relation. In this case linear fits of the maximum rate as a function of the $V_{CountTh}$ threshold level give the following equations:

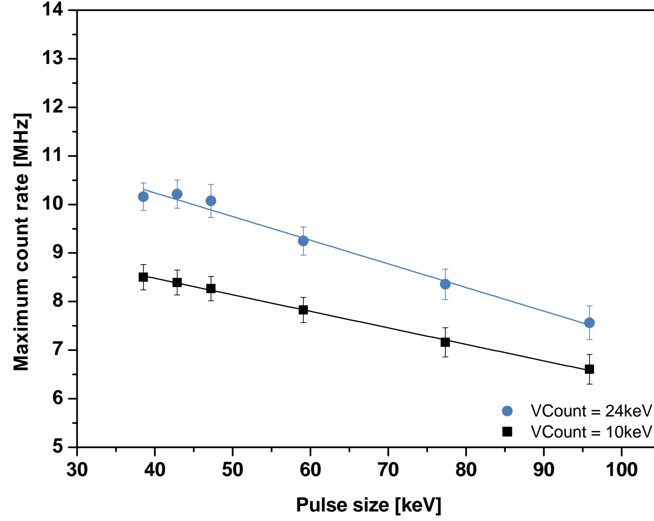

Fig. 4.8: Average maximum count rate as a function of the current chopper pulse size in keV in a 3 mm CdZnTe sensor at two different *VCountTh* threshold settings. The error bars represent the module-wide standard deviation of the maximum rates. Both curves show the expected linear dependence of the maximum rate on the pulse size.

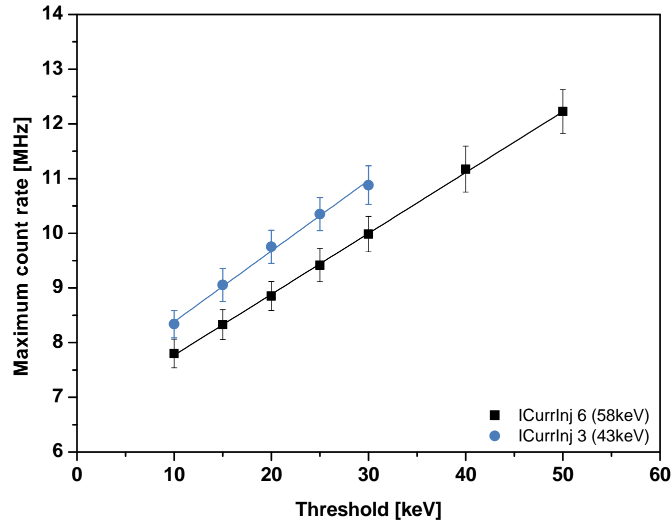

Fig. 4.9: Average maximum count rate as a function of the applied discriminator threshold in keV in a 3 mm CdZnTe sensor at two different current chopper pulse sizes. The error bars represent the module-wide standard deviation of the maximum rates.

$$43\ keV\ pulse\ size:$$

$$N_{Max} = (7.09 \pm 0.09)MHz - (0.129 \pm 0.005)\frac{MHz}{keV} \cdot V_{CountTh} \tag{4.7}$$

$$58\ keV\ pulse\ size:$$

$$N_{Max} = (6.66 \pm 0.03)MHz + (0.111 \pm 0.001)\frac{MHz}{keV} \cdot V_{CountTh} \tag{4.8}$$

These findings infer that the pulse shape of the CIX 0.2 preamplifier output closely follows the theoretical prediction of the triangular shaped signals presented in Fig. 3.5.

Concerning the maximum rate, previous measurements without a sensor connection [1] found a maximum of approximately 12 MHz at maximum feedback settings, a charge packet size of 2 fC (58 keV in CdZnTe) and a 1.3 fC (39 keV in CdZnTe) threshold. The good agreement between this value and the (11.1 ± 0.5) MHz obtained from Fig. 4.9 shows that the addition of the sensor does not influence the maximum count rate negatively.

Discriminator dead time

The evaluation of the maximum count rate in the previous section allows a further characterization of the photon counter. Namely, it is possible to derive the discriminator's dead time. The argument from which this is deduced relies on a geometric reconstruction of the minimum separation between individual preamplifier output pulses at different threshold levels. This in turn requires a schematic representation of the pulses as shown in Fig. 4.10. Note that this particular pulse shape is determined by the operation of the CIX 0.2 feedback, which acts like a switch. To be more specific, if the potential change at the output of the preamplifier is large, the p-MOS in the first differential pair fully opens and the feedback delivers/draws it's maximum current into/from the preamplifier input node. This causes the constant falling slope of the pulses shown in Fig. 4.10. However, for very small potential differences, the p-MOS remains in its linear region and delivers a current proportional to the potential change. Hence, if the discharge of the feedback capacitor nears its end, i.e. the potential difference between the preamplifier output and $V_{CountBaseline}$ in Fig. 3.9 gets small, the discharge current is also reduced and the return to baseline is prolonged. This is indicated by the tailing section of the pulses in Fig. 4.10. Direct measurements of the preamplifier output pulses with a fast oscilloscope [1] as well as the results of the previous section support this model of the pulse shape.
Starting from these prerequisites, the solid lines in the figure show that the minimum distance between two successive pulses is given by the system's maximum count rate at the highest threshold setting. In this case, the preamplifier just manages to clear the charge of the previous pulse before the next one arrives. If the second pulse were to occur any sooner, the system would run into pile-up. The data point at 50 keV threshold setting in Fig. 4.9 yields that in CIX 0.2 two successive 58 keV pulses have to have a minimum separation between the threshold crossings of 82 ns (12.2 MHz). Assuming a rising edge of 15 ns for the individual pulses, this geometrical reconstruction also illustrates that at 50 keV threshold the preamplifier only stays about 10 ns above threshold. The remaining 72 ns are used for the discharge of the first pulse and the rising slope of the next one.

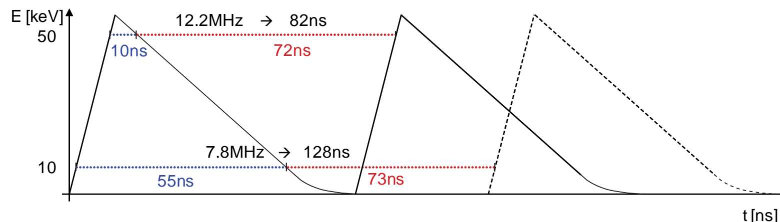

Fig. 4.10: Idealized view of the preamplifier output pulses. Measurements of the maximum count rate indicate that at high threshold settings, the minimum distance between to positive threshold crossings is 82 ns. At a low threshold this period extends to 128 ns although the preamplifier pulse shape is independent of the threshold setting. This means, that at standard settings the discriminator has a dead time of approximately 70 ns between successive pulses.

Considering a very low threshold of 10 keV, a maximum rate of 7.8 MHz is obtained (see data in Fig. 4.9). This means that although the shape of the preamplifier pulses remained unchanged, the lowering of the threshold forces the minimum separation up to 128 ns. In other words, pile-up always occurs if the second pulse arrives at most 82 ns after the first, but at 10 keV threshold the system registers a second pulse only if it comes another 73 ns after the first one has fallen below the threshold.
Both the measurements at high and at low threshold showed that the system stays approximately 70 ns below threshold before the discriminator can register the next pulse. These 70 ns are the dead time of the discriminator. Note that this duration depends on the feedback current and the discriminator DAC values, but as it was measured at standard settings (I_{Fb} = 91 nA, *Comp1* = 13, *Comp2* = 10), it is a measure of the discriminator performance under imaging conditions.

4.3.2 Integrator

The main advantage of the integrator is that its signal processing concept can cope with large input currents. This ability can be tested by connecting the integrator to an on-chip constant current source. A linear fit to the integrator data subsequently allows to qualify the linearity of the integrator's response. This method gives a first impression of the integrator linearity but it is strongly influenced by the linearity of the on-chip current source. A better measure of the linearity, based on X-rays, will be given in section 7.1.2
Fig. 4.11 shows the dynamic range of the integrator as measured with the on-chip $ILeakSim$ constant current source. The measurement was performed on a 3 mm thick CdZnTe module at a bias of 900 V. The results presented in Fig. 4.11 are offset corrected, which means that detector leakage current has been subtracted off-line from the $I_{LeakSim}$ signal current (see also section 3.3.6). In order to directly connect the integrator to the leakage current simulation and at the same time having it connected to the sensor bump pad, the *EnIn-*

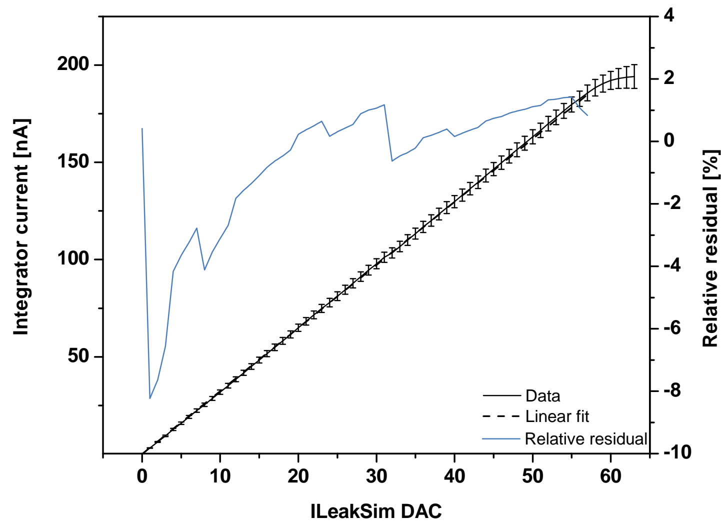

Fig. 4.11: Measured average integrator current as a function of the $I_{LeakSim}$ leakage current simulation source in a 3 mm thick CdZnTe sensor module at 900 V bias. The error bars indicate the module-wide standard deviation. The relative residuals (right axis) are dominated by the non-linearities of the $I_{LeakSim}$ current source. The integrator was operated at a clock rate of 10 MHz and a packet size of 20 fC, yielding a theoretical maximum input current of 200 nA.

jInt and *EnInjAmp* switches were closed and the preamplifier was disabled. The integrator charge pump was set to 20 fC. At an integrator clock rate of 10 MHz this yields a maximum measurable current of 200 nA, i.e. one 20 fC pump event every 100 ns. The measured data show this 200 nA limit, inferring that the per pixel leakage current of the CdZnTe sensors is small compared to 200 nA. The linearity of the integrator (largest relative residual 8 %) illustrates the fact that the sensor connection does not degrade the detector's performance. The sawtooth shape of the residuals is an artifact of the *ILeakSim* DAC, which consists of six different current sources whose strengths are scaled in a binary fashion. This then causes the characteristic steps when switching from one binary configuration of the current sources to another.

4.4 Noise

This section deals with the influence of the sensor connection on the counter and the integrator. Like with the dynamic range, the two signal processing concepts were evaluated individually, i.e. the integrator was connected directly to the signal source bypassing the differential feedback. Detailed information on the noise contribution of the differential feedback can be found in [1].

4.4.1 Counter

Fig. 4.12 shows the counter noise in a CdTe module in terms of the average equivalent noise charge (ENC). The ENC is defined as the number of electrons at the preamplifier input, which are necessary to produce an output signal of the same amplitude as the preamplifier noise. In CIX 0.2 this value can be obtained from a threshold scan while injecting for example 2 fC charge packets at a rate of 10 kHz with the capacitive chopper. As the threshold curve is smeared out by the preamplifier noise, it is therefore possible to determine the ENC by measuring the width of the threshold s-curve given in (C.2). It is found that the preamplifier noise increases linearly with the I_{Fb} feedback current such

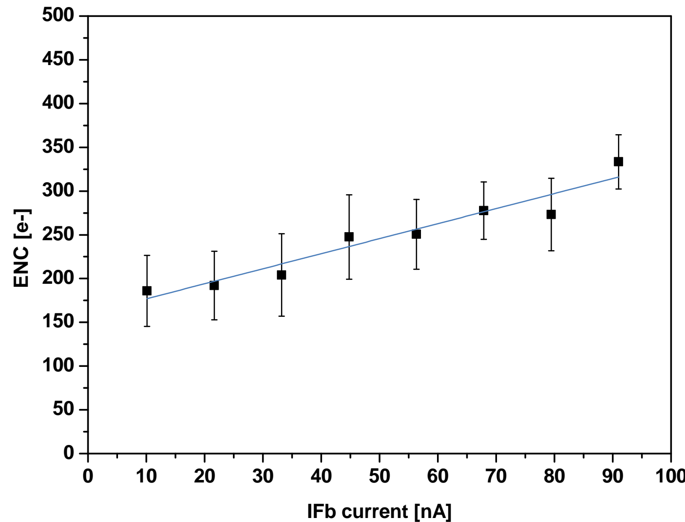

Fig. 4.12: Equivalent noise charge (ENC) as a function of the feedback current I_{Fb}. The error bars represent the standard deviation of all 64 pixels.

Bare ASIC	CdTe module	CdZnTe module
117	320 ± 30	260 ± 30

Tab. 4.1: Equivalent noise charge in bare and bumped CIX 0.2 modules.

that at the maximum feedback settings the system has an ENC of approximately 320 e$^-$.

$$ENC = (160 \pm 7.8)e^- + (1.7 \pm 0.14)\frac{e^-}{nA} \cdot I_{Fb} \tag{4.9}$$

Since the CdZnTe sensors are thrice as thick as the CdTe ones, they possess a smaller pixel to backplane capacitance, which explains the difference between CdTe and CdZnTe. Tab. 4.1 gives an overview of the typical noise values of the CIX 0.2 system at maximum feedback settings ($I_{Fb} = 91$ nA). The ENC of the bare, i.e. unbumped ASIC was reported previously in [1]. Hence, the table indicates that the sensor connection increases the system's noise only by approximately 200 e^-.
CIX 0.2 does not feature additional capacitors that can be connected to the preamplifier input in order to calibrate the dependence of the noise on the capacitive load. Nevertheless, the noise performance of the counter under a varying capacitive load could be characterized with the help of some badly flipped CIX 0.2 modules. In these modules the flip-chip deposit of the sensor on top of the ASIC did not result in a parallel alignment but caused a slight tilt and therefore different distances between sensor and chip along one axis. By using a microscope with a high resolution and thereby a small depth of view, it is possible to measure the separation between chip and sensor around the module edges (see inlay in Fig. 4.13). The strong correlation between a small separation and a large preamplifier noise can be seen in the main plot of Fig. 4.13. It furthermore shows an estimate of the chip-sensor capacitance C_{Estim} based on the simple assumption of a parallel plate

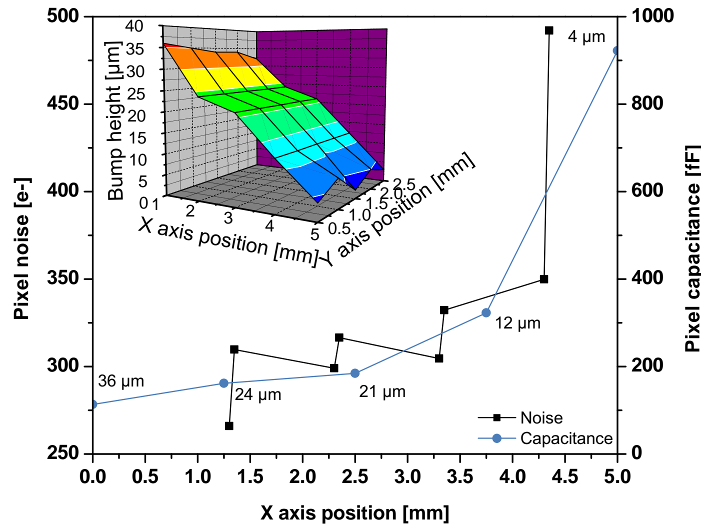

Fig. 4.13: ENC and estimated pixel capacitance as a function of the position along the long (5.7 mm) axis of a CdTe module (CdTe01). During flip-chip the sensor was not deposited parallel to the ASIC surface resulting in different distances between chip and sensor. The insert shows a 3d representation of the chip-sensor distance as a function of the x-y position. The pixel capacitance was estimated by assuming a parallel plate capacitor between chip and sensor.

geometry with distance d and a dielectric constant $\epsilon_{Adhesive}$ of the adhesive of 3.5.

$$C_{Estim} = \epsilon_0 \cdot \epsilon_{Adhesive} \cdot \frac{A_{Pixel}}{d} \tag{4.10}$$

Typical distances between sensor and chip after the module assembly are on the order of 20 μm. The ENC value of 300 e^- at the x-axis position of 2.5 mm (21 μm separation) agrees nicely with the result obtained at identical settings on a well flipped module (see Fig. 4.12).

4.4.2 Integrator

The integrator noise was assessed by determining the standard deviation of 100 identical integrator measurements of a given input current. As this measurement was geared towards a characterization of the integrator noise over its full dynamic range, the signal currents were generated by overwriting the DAC controlled voltage of an on-chip current source with an external voltage source. Otherwise, the coarse 6-bit on-chip DAC stepping would have resulted in only a few data points in the low current regime. Furthermore, the integrator charge pump was set to the minimum value of 2.6 fC such that this study also evaluates the highest achievable precision of the integrator (see (3.6)).
Fig. 4.14 shows the result of this analysis in the form of a logarithmic plot of the noise amplitude versus the input current for four different frame durations. Section 3.3.2 detailed that the frame time directly influences the minimum input current I_{Min}. The minimum input currents for the different frame durations used in this measurement can be found in Tab. 4.2. In order to achieve a better comparability, these minimum input currents were subtracted from the data in Fig. 4.14. It is found that at low frame durations the system's noise increases up to a local maximum, which is situated at approximately twice the minimum input current. This is followed by a section of constant noise up to a few nA, after which the integrator noise rises monotonously. From the lack of a noise plateau

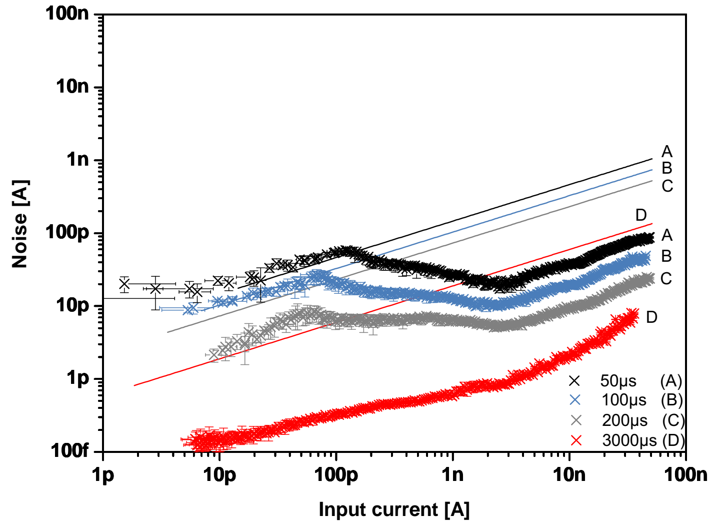

Fig. 4.14: Average integrator noise as a function of the input current in an unbiased 1 mm CdTe module. The input current was generated by a constant current source. In all curves the minimum input current I_{Min} is subtracted. The integrator pump packet size was set to 2.6 fC. The solid lines indicate the Poisson limit in case of an X-ray irradiation with Poisson-distributed 20 keV photons.

50 μs	100 μs	200 μs	3 ms
104 pA	52 pA	27 pA	1.7 pA

Tab. 4.2: Minimum integrator input currents at 2.6 fC pump size.

in the 3 ms measurements at low input currents it can be inferred that the noise at low input currents is dominated by the integrator and not the signal source.
Note that in terms of noise a longer frame duration is equivalent to a longer averaging period. This can be illustrated by considering a constant input current and an additional Gaussian distributed noise current superimposed on this signal. In that case, the fluctuations in the total current cause the *TimeLast* time stamp to vary between successive measurements of the same input current. As this jitter is the result of all fluctuations of the pump times during one frame, a longer frame period essentially averages these fluctuations and thereby reduces the noise. Hence, the 3 ms curve shows the lowest noise.
One important feature of this noise measurement is that it is based on constant currents. Yet, when irradiating with X-rays the signal current will be the result of individual Poisson-distributed photon absorption events. This discrete nature of the input signals causes the fluctuation $\sigma(n)$ in the number of photons per frame n to be:

$$\sigma(n) = \sqrt{n} \tag{4.11}$$

Therefore all figures in this section also include the expected integrator noise based on the photon number fluctuations (see solid lines in the graphs). These values were derived from a simulation of the average photon energy of the Hamamatsu microfocus X-ray tube. Based on this average energy the number of photons per frame necessary to produce a given input current was calculated. Subsequently, the $\sigma(n)$ of these numbers was converted into a fluctuation of the input signal. It is found that the integrator noise exceeds the photon limit only at the smallest input currents in the case of very small frame durations. In other words, the integrator noise is essentially limited by the photon statistics alone, i.e. the system is *Poisson-limited*.
In addition to the measurement above, the integrator performance was also tested with an additional bias current. According to the description given in section 3.3.2, the purpose of the bias current is to meet the minimum input current condition of the system. By using a bias current it is therefore possible to measure currents that would normally lie outside the lower limit of the dynamic range. Note that these measurements furthermore illustrate the noise performance of the integrator under typical X-ray imaging conditions. This is because the operation of CIX 0.2 requires bias currents in order to balance the mismatch of the differential feedback (see section 3.3.6).
Fig. 4.15(a) shows one such measurement in which the bias current is already subtracted from the data. The signal current and integrator settings were identical to the ones in Fig 4.14, with the only difference being the 800 pA bias current ($IntBiasI$ = 1). Compared to the measurements in Fig. 4.14 the data with bias current show a constant noise below 1 nA signal current. This and the fact that the noise in the 3 ms measurement is generally higher with bias current than without, indicates that here the integrator current is dominated by the noise of the bias current source. Above 1 nA an increase in noise, similar to the previous measurement, is found.
Fig. 4.15(b) shows the achievable signal-to-noise ratios when measuring with a bias current of 800 pA. At large frame durations the system registers signal-to-noise ratios ranging from 1 at 1 pA up to almost 10k at 100 nA. Even at very short (50 μs) frames SNRs in excess of 100 can be found.

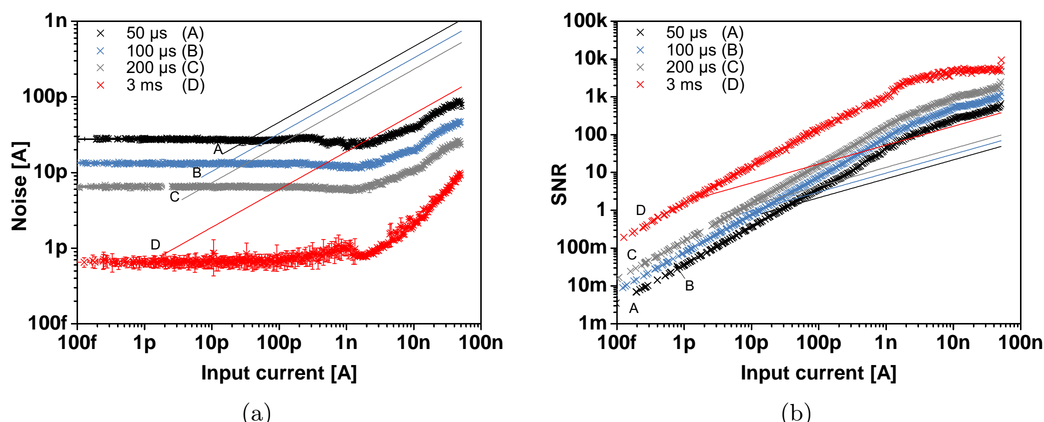

(a) (b)

Fig. 4.15: Average integrator noise (a) and SNR (b) as a function of the input current with an additional *IntBiasI* current. The figure shows results from an unbiased 1 mm thick CdTe module. The bias current of 800 pA is used to guarantee a certain number of pump events per frame, thus allowing the measurement of very small input currents. Solid lines indicate the Poisson limit.

An example of the typical noise amplitudes and signal-to-noise ratios (SNR) with and without bias current at 1 nA input current is given in Tab. 4.3. The table also contains the simulated quantum noise for an average photon energy of 30 keV.
At the end of this section Fig. 4.16 gives an overview of the different factors, which influence the noise measurement. The figure shows the SNR as a function of the input current using the example of a 3 mm thick CdZnTe module. It is found that the best noise performance is achieved with unbumped, bare chips. The addition of an unbiased sensor generally increases the noise by a factor of 2 to 10. At high input currents the difference

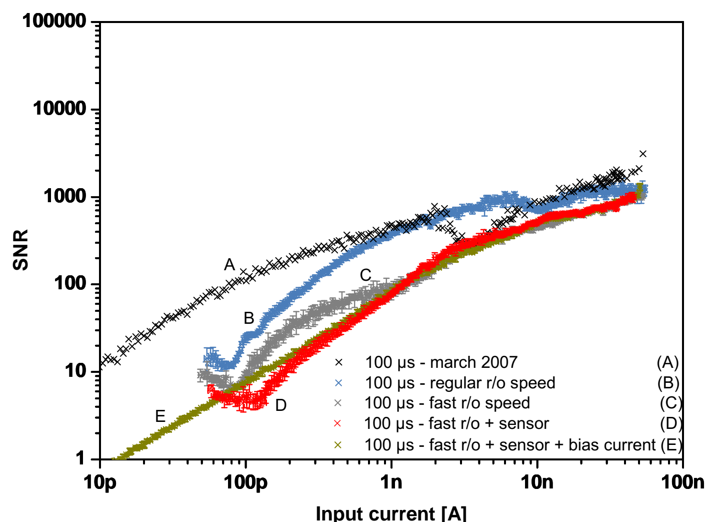

Fig. 4.16: Signal-to-noise ratio (SNR) for different input currents measured on a bare module (a-c) as well as one with an unbiased 1 mm thick CdTe sensor (d,e). The plot shows data taken in march 2007 (a) [1] as well as measurements taken at different *CKInt* integrator clock settings (10 MHz (b) and 20 MHz (c)). The lowest SNRs were measured in the bumped CdTe modules at fast clock settings and with an additional bias current (e).

Frame [μs]	No $IntBiasI$		$IntBiasI$		Quantum noise	
	Noise [pA]	SNR	Noise [pA]	SNR	Noise [pA]	SNR
50	27	37	25	40	149	7
100	13	77	12	83	103	10
200	6.5	154	6	167	74	14
3000	0.6	1667	0.9	1111	18	56

Tab. 4.3: Integrator noise and signal-to-noise ratio at 1 nA input current, 2.6 fC integrator charge pump size and 10 MHz $CKInt$ without and with 800 pA $IntBiasI$ current. The last two columns contain the simulated quantum noise for an X-ray spectrum with an average photon energy of 30 keV.

in noise between the bare chip and the one with a sensor attached is reduced. Finally, the influence of the integrator clock frequency on the SNR can also be identified in the measurements. The data show a significant reduction of the SNR when going from the regular *CKInt* clock setting of 10 MHz up to a frequency of 20 MHz.

5. CIX X-ray test setup

5.1 X-ray tube

The majority of the experiments in this work was performed using X-rays. This section therefore gives a brief overview of the X-ray test setup and its main components.
The left part of Fig. 5.1 shows a photograph of said X-ray test setup. All experiments were performed inside the hermetically sealed phoenix X-ray bench|mate 90 cabinet. The X-rays are generated by an Hamamatsu microfocus X-ray tube, which is installed at the bottom of the cabinet. Hence, the device under test has to be suspended upside down above the tube. Great care was taken to position the center of the detector exactly above the focus point of the X-ray tube in order to avoid shading or even an inhomogeneous irradiation of the device under test. Under measurement conditions a heat-up period of 1 hour was mandatory for the interior of the cabinet to reach a thermal equilibrium. This precaution reduces the temperature variations during one measurement to values smaller than 0.5 °C. The tube parameters are summarized below.

- Maximum acceleration voltage: 90 kVp
- Maximum tube power: 10 W, e.g. 110 μA at 90 kVp

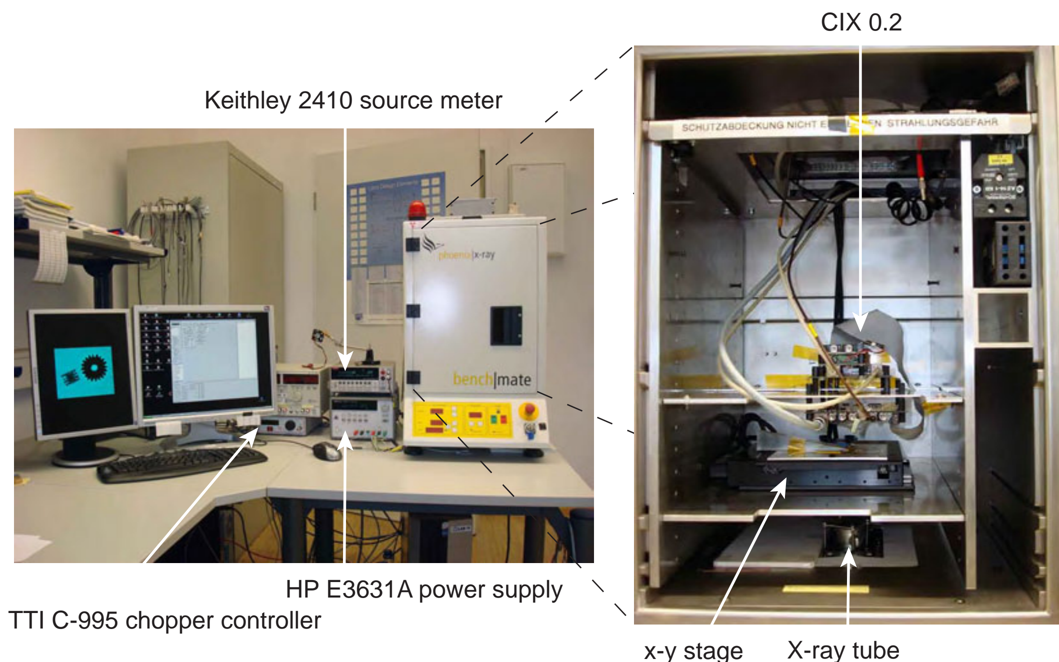

Fig. 5.1: Left: Photograph of the Bonn University X-ray setup.
Right: The inside of the X-ray cabinet with a CIX 0.2 module suspended above the x-y stage and the microfocus tube at the bottom of the cabinet.

- Anode material: Tungsten
- Focal spot size: $< 7\ \mu$m
- Beam cone: 40 °
- Beam filtration: 150 μm Be exit window plus 300 μm Al casing plus 1 mm low energy Al filter

5.2 X-Y stage

As CIX 0.2 has only a very small active area of approximately 4 x 2 mm^2, a commercially available x-y stage was installed inside the X-ray cabinet in order to scan larger objects. The Feinmess KDT-180DC table offers a total travel range of 6 cm in both x and y direction at a precision of 5 μm. Its motion is controlled by the CIX 0.2 control software via the serial RS-232 interface. Due to the limited space inside the X-ray cabin, it allows the scanning of objects up to 2 x 2 cm^2 without the need for user interaction. The x-y stage can be seen in Fig. 5.1.

5.3 Mechanical chopper

A further component, which was installed inside the X-ray cabinet, is the mechanical chopper. This quickly rotating beam chopper is used to modulate the beam of the X-ray tube. Like the x-y stage the TTI C-995-OH chopper is a commercially available system. It consists of a small motor and a thick metal blade with evenly spaced openings. However as the system is normally intended for the modulation of a laser beam, the original 500 μm steel blade is much too thin to provide a significant modulation of hard X-rays. Therefore a special 2 mm thick brass disc with a total of 15 openings was commissioned and the original steel blade was replaced. It achieves an absorption of approximately 98 % of the X-rays that are produced by the tube at maximum voltage settings. Typical chopper frequencies range from a few Hz up to several kHz. Nevertheless, the greatly increased weight of the X-ray chopper disc has to be taken into account when changing the chopper frequency. When equipped with the brass disc the chopper motor takes about 30 s (instead of < 1 s) to reach a constant rotation frequency.
One feature of the chopper system that was extensively used in this study, is the ability to synchronize the chopper motion to an external trigger signal. This allows the chopper motion to be synchronized to the readout of the CIX 0.2 chip. For example, if the chopper motion is synchronized to the beginning of a measurement frame, this measurement will always coincide with the same position of the chopper or in other words the same beam intensity. The addition of a tuneable delay between the onset of a frame interval and the clock signal for the chopper then even allows to shift the frame period with respect to the bright-dark pattern produced by the chopper.
Fig. 5.2 illustrates this principle. It is assumed that CIX 0.2 operates in static leakage compensation, i.e. a sampling interval measures the dark current of the detector and the feedback subtracts this value from a following measurement. These so-called sampling and frame phases are separated by a delay phase. Hence, it is possible to sample the dark current of the sensor with a closed chopper (b), wait for the chopper to open in the delay phase and then take a measurement with the chopper fully opened (c). This workaround allows the use of the static leakage compensation under X-ray irradiation even with the leaky sampling switches (see section 3.3.6) because the switching of the tube beam happens on a millisecond scale.

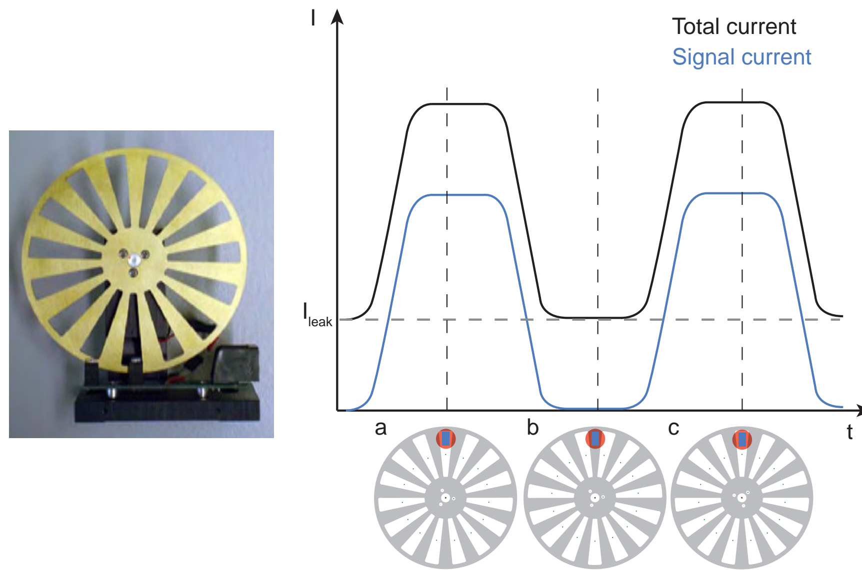

Fig. 5.2: Left: Photograph of the mechanical X-ray chopper.
Right: Illustration of the synchronization between chopper motion and static leakage current compensation. The sketches at the bottom of the figure show the position of the chopper blade for three different moments in time. The position of the CIX 0.2 detector is indicated by the rectangle at the top of the chopper blade. In position (a) the beam passes through the chopper and the detector registers a large current. As the chopper rotates, it subsequently closes (b) and opens (c) again. If the leakage current is sampled during the dark phase, i.e. when the chopper is closed, the measured current can be corrected for the sensor leakage current I_{leak}.

6. Sensor material characterization

6.1 Leakage current

The performance of a detector module depends strongly on the quality of the sensor. One measure of this quality is the sensor leakage current, which will be analyzed in this section. All measurements were performed inside the X-ray cabinet in total darkness and all current values presented herein were obtained in the simultaneous counting and integrating mode, i.e. the integrator was connected to the preamplifier output via the differential feedback.

6.1.1 Bias dependence

The first parameter, which was established, is the applicable bias range of the sensor samples. This was tested in voltage-dependent measurements of the sensor leakage current. Figs. 6.1(a) and 6.1(b) display the average global and pixel leakage currents of a 3 mm thick CdZnTe and a 1 mm thick CdTe sensor. The global currents were measured directly with the high voltage supply (Keithley 2410 source monitoring unit) and the pixel currents were sampled with the integrator. The measurements show that the sensors are capable of sustaining bias voltages of up to 900 V for CdZnTe and 400 V for CdTe. The typical global detector leakage currents, average per pixel currents and the module-wide standard deviations of these pixel currents at the highest bias settings can be found in Tab. 6.1. This overview illustrates that the pixel currents in CdTe and CdZnTe correspond to roughly 1/140 of the total detector currents. Since the obtained ratios lie slightly below the value defined by the pixel area A_{Pix} and the total detector area A_{Det}, this result points towards

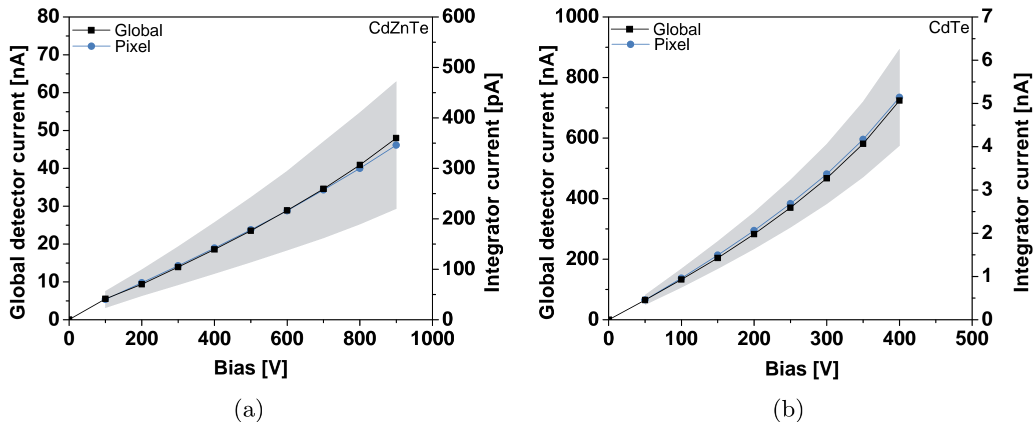

(a) (b)

Fig. 6.1: Average global (left axis) and per pixel (right axis) leakage currents in (a) a 3 mm thick CdZnTe (CZT04) and (b) a 1 mm thick CdTe (CdTe11) sensor as a function of the applied voltage. In case of the pixel currents, the shaded area indicates the module-wide standard deviation. Each pixel in CdZnTe and CdTe registers approximately 1/140 of the global detector current.

Sensor	Per pixel average [nA]	Per pixel std. dev. [pA]	Global [nA]
CdZnTe	0.34	0.125	48
CdTe	5.1	1.1	720

Tab. 6.1: Average per pixel and global detector leakage currents in a 3 mm CdZnTe (CZT04 at 900 V) and a 1 mm CdTe (CdTe11 at 400 V) sensor.

an additional surface current along the edges of the samples.

$$\frac{I_{Pix}}{I_{Det}} = \frac{1}{140} < \frac{1}{119} = \frac{A_{Pix}}{A_{Det}} \tag{6.1}$$

Despite the good agreement in the pixel to global current ratios the leakage currents of CdZnTe and CdTe yield very different absolute values. By comparing the leakage currents at identical electric field strengths (e.g. 300 V/mm), it is found that the resistance of the CdZnTe crystals is approximately 10 times higher than that of the CdTe sensors. This is in excellent agreement with standard material parameters found in the literature (see Tab. 2.4).
Fig. 6.2 shows an identical measurement for a CIX 0.2 module equipped with a 300 μm thick Si sensor. From it an average pixel leakage current of 1 nA and a global detector current of 100 nA at a bias setting of 80 V is obtained. This very low breakthrough voltage of only 80 V is not expected as, according to the manufacturer, the sensors should be able to sustain more than 100 V. The most likely explanation for this is that the sensors suffer from a breakdown in the bias-grid. This implantation on the pixel side is normally used to bias the sensor when testing it with a probe needle on a probe station. In case of a defect it can become conductive and lead to the observed current increase at relatively low voltages. Although this significantly reduces the quality of these sensors, it does not completely prevent their use. Based on the wafer properties, the sensors have a depletion voltage on the order of 80 V and therefore they can still be operated close to full depletion.

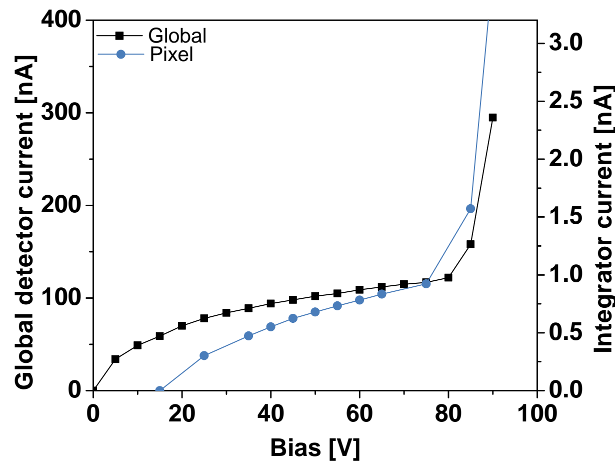

Fig. 6.2: Average global (left axis) and per pixel (right axis) leakage currents in a 300 μm thick Si sensor (Si03). On average the per pixel current amounts to roughly 1/100 of the global detector current. The global as well as the pixel current both show the breakdown behavior of the Si p-n diode at approximately 80 V.

6.1.2 Temperature dependence

All materials that were analyzed in this work show a negative temperature coefficient. As the X-ray setup does not have an active temperature control, the power dissipation of the readout ASIC leads to an increase in the sensor leakage current. It is therefore mandatory to assess the magnitude of the leakage current changes under typical measurement conditions.
Fig. 6.3 shows the temperature change during one hour using the example of a CdTe module. The chip was read out continuously, which causes a maximum power consumption of the ASIC. After approximately one hour an equilibrium value of roughly 44 °C is reached. Different ambient temperatures (22 °C - 25 °C) result in a variation of the plateau value of approximately 3 °C. Note that apart from this particular measurement all measurements presented in this work started from thermal equilibrium in order to keep the variations in the leakage current as small as possible.
The influence of the ambient temperature on the leakage current in CdTe and CdZnTe is illustrated in Fig. 6.4(a) and 6.4(b). The values were obtained by sampling the current during the heat-up phase and plotting them versus the temperature. A linear fit to the data yields an average current increase of 31 pA/K in CdZnTe and 363 pA/K in CdTe at temperatures around 40 °C.

$$I_{Leak}[CdZnTe] = -\,(977 \pm 22)\ pA + (31.1 \pm 0.5)\ \frac{pA}{K} \cdot T \tag{6.2}$$

$$I_{Leak}[CdTe] = -\,(10.9 \pm 0.2)\ nA + (363 \pm 5.5)\ \frac{pA}{K} \cdot T \tag{6.3}$$

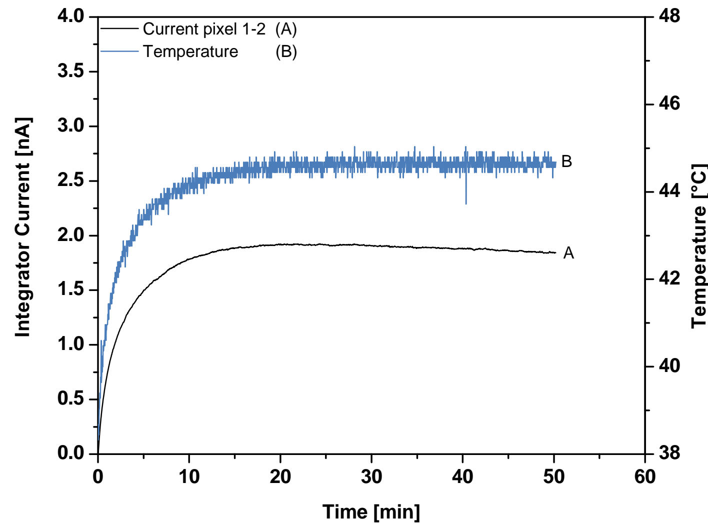

Fig. 6.3: Integrator current (A) in pixel 1-2 of a CdTe module (CdTe11) during a heat-up phase of one hour. At the beginning of the measurement the current was set to zero by an offline subtraction of mismatch and leakage currents. The light blue line (B) shows the temperature of the chip as a function of the time. The plateau value of the thermal equilibrium can vary by approximately 3 $°C$ depending on the room temperature [22 °C - 25 °C].

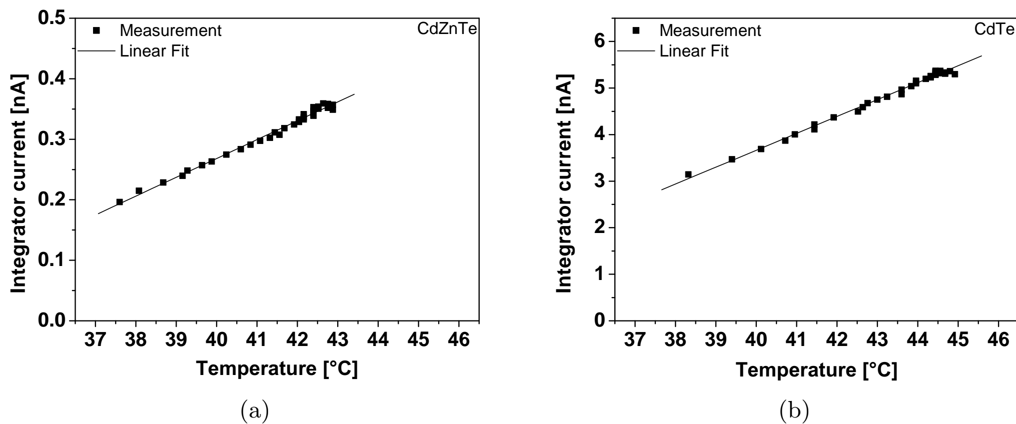

Fig. 6.4: Leakage current in (a) 3 mm thick CdZnTe (CZT04) and (b) 1 mm thick CdTe (CdTe11) sensors versus the ambient temperature of the sensor module. Solid lines indicate linear fits to the data (see (6.2) and (6.3)).

6.1.3 Photon flux dependence

The previous section already illustrated that a constant sensor temperature minimizes variations in the leakage current. Nevertheless, measurements of the leakage current under X-ray irradiation indicate that even under stable thermal conditions, the leakage current is not necessarily constant. In fact, as presented in Fig. 6.5, the leakage current is influenced by the applied photon flux. The data were taken by measuring the global detector current with the Keithley 2410 source monitoring unit 5 s after the tube had been switched on. Following this, the tube was switched off for 10 min before the next measurement was performed. In that way all data points in Fig. 6.5 had identical starting conditions in terms of the sensor leakage current.

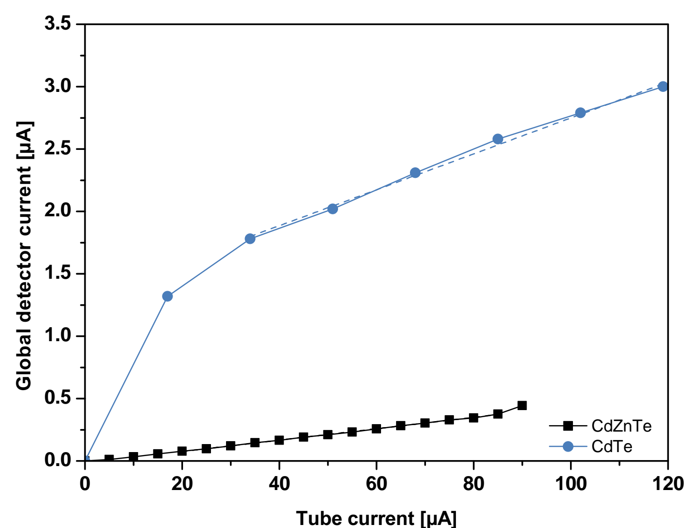

Fig. 6.5: Global detector current under a linear increase of the tube current for 1 mm thick CdTe (CdTe11 - dots) and 3 mm thick CdZnTe (CZT04 - squares) sensors. The detector area is approximately 15 mm^2. The measurements were performed at 90 kVp and 12.5 cm focal spot to detector distance.

Concerning the photon flux dependence the CdZnTe data show the expected behavior, i.e. a linear increase in the tube current leads to a proportional rise in the measured current. In contrast to this, CdTe exhibits a steep increase in the measured current at low fluxes. At approximately 20 μA tube current, the steep increase flattens such that after 5 s of irradiation the CdTe signals are on average 5-10 times larger than those generated in the CdZnTe sensors. This current difference cannot be explained by the 0.21 eV difference in the electron-hole pair creation energy $E_{e/h}$ between CdTe and CdZnTe.
Therefore this behavior, which is observed in all CdTe samples, is a strong indication that the crystals feature an additional, flux-dependent current component. This current cannot be generated directly by the impinging photons, which leads to the conclusion that it has to enter through the detector's electrodes. Hence, if the sensor is considered a black box, this effect can be described as a photon flux dependent change in the sensor's resistivity. In order to further quantify this effect, the expected CdTe signal currents I_{Exp}^{CdTe} were calculated based on the CdZnTe results I_{Meas}^{CdZnTe}.

$$I_{Exp}^{CdTe} = I_{Meas}^{CdZnTe}(1 + 0.05) \tag{6.4}$$

The additional 5 % represent the difference in $E_{e/h}$ of the materials. Subtracting the expected from the measured CdTe signal currents yields the additional current component (see Fig. 6.6). A comparison of these currents to the leakage current without irradiation (see Fig. 6.1(b) at 400 V) allows an assessment of the radiation-induced change in the sensor's resistivity. This means that for example at a tube current of 20 μA at 12.5 cm focal spot to detector distance the sample's resistance is decreased by a factor of 0.57. Fig. 6.6 also shows the ratio of the additional current to the theoretically expected signal current. It is found that starting from an additional current component which is a factor 18 larger than the X-ray signal, the current ratio settles at a factor of 4 at higher fluxes.
When generalizing these results, it is however important to note that this analysis describes the photon induced changes of the current in a CdTe sample at a specific detector bias. The absolute value of the detector current always depends on this bias setting and

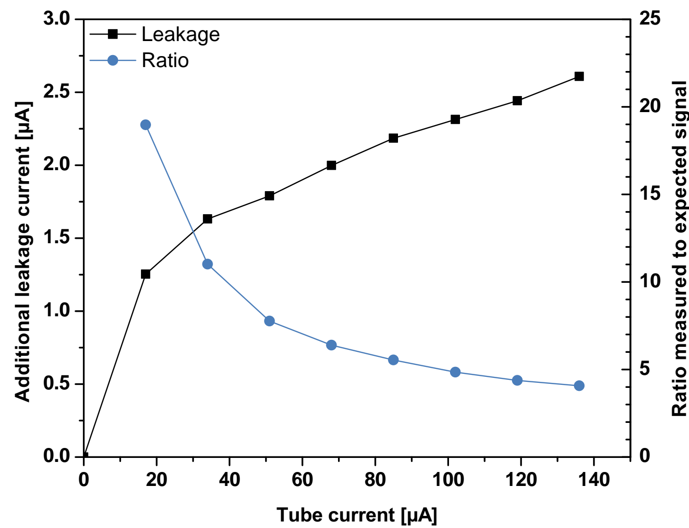

Fig. 6.6: Photon-induced change in the CdTe detector (CdTe11) current in μA after 5 s of irradiation at 90 kVp (left axis). The right axis shows the ratio of the additionally injected current component to the expected signal current of a CdTe sensor. The tube currents are scaled to 12.5 cm focal spot to detector distance.

the irradiation time after which the measurement is taken.
For the simultaneously counting and integrating CIX 0.2 detector such a behavior nevertheless has severe consequences as the sensors are DC-coupled to the readout. If the current changes disproportionally under irradiation, the DC-coupled preamplifier reacts with a baseline shift at the output. This offset causes a lowering of the effective threshold, which can result in a paralyzation of the photon counter at significantly lower fluxes than normal.

6.2 Temporal response

An additional feature, which marks a good sensor material, is a good long-term stability of the response under constant irradiation as well as a rapid response to varying signal intensities.
Fig. 6.7 illustrates these temporal requirements on three X-ray images, which were taken simultaneously with a CdTe module. All three images show a small brass cogwheel placed next to a 8-pin IC measured at 90 kVp tube voltage, 70 μA tube current and a focal spot to detector distance of 16.5 cm. Due to the small physical dimensions of the pixel matrix (2 mm x 4 mm) the objects had to be moved in front of the detector with the help of the x-y stage. During the scans the stage went through an s-shaped path starting at the top right of the images. The full scan of the two objects consists of 9 x 6 individual raster positions and it took approximately four minutes.
Fig. 6.7(a) shows the result of the photon counting channel at a high threshold of 24 keV and Fig. 6.7(b) contains the integrator data. It can be observed that both the photon counter and the integrator images brighten from the top-right to the lower-left corner. This effect is caused by a gradual decrease in the signals (inverted scale) measured with the 1 mm thick CdTe detector as the scan progresses over the objects. It could either be caused by a variation in the sensor signals or it could also be introduced by the ASIC itself. However, as long-term measurements of on-chip generated, constant input signals revealed no drift in the measured signals, the ASIC can be ruled out as a potential source of the observed effect. This leaves the sensor material as the only possible origin of the

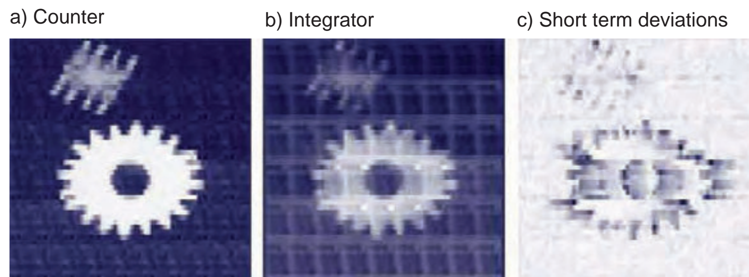

Fig. 6.7: X-ray images of a cogwheel and an integrated circuit taken with a 1 mm thick CdTe sensor (CdTe11) at 90 kVp, 70 μA and 16.5 cm focal spot to detector distance. The images show (a) the photon rate at 24 keV threshold, (b) the integrator current and (c) the integrator current standard deviation of 10 consecutive measurements. All three images were taken simultaneously. The scale is inverted such that dark sections indicate large signals. Due to the small dimensions of the sensor (2 x 4 mm^2) individual images are tiled together with the help of an x-y stage. This also explains the repetitive pattern in the images. Long-term variations in the detector signals can be seen as a gradual brightening of the photon counter and integrator images from top right to bottom left. The short-term effects are best seen in the deformation of the central region of the cogwheel in Fig. 6.7(c).

amplitude changes.
Furthermore, a distinctive rectangular pattern is visible in the integrator image. This is the result of the stitching of subsequent measurements because during irradiation the decrease in signal amplitude varies from pixel to pixel. Tiling the individual measurements to form the large 9 x 6 view then creates the repetitive pattern. Hence, the first two images illustrate the need for a good long-term stability of the sensor signals.
The effect of a slow response to a varying input signal is demonstrated in the third image (see Fig. 6.7(c)). This image shows the fluctuations in the current signals on a short (1 ms) timescale using the dead time free readout of CIX. At each x-y stage position 10 individual snap-shots of that particular image section were taken and the standard deviation of these 10 measurements was calculated. Although the long-term decrease in current amplitude is lost in this measurement, distortions at the edges of the cogwheel are visible. This is because during the imaging procedure the middle section of the cogwheel was scanned going from left to right. Like this the remainders of high current signals from outside the object are superimposed over the low signal section of the cogwheel. Similarly, when moving out of the brass absorber the current signals only slowly return to the high amplitudes.

6.2.1 Long-term response

The afore mentioned long-term change in the detector response of CdTe and CdZnTe was studied in detail for different bias and flux conditions. In these measurements the sensors were irradiated with a constant beam intensity for five minutes. Following this irradiation period, the sensor signals were recorded for another five minutes without irradiation. The irradiation interval of five minutes was chosen as it reflects the typical scan durations when imaging a larger object with CIX 0.2. In order to evaluate the ASIC's performance under such measurement conditions, identical measurements were performed on a 300 μm thick Si sensor. In this context they will serve as a reference since Si is not limited by comparable temporal instabilities. The focus of this analysis is placed on the integrator because of its inherent sensitivity to slow changes in the signal amplitude. In contrast to this, the CIX counter is only influenced indirectly via a preamplifier baseline shift.

Integrator long-term response - Pulse shapes and mathematical description

Fig. 6.8 shows the time dependence of the average pixel current for a Si, a CdZnTe and a CdTe sensor at a tube current of 30 μA at 6.5 cm focal spot to detector distance and at high bias settings. As expected, the Si sensors exhibit no significant temporal changes during or after an irradiation period. This is not true for the CdTe and CdZnTe detectors where a significant time-dependence of the signals is observed. Note that the curves in Fig. 6.8 are representative examples, which were confirmed on other samples of the three sensor materials.
Starting with the CdZnTe detectors, the current under X-ray irradiation I_{On} can be described by a combination of an exponential function with a time constant τ_{On}, specifying the initial amplitude increase, and a linear function, which parameterizes the subsequent rise. The observed linear runaway of the detector currents under irradiation has recently been confirmed in a separate study on CdZnTe samples with high $\mu_h \tau_h$ products at high bias [53]. At the end of the 5 min irradiation period, the current I_{Off} quickly drops down to a few percent of the current under irradiation and then slowly returns back to the baseline following an exponential tangent with the time constant τ_{Off}^{long}. Even on a timescale of one hour no current undershoot after tube shut-off is observed. The mathematical de-

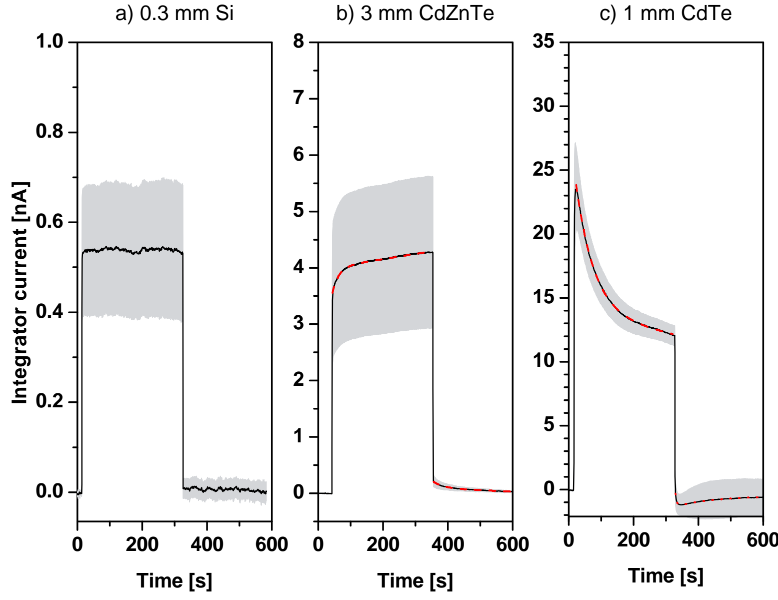

Fig. 6.8: Average integrator currents for (a) Si (Si03), (b) CdZnTe (CZT04) and (c) CdTe (CdTe11) sensors at high flux X-ray irradiation. A 5 min irradiation period at constant tube settings was followed by a 5 min recovery phase without X-ray irradiation. The dashed lines are fit curves to the experimental data. Detector bias: Si = 50 V, CdZnTe = 900V, CdTe = 400 V. The measurements were performed at 90 kVp and 30 μA at 6.5 cm focal spot to detector distance.

scription of the signal shape is given by the following two equations in which A - D are parameters depending on the photon flux and the sensor bias.

$$I_{On}^{CdZnTe} = A - B \cdot exp\left(-\frac{t}{\tau_{On}}\right) + C \cdot t \tag{6.5}$$

$$I_{Off}^{CdZnTe} = D \cdot exp\left(-\frac{t}{\tau_{Off}^{long}}\right) \tag{6.6}$$

The long-term behavior of the CdTe modules is shown in the right part of Fig. 6.8. Here, the CIX measurements exhibit a slow exponential decrease in the signal amplitude with a time constant τ_{On}. Once the tube is switched off, the signal current quickly decreases and even reverses its sign before slowly returning to the baseline value. A good approximation of this undershoot is given by two exponential functions, one describing the fast component (τ_{Off}^{short}) and a second one for the long-term contribution (τ_{Off}^{long}). In the following two equations the parameters E - F again depend on the photon flux and the sensor bias.

$$I_{On}^{CdTe} = A + B \cdot exp\left(-\frac{t}{\tau_{On}}\right) - C \cdot t \tag{6.7}$$

$$I_{Off}^{CdTe} = -E + D \cdot exp\left(-\frac{t}{\tau_{Off}^{short}}\right) + F \cdot exp\left(-\frac{t}{\tau_{Off}^{long}}\right) \tag{6.8}$$

The aforementioned equations were used to fit the signal shapes given in Fig. 6.8. This allows an assessment of the observed long-term changes with respect to their characteristic time constants and their relative impact on the signal amplitudes. The time constants τ_{On} and τ_{Off} are obtained directly from the fits while the relative amplitude changes R_{On}

and R_{Off} are defined as follows.
R_{On} describes the relative amplitude change under irradiation caused by the exponential terms in (6.5) and (6.7). The linear part of the two equations has been neglected as this would introduce an additional time-dependence. Hence, R_{On} is defined as:

$$R_{On} = \frac{I_{On}^{exp}(t \rightarrow \infty)}{I_{On}^{Ref}(5\ s)} = \frac{A}{I_{On}^{Ref}(5\ s)} \tag{6.9}$$

The reference amplitude $I_{On}^{Ref}(5\ \mathrm{s})$, to which the exponential component of this fit is compared, was chosen such that it lies outside the parts of the signals, which are dominated by the switching of the X-ray tube. This accounts for the one or two seconds necessary for the X-ray tube to reach the desired acceleration voltage and tube current.
Regarding the amplitude change after the tube has been switched off, the different pulse shapes in CdZnTe and CdTe require different definitions of R_{Off}. In CdZnTe it is given by:

$$R_{Off}^{CdZnTe} = \frac{I_{Off}(5\ s)}{I_{On}^{Ref}(299\ s)} \tag{6.10}$$

Like this the residual signal 5 s after tube shut-off is referenced to the signal amplitude immediately before the tube is switched off.
Due to the negative undershoot the respective quantity in CdTe is defined as:

$$R_{Off}^{CdTe} = \frac{I_{Off}^{Min}}{I_{On}^{Ref}(299\ s)} \tag{6.11}$$

Thus, R_{Off}^{CdTe} gives a measure of the maximum negative signal amplitude after tube shut-off with respect to the signal under irradiation.
Tab. 6.2 summarizes the time constants and relative amplitude changes in CdZnTe and CdTe. The values given in this table represent the averaged fit data of 64 pixels (one module) in CdZnTe and 128 pixels (two modules) in CdTe. Note that although these results allow a direct comparison of the different sensor types that were used in this work, a generalization to any kind of CdTe and CdZnTe sensor is difficult as differences between sensor batches and manufacturers are to be expected. Moreover, the values stated in the table depend on the bias settings (here CdTe: 400 V and CdZnTe: 900 V), the photon spectrum (here 90 kVp) and the photon flux (here 30 μA at 6.5 cm focal spot to detector distance).
Nevertheless, considering all the aforementioned constraints, Tab. 6.2 gives some valuable information on the performance of the sensor materials used in this work. It is found that in both sensor materials the long-term changes during irradiation occur on time scales similar to those after irradiation. Furthermore, the data indicate that CdTe suffers from longer lasting as well as more pronounced amplitude changes compared to CdZnTe.

	τ_{On}[s]	$\tau_{Offlong}$[s]	$\tau_{Offshort}$[s]	R_{On}(%)	R_{Off}(%)
CdZnTe	20	33	x	13	5
CdTe	65	78	3	39	-9

Tab. 6.2: Average exponential time constants τ and relative amplitude changes R in CdZnTe and CdTe during a 5 min irradiation period at 90 kVp, 30 μA and 6.5 cm focal spot to detector distance. The sensor bias was 900 V (CdZnTe) and 400 V (CdTe). The presented values are the average of 64 pixels (one module) in CdZnTe and 128 pixels (two modules) in CdTe. More information on the parameters τ and R is given in the text.

Integrator long-term response - Explanatory approach

One possible explanation for the observed long-term behavior of the integrator currents could be a slow heating of the detector. However, this hypothesis is considered unlikely as the temperature-dependent measurements of the pixel leakage current yielded a current increase of 31 pA/K in CdZnTe (see section 6.1.2). This means that the linear increase in Fig. 6.8 alone would constitute a temperature change of 10 K. Since the temperature variations under measurement conditions were only 0.5 K and the energy deposited by the X-ray beam inside the detector is 1 μW, thermal changes are not the correct explanation. An alternative explanation is given by a model based on the charge carrier injection through the metal contacts [54]. In detail, the authors argue that the accumulation of space-charges inside the sensor can influence the current entering through the sensor's electrodes. The general presence of a positive space charge inside CdZnTe sensors has been confirmed by recent works on the polarization effect and the electrical field profile (see section 2.5.2). Hence, by applying the contact model to CdZnTe, the pulse shapes can be understood in terms of an electron current, which enters through the cathode and which is modulated by the magnitude of the positive space charge in the sensor.
Fig. 6.9 illustrates the model in terms of the signal current, the space charge distribution and the electric field profile before, during and after an irradiation interval. Prior to the irradiation (t_1) the detector features a certain space charge and a current flowing through the contacts (see also Fig. 6.9.d). If irradiated (t_2 and Fig. 6.9.e), the trapped charge carriers increase the space charge inside the detector. The larger internal charge corresponds to a higher electric field at the cathode, which in turn causes a larger electron injection through the non-blocking contacts. After the tube is shut off (t_3 and Fig. 6.9.f) the gradual detrapping of the accumulated charge decreases the electric field strength at the contact. Hence, the current slowly returns return back to the baseline.
A first confirmation of this hypothesis can be found in a bias-dependent measurement of the integrator signals (see Fig. 6.10(a)). The analysis reveals that both the exponential increase as well as the subsequent linear rise scale with the applied bias. Similarly, the

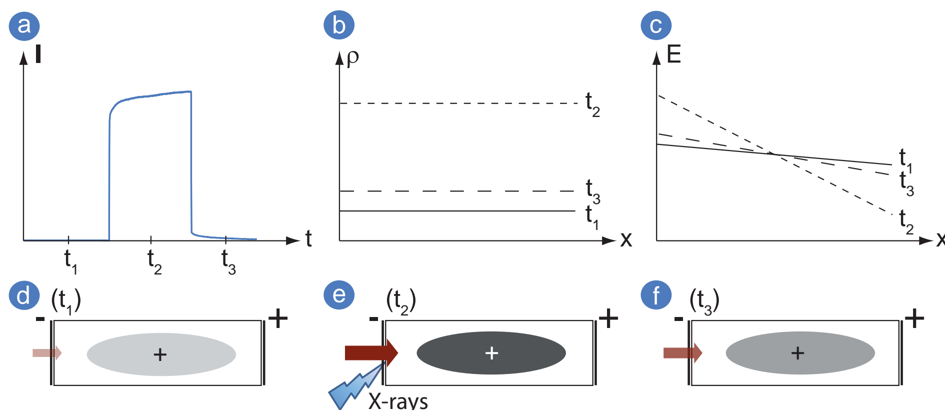

Fig. 6.9: Possible explanation of the long-term behavior of the current signals in CdZnTe. (a): Typical pulse shape of the CdZnTe signals. (b): Space charge density ρ at three different times t_1 - t_3. (c): Electric field profile E at t_1 - t_3. The three figures (d-f) at the bottom show a graphical representation of the sensor at the three moments in time. The color saturation of the arrows and the ellipsoids symbolizes the injected current and the space charge density, respectively. Under irradiation, the space charge increases and thereby increases the current, which flows into the detector. After the irradiation period, detrapping causes the space charge to slowly return to the pre-irradiation value.

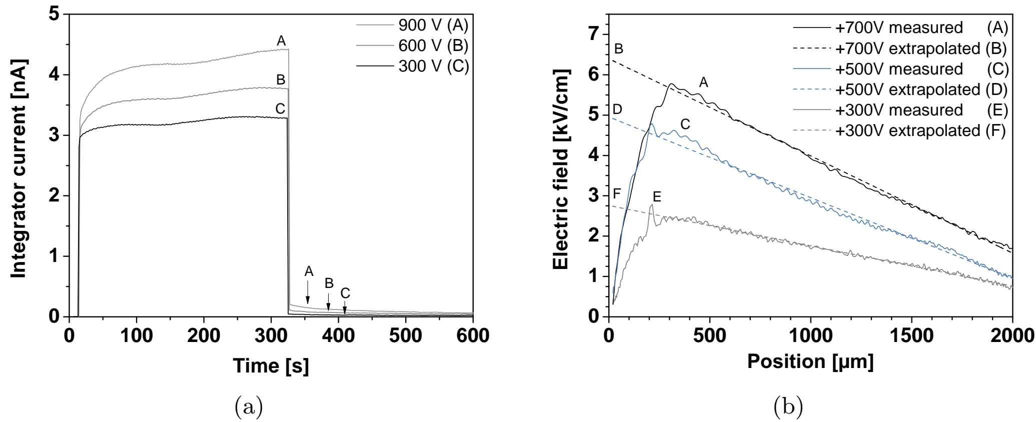

(a) (b)

Fig. 6.10: (a): Average long-term integrator current response of a 3 mm thick CdZnTe detector (CZT04) at different bias settings. The temperature variations during the measurement were smaller than 0.5 K. Tube settings: 90 kVp and 30 μA at 6.5 cm focal spot to detector distance.
(b): Electric field profiles in a 2 mm thick single channel eV Products CdZnTe sensor measured with the TCT method [2].

absolute value of the residual current amplitude after tube shut-off also increases with the bias voltage. According to the aforementioned injection model, this can be explained under the assumption that a higher bias facilitates the charge carrier injection through the cathode via a larger space charge in the detector. The general bias-dependence of the space charge in CdZnTe is supported by TCT measurements on single channel detectors from the same manufacturer (see Fig. 6.10(b)) [2,41]. These measurements illustrate that the slope of the electric field profile increases with increasing bias, which can only be caused by a larger space charge inside the detector. It can therefore be concluded that the long time response of CdZnTe at different bias settings agrees with a space charge controlled injection model.
Another finding, which points towards a contact effect, is that the observed long-term changes are also influenced by the applied photon flux. The left part of Fig. 6.11(a) shows four consecutive 5 min irradiation periods, each of which is characterized by a signal shape similar to the ones shown in the previous figures. It can be seen that the relative amplitude increase gets larger with a rising photon flux. According to the injection model this is to be expected because a larger photon flux results in a larger number of trapped charges inside the detector. The larger space charge in turn causes a stronger manipulation of the current, which flows through the electrodes. This effect is quantified in Fig. 6.11(b) where the signal current after 30 s of irradiation is compared to the current 5 s after the tube had been switched on. The data show that the signal amplitude increases by more than 15 % within the first 30 s of irradiation. Hence, in terms of the long-term stability of the integrator signals a low bias setting as well as a low photon flux is favored.
Apart from further supporting the contact model, Fig. 6.11(a) yields a second result. It shows that the signals above 50 μA deviate significantly from the signal shape parameterized by (6.5) and (6.6). This implies that the mathematical description of the signal shapes is only valid up to about 50 μA at 6.5 cm focal spot to detector distance.
The aforementioned injection mechanism can also be applied in order to explain the behavior of the CdTe samples. Like with CdZnTe, previous measurements on CdTe crystals from the same manufacturer revealed the presence of positive space-charges inside the

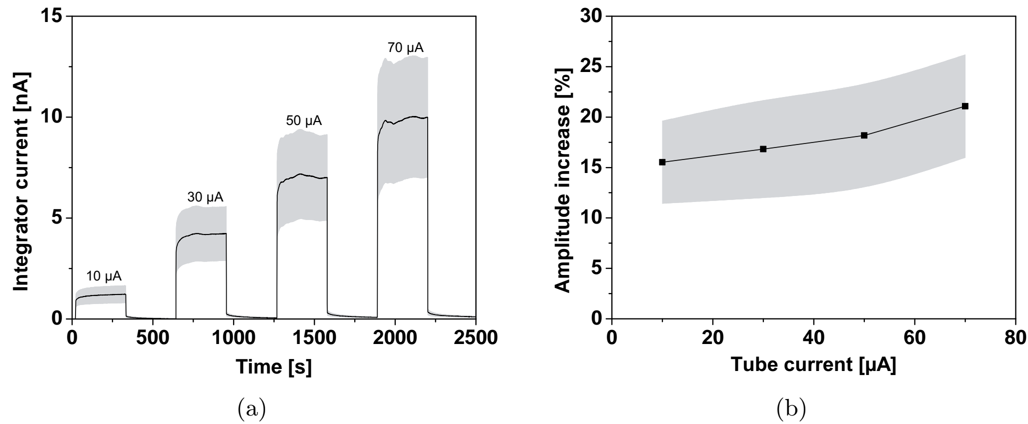

Fig. 6.11: (a): Average long-term integrator current response of a 3 mm thick CdZnTe detector (CZT04) at different tube fluxes.
(b): Relative amplitude gain after 30 s of irradiation. The value is given with respect to the current after 5 s of irradiation.
The module-wide standard deviation is indicated by the shaded areas. The temperature variations during the measurement were smaller than 0.5 K. Tube settings: 90 kVp and 30 μA at 6.5 cm focal spot to detector distance.

sensor volume [2] (see also section 2.5.2). However, the different pulse shapes compared to CdZnTe can only be explained by a blocking space charge (see Fig. 6.12). This means that the accumulated positive charge has to act on a hole current, which flows through the anode. In that case, the current is reduced under irradiation because the larger space charge hinders the hole injection (t_2 and Fig. 6.12.e). Immediately after the X-ray irradiation period (t_3 and Fig. 6.12.f) the residual trapped charge still prevents holes from entering the detector, thus keeping the dark current below the pre-irradiation value. As

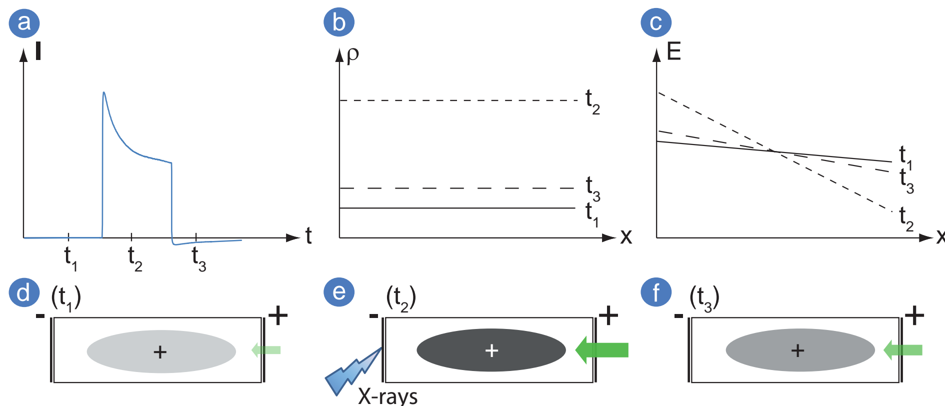

Fig. 6.12: Possible explanation of the long-term behavior of the current signals in CdTe. (a): Typical pulse shape of the CdTe signals. (b): Space charge density ρ at three different times t_1 - t_3. (c): Electric field profile E at t_1 - t_3. The three figures (d-f) at the bottom show a graphical representation of the sensor at the three moments in time. The color saturation of the arrows and the ellipsoids symbolizes the injected current and the space charge density, respectively. Under irradiation, the space charge increases and prevents holes from entering the detector. After the irradiation period, the remaining space charge still suppresses the injection current. This causes the negative undershoot with respect to the pre-irradiation conditions.

the trapped charge is eventually released during the relaxation period, the current slowly returns to the original value.
This too is supported by bias dependent measurements of the long time behavior of CdTe samples under irradiation. The measurements indicate that the relative magnitude of the amplitude change in CdZnTe also increases at higher bias settings. Similar to CdZnTe, this is in accordance with the injection hypothesis, in which the higher electric field and the accompanying larger space charge aggravate the impact of the injection current on the signal shapes. A general estimate of the change in the space charge density introduced by different bias settings can be found in [41]. These TCT measurements on a CdTe sample showed that the charge density scales proportionally to the applied bias.
It should also be noted that although the measurements in Fig. 6.8 were performed at identical photon fluxes, the CdTe currents at the onset of the irradiation period are roughly seven times larger than the currents in CdZnTe. This is consistent with the current amplification by the CdTe sensors described in section 6.1.3.
Hence, summarizing the above, it is found that the measurements all support a space charge modulated current injection as the origin of the observed long-term effects.

Photon counter long-term response

Fig. 6.13 shows the temporal responses of the photon counting channels in a Si, a CdZnTe and a CdTe module. The previous measurements already illustrated that the signal currents exhibit large changes under X-ray irradiation at high flux. At a tube current of 30 μA and a focal spot to detector distance of 6.5 cm the resulting baseline shift at the

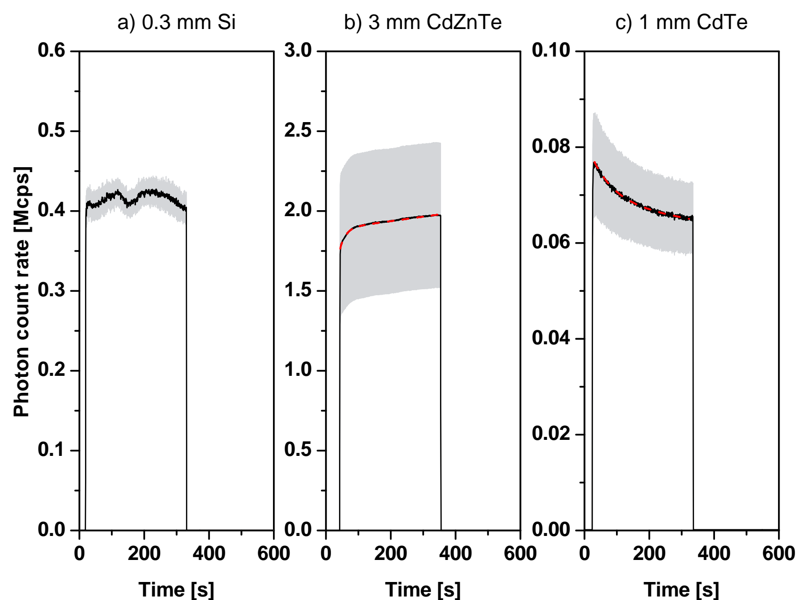

Fig. 6.13: Average photon count rates for (a) Si (Si03), (b) CdZnTe (CZT04) and (c) CdTe (CdTe11) sensors under X-ray irradiation. The Si and CdZnTe sensors were tested with a 90 kVp spectrum at a tube current of 30 μA and at 6.5 cm focal spot to detector distance. The counter threshold was set to 10 keV. As the temporal changes in the signals of the CdTe sensors are much more pronounced, they were tested at 10 μA at 16.5 cm distance (1.6μA at 6.5 cm). The dashed lines are fit curves to the experimental data. Detector bias: Si = 50 V, CdZnTe = 900V, CdTe = 400 V. The most likely explanation for the artifacts in Fig. 6.13(a) is cross-talk from the shortened pixels into the working ones.

preamplifier output is large enough to cause a complete paralyzation of the photon counter. Hence, the photon counting channel in the CdTe modules had to be tested at a reduced tube current of 10 μA and a larger focal spot to detector distance of 16.5 cm.
Concerning the shape of the photon counter responses, the general trends observed with the integrating channel during irradiation are reproduced in the counting measurements. The reason for this is that the variation in the input current causes a baseline shift at the preamplifier output. The change of the relative discriminator threshold then leads to the observed changes in the count rates.
The main difference between the counter and integrator measurements is the absence of residual signals after tube shut-off. The lack of these signals can be easily understood by considering the origin of these afterglow signals. Essentially, they are based on the detrapping of individual charge carriers from deep traps within the band gap of the sensor material. The resulting slowly varying detrapping current does not pass the discriminator threshold and thus a complete shut-off of the X-ray tube does not reveal an afterglow signal in the counter. In case of an AC-coupled photon counting detector, the impact of long-term variations would be even further reduced by the high-pass filtering of the input signal.

6.2.2 Short-term response

This section discusses the short-term behavior of the detector signals (compare with Fig. 6.7(c)). In the following measurements the quickly rotating beam chopper was used to provide a rapidly changing intensity profile similar to a high contrast object. Individual data points were taken continuously at intervals of 500 μs with the help of the chip's dead time free readout.
Fig. 6.14(a) shows the photon counter response of Si, CdTe and CdZnTe modules. All curves have, to a good approximation, a rectangular shape without any short-term variations. The slopes at the beginning and at the end of the irradiation period are governed by the motion of the chopper disc and give no indication of an initial spike as found in [55]. The counts in the dark phase of the chopper cycle originate from X-rays, which are scattered from the mechanical support structures inside the X-ray cabinet.

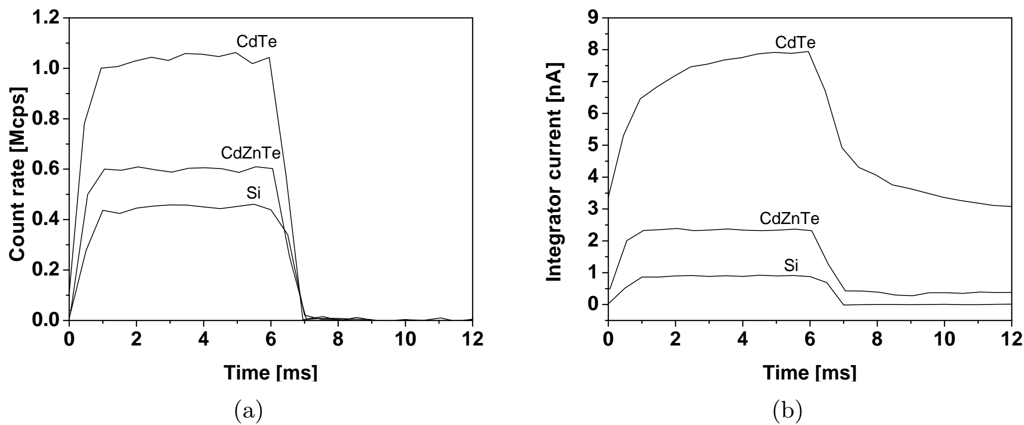

Fig. 6.14: Average photon count rates (a) and integrator currents (b) in 1 mm thick CdTe (CdTe11), 3 mm thick CdZnTe (CZT04) and 300 μm thick Si (Si03) samples as a function of the time. The quickly varying beam intensity is generated by a beam chopper operating at 80 Hz. Tube settings: 90 kVp and 50 μA at 6.5 cm focal spot to detector distance.

The integrator signals in Si again show the expected flat response, i.e. a stable current under irradiation and zero current when the X-ray beam is cut off (see Fig. 6.14(b)). The general shape of the CdZnTe signals also comes close to this ideal response with only a small residual current being visible outside the irradiation phase. As the brass disc absorbs 98 % of the X-ray photons, the observed current is likely an afterglow signal. This behavior is even more pronounced in the CdTe samples. Here, the current amplitude changes strongly under irradiation (approximately 30 % over 6 ms). Outside the irradiation interval, the CdTe signals show a significant residual current. It can thus be argued that the intensity variations happen too quickly for the detector to reach an equilibrium. The amount of trapped space charge oscillates and the signal current settles around an intermediate level.
The increasing current amplitude of the CdTe signals found in Fig. 6.14(b) can also be observed in the first part of the long-term measurements in Fig. 6.8. Here, the current increases initially and only after a few seconds the slope changes sign and the signal amplitudes start to fall.

6.2.3 Concluding remarks on the temporal response

Both the long-term and the short-term measurements showed that CdTe as well as CdZnTe exhibit temporal variations in the output signals due to the build-up of space charge. The lack of similar effects therefore makes Si a good choice for an X-ray sensor material if a high photon absorption is not mandatory. Yet, for applications that require a high stopping power of the sensor material, the investigated CdZnTe sensors offer the best balance between X-ray detection efficiency and temporal stability of the detector signals. A potential solution to the temporal behavior might lie in a mathematical correction of the amplitude changes. This approach is in principle feasible in case of a static irradiation of the detector. However, when scanning a larger object for several minutes with CIX 0.2, the photon flux changes constantly due to the imaged object. A correction of the intrinsically flux-dependent long-term changes is therefore very challenging. So, the only resort is to keep the sensor bias low in order to minimize the fluctuations.
A different situation arises in a CT-like environment in which the scans take just a few seconds and not minutes. The quickly rotating gantry can produce rapidly changing beam intensities, which makes these conditions comparable to the short-term measurements in section 6.2.2. Within the measurement precision achieved in this work an offline correction of the temporal changes in CdZnTe does not seem to be mandatory due to the small temporal variations in the signal amplitudes.

6.3 Module homogeneity and lateral polarization

In light of the better performance of the CdZnTe sensors compared to the CdTe crystals, the CdZnTe modules were further analyzed with respect to the homogeneity of the pixel response. As an example, Figs. 6.15(a) to 6.15(d) show the typical spread of the counter and the integrator signals in a CdZnTe module under homogeneous irradiation at 90 kVp, 20 μA and 4.5 cm focal spot to detector distance. The following analysis will address the magnitude and the origin of these large inhomogeneities.

6.3.1 Potential chip-based inhomogeneities

The detailed calibrations and tests presented in chapter 4 can be used to answer the question if the observed inhomogeneities in the system response are originating in the CIX 0.2

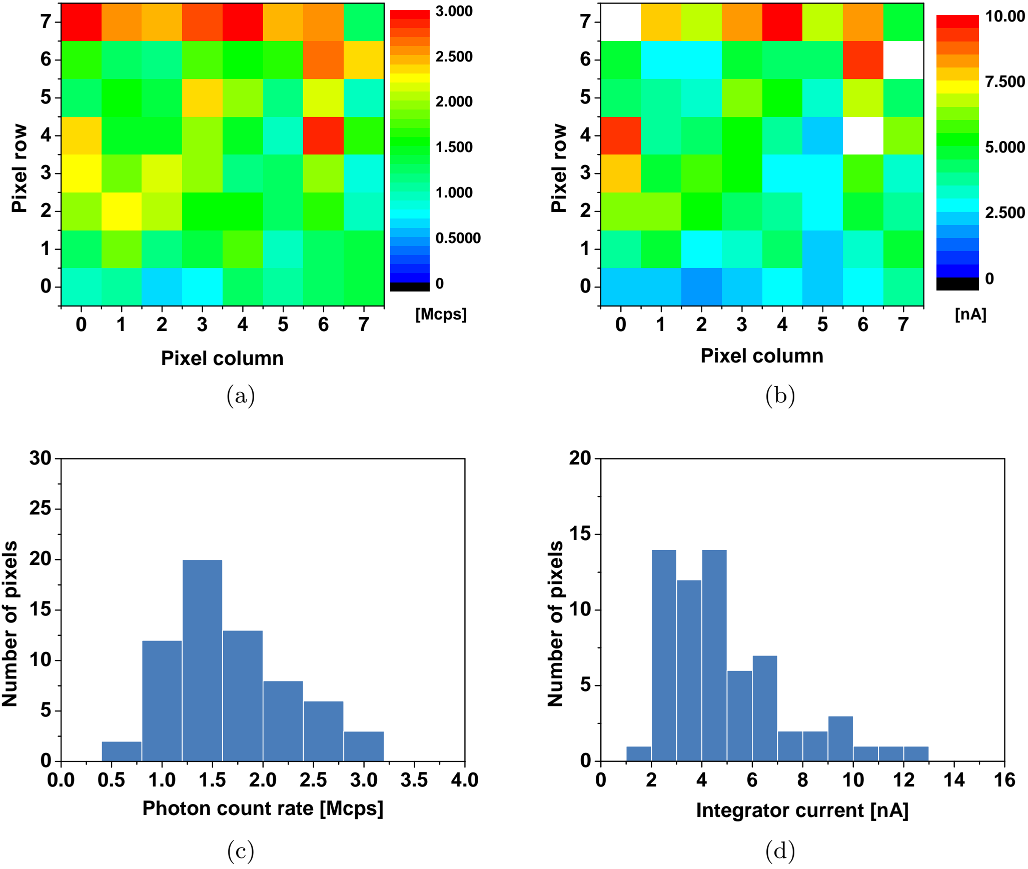

Fig. 6.15: Photon count rate in Mcps (a, c) and integrator currents in nA (b, d) in a CdZnTe (CZT03) module under homogeneous irradiation at 90 kVp, 20 μA and 4.5 cm focal spot to detector distance. The threshold was set to 24 keV. The relative standard deviation with respect to the mean is approximately 40 % in both channels.

chip. Considering the photon counting channel, only two chip-based effects are possible causes for the variations. The first candidate is a variation in the feedback current sources. The resulting differences in the pulse height (ballistic deficit) and the pulse duration at the preamplifier outputs would translate into different count rates at identical photon fluxes. Alternatively, different mismatch currents in the feedback circuits could also influence the homogeneity of the module through different baseline shifts in the pixels.
However, Fig. 6.16(a) shows that the inhomogeneities are not caused by variations in the feedback as they do not correlate with the count rate at a given photon flux. Similarly, no correlation between the mismatch current and the photon rate is observed (see Fig. 6.16(b)).
Regarding the integrator, possible explanations for the large spread between individual pixels are differences in the integrator pump sizes or alternatively differences introduced by the replication of the input current in the feedback circuit. The first potential cause can be excluded as the pump logic of every pixel is calibrated individually at the onset of every measurement. With regard to the second hypothesis, the feedback inhomogeneity was evaluated with the $ILeakSim$ constant current source. In all 64 pixels the $ILeakSim$ DAC was swept through its dynamic range and the relative spread of the pixel current at each DAC setting with respect to the module-wide average was calculated. Fig. 4.11

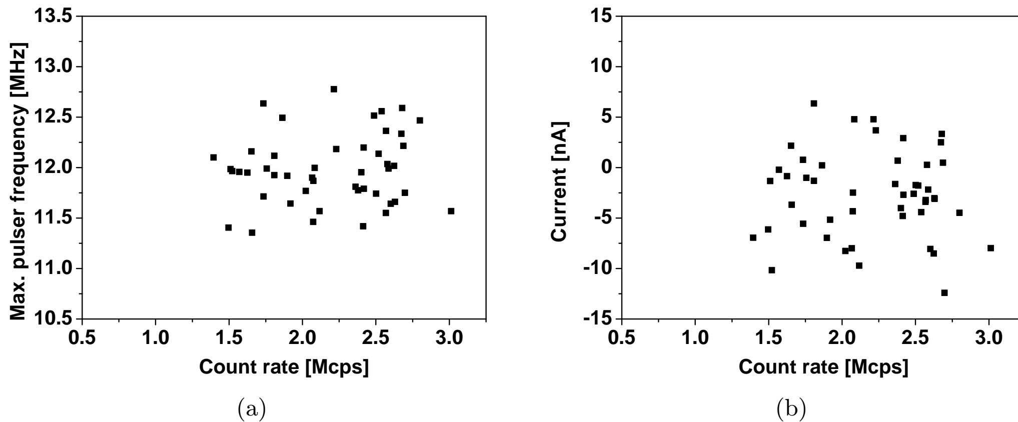

(a) (b)

Fig. 6.16: Correlation plots of potential chip-based origins of the inhomogeneities in the photon counting channel. (a): Influence of the counter performance as determined with electrical tests of the maximum count rate. (b): Impact of the feedback mismatch currents on the homogeneity. The X-ray measurements were performed at 90 kVp, 50 μA and 6.5 cm focal spot to detector distance. Both plots show no correlations and therefore any chip-based disturbances can be discarded.

showed a similar measurement in which the $ILeakSim$ current was measured directly with the integrator bypassing the differential feedback. It yielded a relative standard deviation of only a few percent. If the $ILeakSim$ current is routed through the preamplifier feedback a relative spread between the integrator currents of 6 % is obtained. This accounts only for a fraction of the relative standard deviation of 49 % observed in Fig. 6.15(b). Thus the measurements imply that the ASIC is not responsible for the observed inhomogeneities.

6.3.2 Sensor-based inhomogeneities

With the ASIC ruled out, the sensor is the only remaining source of the large inhomogeneities. In the following paragraphs it will be shown that apart from the temporal component, the tested samples also exhibit a form of spatial polarization.

Homogeneous irradiation

The spatial effect becomes evident when comparing the measured photon rate and integrator current for different tube settings. Fig. 6.17(a) shows the photon rate in all 64 pixels of a CdZnTe module as a function of the applied tube current. It can be seen that although the beam of the micro-focus X-ray tube is homogeneous over the detector area, the relative standard deviation of the count rates with respect to the mean rate is approximately 40 % (up to tube currents of approximately 30 μA). Analogously, Fig. 6.17(b) shows the different integrator currents as a function of the applied tube current.
At this point, the simultaneous counting and integrating concept offers a unique way of analyzing the origin of the inhomogeneities by plotting the measured rate in the pixels versus the corresponding integrator current. Fig. 6.18 illustrates that, if the correlation of integrator current and count rate is used to correct the photon rates, the relative standard deviation between the pixels is reduced to an average value of only 6 %. Hence, regardless of the very large differences in the count rates and the integrator currents under homogeneous irradiation, the pixels all measure very similar count rates at any given integrator current. This is a clear indication that different pixels collect different amounts of charge,

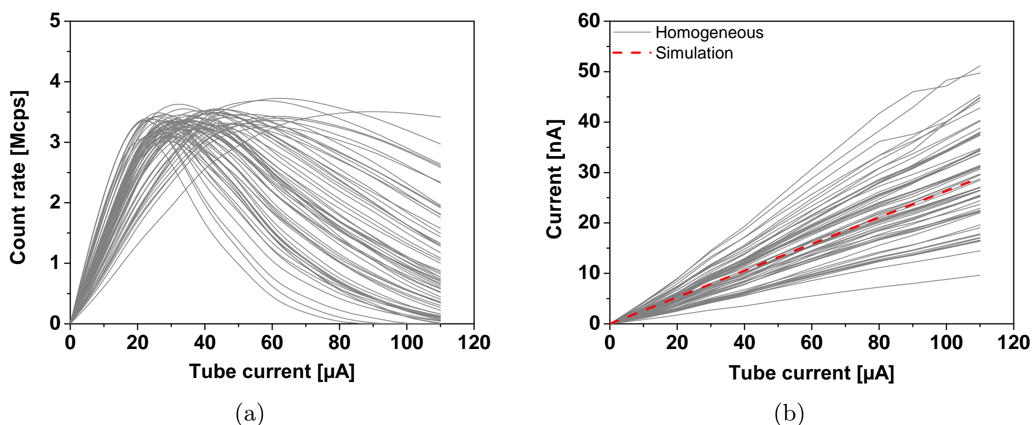

Fig. 6.17: Photon count rate (a) and integrator (b) inhomogeneity in a 3 mm thick CdZnTe module (CZT04) under homogeneous X-ray irradiation. The X-ray tube settings were 90 kVp and 4.5 cm focal spot to detector distance.

although the same amount of charge is deposited inside the pixel area. Note that the remaining spread in Fig. 6.18 can be attributed to variations in the counter electronics, specifically in the feedback current sources of the first differential pair.
The previous observations lead to the question as to where the inhomogeneities originate from. In principle, two potential effects have to be considered. Either the effective area of the pixels changes under irradiation, i.e. the area of one pixel increases at the cost of the effective area of a neighboring pixel. Alternatively, the pixel areas could be reduced by dead zones where no or only a significantly reduced charge collection takes place. In contrast to the effective area hypothesis, this second effect would always result in a reduction of the sensitive pixel area.

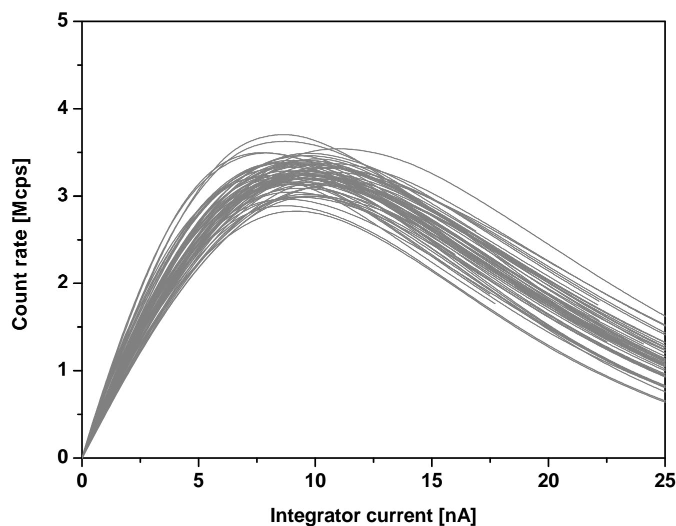

Fig. 6.18: Calibration of the photon count rate with the simultaneously measured integrator current (data taken from Figs. 6.17(a) and 6.17(b)). The individual rescaling of the photon count rate for all 64 pixels in the 3 mm thick CdZnTe sample (CZT04) strongly reduces the spread compared to Fig. 6.17(a). This illustrates the existence of a strong correlation between e.g. a small integrator current and an equally small photon count rate.

Simulation

The origin of the aforementioned inhomogeneities was identified with a full simulation of the sensor signals as a function of the tube current. This Monte Carlo simulation of the detector response was performed by [56] and it includes the following effects:

- Small pixel effect based on the precise sensor geometry
- Charge charing due to diffusion of the charge carrier cloud
- X-ray fluorescence from Cd and Te atoms
- Compton scattering
- Charge trapping with a mean free electron path of 0.09 m.

Further information on the underlying model and the accompanying equations can be found in [4, 57].
By comparing the measured integrator current to the simulation data (see Fig. 6.17(b)), it is found that about half the pixels show currents above the simulation result. Hence, charge loss due to dead areas within the pixels can be ruled out because this would only yield signal currents smaller than the simulation results. Thus, even though count rate and integrator current under homogeneous irradiation vary greatly between individual pixels, the charges are not lost, but seem to be drifting from one pixel to another. This result indicates that the pixels develop non-equal effective areas under irradiation. It is furthermore in accordance with the analysis presented in [45] and following their argument, the likely explanation of this phenomenon is an inhomogeneous build-up of space charge inside the detector. Fig. 6.19 sketches the basic mechanism responsible for the formation of effective pixel areas. It is based on the assumption that the inhomogeneous distribution of trapping centers inside the sensor material translates into inhomogeneously distributed space charges. As shown, these charges introduce a lateral electric field component and thereby influence the charge carrier movement.

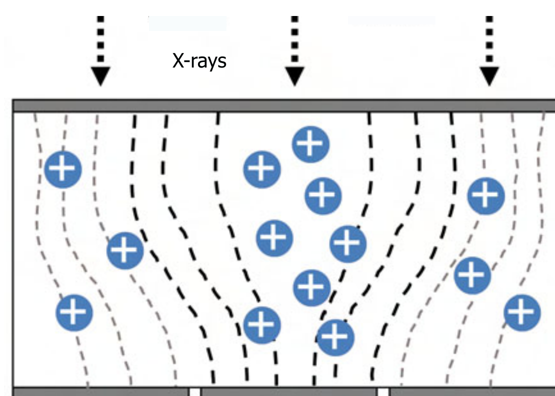

Fig. 6.19: Sketch of the electric field lines inside a CdZnTe pixel sensor induced by the inhomogeneous distribution of space-charges. As shown the increased space charge density above the central pixel causes a horizontal field component, which steers charges towards the central electrode. Thus the effective size of this pixel is larger than the dimensions given by the pixel electrode.

Pinhole measurements

Apart from the comparison with the simulation, the effective pixel size hypothesis is also supported by measurements on single pixels. These measurements used a 200 μm wide pinhole drilled into a 1 mm thick lead absorber to focus the X-ray beam onto one single pixel at a time. The pinhole was placed as close as possible to the detector module in order to minimize the geometric broadening of the irradiated area due to the cone-shape of the applied X-ray beam. Effectively, the irradiated area had a diameter of 250 μm, which amounts to 41 % of the pixel area.
The curves in Fig. 6.20(a) illustrate that the use of a pinhole again reduces the interpixel dispersion, i.e. when irradiated individually the pixels all register very similar count rates. Fig. 6.20(b) proves that the same is true for the integrator. This shows that the inhomogeneities are only present when the whole detector is irradiated. When using the 200 μm pinhole the space-charges are only created underneath the irradiated pixel. As the dimensions of the aperture are smaller than the pixel size, the effective pixel area is limited to the exposed area, which practically eliminates the variations between the pixels. However, if dead areas within the pixels were the origin of the inhomogeneities, their effect should also be visible in the single pixel measurements. This is because in that case a part of the pixel would simply loose its ability to collect charges regardless of the surrounding pixels. Hence, the pinhole measurements are also in agreement with the hypothesis that unequally distributed space charges are the origin of the observed inhomogeneities.
Fig. 6.21 shows what happens if the photon count rates under single pixel irradiation are normalized with the integrator current. The result is very similar to the result of the normalization of the counter values under homogenous irradiation (see Fig. 6.18). This proves that in general small count rates are highly correlated with small integrator currents. Note that the maximum count rate of the module decreases with the use of a pinhole compared to the homogeneous irradiation (see also Fig. 6.20(a)). This effect can be attributed to the change in the registered X-ray spectrum. In a pixel detector interpixel coupling effects like X-ray fluorescence and charge sharing introduce many low energy hits in the measured spectrum. As a consequence, the average energy of the detected photons

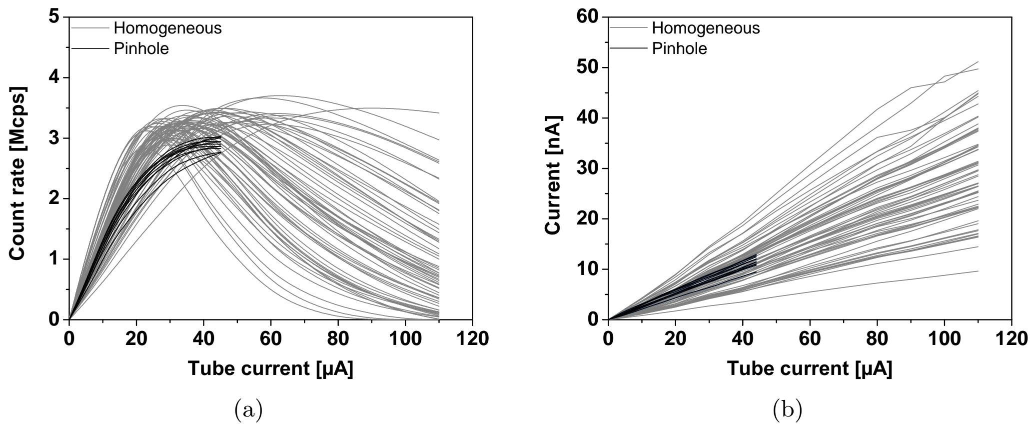

(a) (b)

Fig. 6.20: Comparison of photon count rate (a) and integrator current (b) inhomogeneity under homogeneous (gray) and one pixel only irradiation (black). The single pixel irradiation was performed on a subset of 11 CIX pixels of the 3 mm thick CdZnTe sample (CZT04). These pixels were selected individually with a 200 μm wide pinhole. The tube currents of the pinhole measurements are corrected for the reduction in the irradiated area (41 %).

under homogeneous irradiation is reduced compared to the average energy of the photons in the impinging spectrum. In the CSA the measured signals therefore have on average a reduced pulse height. This then means that at fixed feedback and threshold settings, the time over threshold of the preamplifier signals is decreased and the system can achieve higher count rates. For single pixel irradiation the average pulse size is larger due to the lack of low energy entries introduced by coupling events from the neighboring pixels. Thus, the system runs into pile-up at a lower count rate.

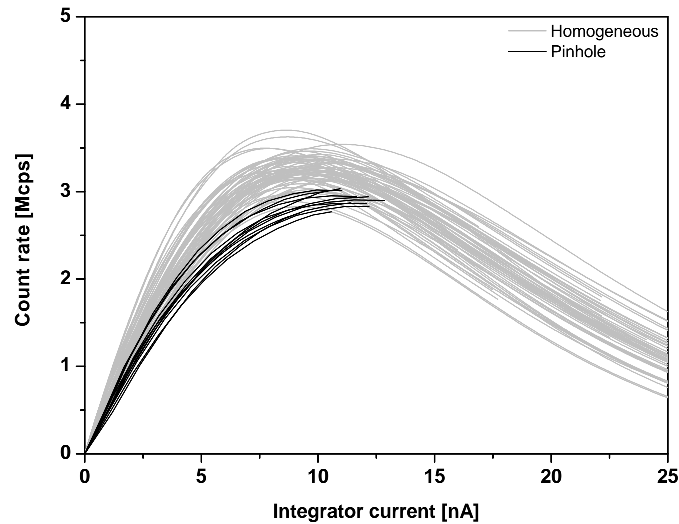

Fig. 6.21: Comparison of photon count rates plotted as a function of the integrator current under homogeneous (gray) and one pixel only irradiation (black) in a 3 mm thick CdZnTe detector (CZT04). The reduced count rate at any given integrator current in case of the single pixel irradiation is a result of the different absorption spectra.

6.4 Spectroscopic performance

The final material related aspect addressed in this work is the spectroscopic performance of the CIX detector. This analysis is of great importance for any measurement of the maximum count rate as well as the average photon energy reconstruction because it reflects the sensor's influence on the recorded X-ray spectrum.

6.4.1 ^{241}Am spectra

With its two major X-ray lines at 13.9 keV and at 59.45 keV, a radioactive ^{241}Am source is a convenient tool to assess the potential spectral degradation caused by the sensor. Fig. 6.22 shows an ^{241}Am spectrum measured with a CdTe module at 250 V bias. The data were obtained by routing the preamplifier output pulses of a single pixel to an external pad and by using a multi-channel analyzer (Tektronix TDS5140B oscilloscope with advanced trigger logic) to record the amplitudes of the individual X-ray signals. The relation between input charge and output voltage at the external pad buffer was calibrated with the help of the capacitive choppers. In order to suppress noise hits in the spectrum the lower threshold of the multi-channel analyzer was set to 10 keV.

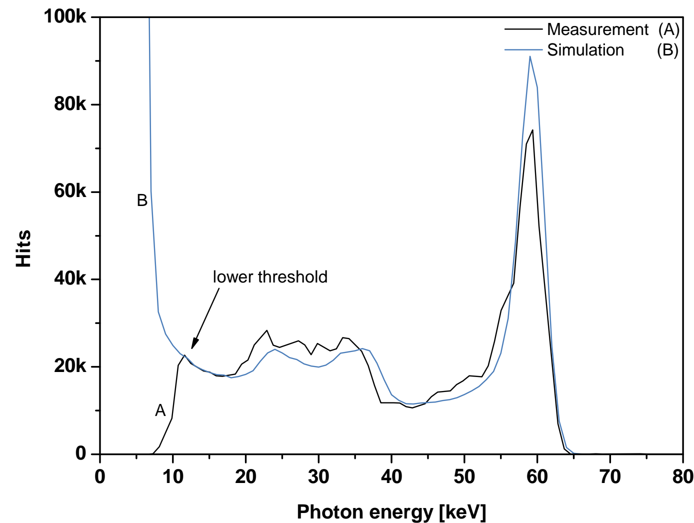

Fig. 6.22: Measured (A) and simulated (B; full detector response) X-ray spectra of an ^{241}Am source. The spectrum was recorded with the analog output of a single pixel in a CdTe module (CdTe11) at 250 V. Both curves illustrate the importance of sensor effects like Compton scattering and X-ray fluorescence on the spectral performance.

Measurement

The resulting spectrum nicely shows the 59.45 keV peak of the ^{241}Am source. The 13.9 keV line lies too close to the threshold of the multi-channel analyzed and is therefore suppressed. Apart from this, the spectrum contains a significant number of low energy hits in the range of 10 keV to 60 keV. These entries are introduced by the Compton effect and by X-ray fluorescence, which were both elaborated in section 2.6.
At roughly 60 keV photon energy, the Compton edge is situated at 12 keV. However, the relatively high threshold setting almost completely blocks the Compton background. Nevertheless, evidence of the Compton component can be found in the tailing section of the 60 keV peak. This tail extends to approximately 48 keV, which is the minimum energy of Compton scattered photons from neighboring pixels.
The bump in the spectrum between 23 keV and 37 keV is a caused by X-ray fluorescence from the Cd and Te atoms. The bumps lower half consists of 23 keV and 27 keV fluorescence photons, which enter from a neighboring pixel. Accordingly, the second half up to 37 keV is caused by fluorescence photons, which escape from the pixel under test. In that case the pixel only registers part of the 59.45 keV, i.e. 33 keV or 37 keV. So, the origin of the additional entries in the otherwise basically monoenergetic ^{241}Am spectrum can be fully understood in terms of Compton scattering and X-ray fluorescence.

Simulation

With the potential effects qualified, the simulation mentioned in section 6.3.2 was used to determine the detector response to the 60 keV photon line of the ^{241}Am source. In the simulation the electronic noise was set to 2.2 keV and the detector temperature was assumed to be 40°C.
Fig. 6.22 shows that the simulated spectrum mirrors the measured data, proving the accuracy of the simulation and the correct interpretation of the spectrum. At energies below 10 keV the simulated spectrum is dominated by charge sharing events between

individual pixels. These hits are not present in the measured spectrum as it is cut-off by the 10 keV threshold of the multi-channel analyzer.

6.4.2 Charge collection efficiency

The well known energy of the ^{241}Am photo-peak furthermore allows to determine the *charge collection efficiency* (CCE) of the detector modules. This quantity is obtained by measuring the position of the photo-peak for various bias settings. In order to calculate the CCE simultaneously for all 64 pixels the spectra were measured by the method detailed in section 4.2.2, i.e. by sweeping the discriminator threshold and differentiating the resulting integral spectra. The problem of this analysis is that at lower bias settings the magnitude of the charge loss due to charge carrier trapping is unknown. Therefore the measured peak positions (in mV) were plotted as a function of the bias voltage. The peak position in case of 100 % charge collection (V_{Peak}^{100}) was extrapolated using the following formula:

$$V_{Peak}^{100} = V_{Peak}(V_{Bias}) + const_1 \cdot exp\left(\frac{-V_{Bias}}{const_2}\right) \tag{6.12}$$

Setting this V_{Peak}^{100} in relation to the measured peak position V_{Peak} at a given bias finally yields the CCEs, which are shown in Fig. 6.23. It is found that at maximum bias the CCEs are at 99 % for CdTe and 97 % for CdZnTe. The CdZnTe sample number 3 yields a slightly lower CCE of 95 % at maximum bias.

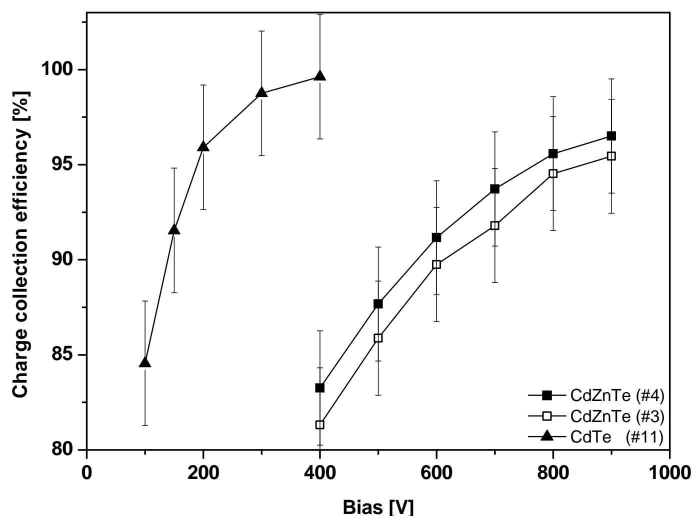

Fig. 6.23: Average charge collection efficiencies for a 1 mm thick CdTe (CdTe11) and two 3 mm thick CdZnTe (CZT03, CZT04) samples as a function of the detector bias.

6.4.3 Tube spectra

Under regular imaging conditions the photons are generated by an X-ray tube and not by a quasi-monoenergetic source. Thus, it is expected that the individual spectral components are blurred due to the described non-idealities and that the shape of the whole spectrum is altered. Fig. 6.24 shows the absorbed X-ray spectrum measured with a 3 mm thick CdZnTe detector under homogeneous irradiation from a X-ray tube operated at 90 kV. The impinging X-rays were filtered by 1 mm of aluminum in order to eliminate the lowest

energy photons (<10 keV). The measurement is again based on a differentiation of an integral spectrum. In addition to the measurement data, Fig. 6.24 includes a simulation of the tube spectrum (see dashed line) based on the parameters of the Hamamatsu X-ray tube [58]. Note that the simulation displays the characteristic lines of the tube's W anode. It furthermore illustrates the influence of the 1 mm Al filter as the simulated spectrum does not contain any photons below 12 keV. If this spectrum is compared to the measured spectrum, the low energy section of the absorbed spectrum immediately stands out. These low energy hits can again be explained by interpixel coupling effects like Compton scattering and X-ray fluorescence. This explanation is supported by the good agreement between the full simulation of the detector response and the measurement data. The high accuracy of the simulation is also reflected in the fact that it does not only reproduce the shape of the spectrum qualitatively but it also achieves a very good quantitative representation. Only below 20 keV does the simulation deviate from the measurement. The origin of this discrepancy is not fully understood but the likely cause is an underestimation of the low energy charge sharing component. In addition, cross-talk in the photon counters of individual pixels could also potentially increase the count rate in the low energy regime. Nevertheless, these results further underline the large importance of interpixel coupling effects when irradiating a detector homogeneously. For CIX 0.2 the low energy shift of the absorbed spectra implies that the average photon energy is reduced. As a consequence the contrast in the average photon energy image is decreased accordingly.
The large impact of the aforementioned interpixel coupling effects can also be illustrated if only a single pixel is irradiated. The dash-dotted line in Fig. 6.24 shows one such measurement in which the X-ray beam was directed onto a single pixel with the help of a 200 μm pinhole. In order to understand this spectrum two factors have to be considered. First, the pinhole prevents low energy photons scattered from neighboring pixels from entering the pixel under test. Secondly, the pinhole also greatly reduces the probability

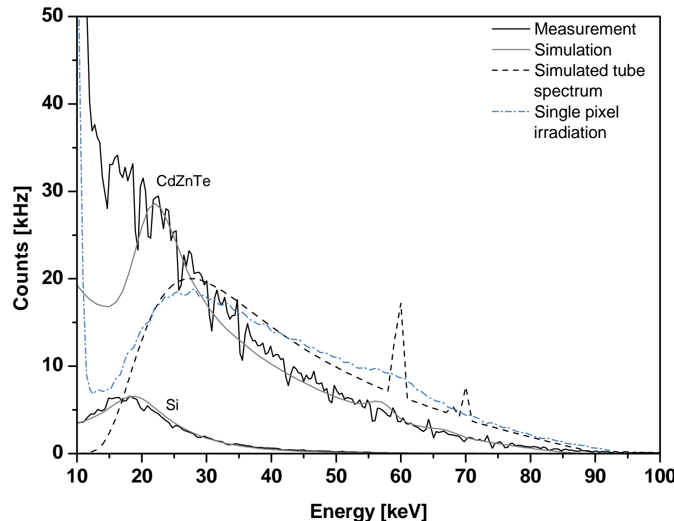

Fig. 6.24: Measured (solid black) and simulated (solid gray) X-ray absorption spectra for CdZnTe (CZT04) and Si (Si03) detectors. The impinging tube emission spectrum (90 kVp) is given by the dashed line. The dash-dotted line was measured by only irradiating a single pixel with the help of a 200 μm wide pinhole (reduced irradiated area is accounted for). The tube current was set to 100 μA and the focal spot to detector distances were 18.5 cm and 4.5 cm during the CdZnTe and Si measurements, respectively.

that a fluorescence or Compton scattered photon leaves the pixel. This is because the circular aperture was centered on the pixel such that most photons have to travel a significant distance before leaving the irradiated pixel. So, in most cases the stray photons are reabsorbed in the initial pixel and the spectrum still largely resembles the incident tube spectrum (the typical absorption length of 30 keV photons in CdZnTe is 90 μm). In Fig. 6.24 even the smeared-out remainders of the characteristic X-ray lines are visible.
Apart from the CdZnTe data, Fig. 6.24 also contains the results of simulations and measurements performed with a 300 μm thick Si sensor. Si does not suffer from X-ray fluorescence at energies above 5 keV and the thinner sensors also reduce the impact of charge sharing. The absorbed spectrum confirms this fact by not featuring an increased low energy section to the left of the absolute maximum at approximately 20 keV. The very good agreement between simulation and measurement for Si furthermore discounts low energy scatter radiation from the surrounding material as a potential origin of the increased low energy count rate in CdZnTe. The mechanical support structures inside the X-ray cabinet were not changed between the Si and CdZnTe measurements and thus potential scatter radiation should also have influenced the Si data.
Finally, Fig. 6.25 shows a comparison of two tube spectra, which were recorded with a CdZnTe and a CdTe sensor. It is found that the spectra are largely identical. Particularly, they both show a very large number of low energy (<10 keV) charge sharing events. This indicates that at similar electrical field strengths (900 V / 3 mm and 400 V / 1 mm) charge sharing is not significantly different for the two sensor geometries.
Tab. 6.3 gives a summary of the measured and simulated average photon energies, which can be used for a quantitative analysis of the interpixel coupling effects. In this calculation photon entries below 10 keV were neglected as all detectors show a significant noise contribution below this value. Both the CdTe and the CdZnTe sensors register an average photon energy of approximately 28 keV under homogeneous irradiation. If compared to the average energy of the impinging X-ray spectrum (39.6 keV), this constitutes a reduction of 30 % with respect to the original value. The simulation of the detector response yields 30.9 keV average photon energy, which lies above the measurement result because

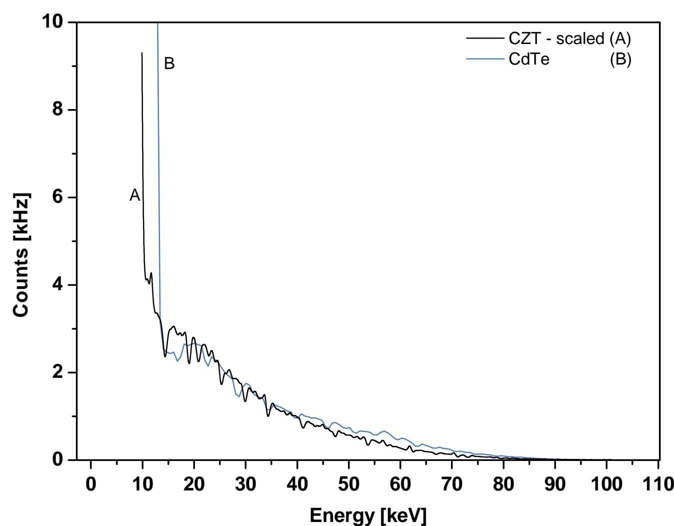

Fig. 6.25: X-ray absorption tube spectra measured with the CZT04 (A) and the CdTe11 (B) module. The CdTe measurement was performed at 20 μA and 28.5 cm focal spot to detector distance.

of the underestimated low energy contribution. In case of the pinhole measurement the resulting 38.2 keV come very close to the 39.6 keV of the incident spectrum. This again underlines that the shift in the spectrum is caused by the photons from neighboring pixels. Si also shows a very good agreement between simulation and measurement. Nevertheless, in this case it is expected that the measured average photon energy deviates significantly from the average energy of the impinging tube spectrum because the absorption spectrum of Si suffers from the low X-ray absorption probability.

	CdZnTe (hom) [keV]	CdZnTe (pin) [keV]	Si [keV]
Sim	30.9	39.7	21.4
Meas	28.6	38.2	22.3

Tab. 6.3: Measured and simulated average photon energies in CZT04 and Si03. The abbreviations '*hom*' and '*pin*' refer to homogeneous and pinhole irradiation, respectively.

7. CIX module performance under X-ray irradiation

7.1 Dynamic range

This section assesses the performance of the CIX 0.2 counting and integrating channels considering all the information, which has been gained on the ASIC's electrical performance as well as the sensor effects. The measurements were performed under imaging conditions, i.e. the sensors were biased, the cabinet temperature was in thermal equilibrium, the DAC settings were optimized for the highest count rate, the integrator was connected to the sensor via the differential feedback and all signals were generated by the Hamamatsu microfocus X-ray tube at 90 kVp. The ASIC was operated at the standard settings used throughout this work:

- Frame duration: 3 ms
- Counter threshold: 10 keV
- I_{Fb} feedback current: 91 nA
- Leakage current compensation mode: None
- Integrator charge pump size: 20 fC
- $CKInt$ Integrator clock frequency: 10 MHz

Fig. 7.1 shows the dynamic range of the CIX 0.2 system at the aforementioned settings as obtained with the best performing detector module (CZT04 at 900 V). The X-ray intensity was varied by changing the tube current as well as the focal spot to detector distance between 4.5 cm and 18.5 cm. This way it is possible to cover almost five orders of magnitude in photon flux. In order to allow an easy comparison between the measurements at different distances, all tube currents are scaled to a distance of 1 m. The extrema of the photon counter's and integrator's dynamic range are given in Tab. 7.1.
For the photon counter, it is found that the number of detected photons ranges from 330 cps, i.e. a single photon per 3 ms frame, up to its maximum at (3.3 ± 0.1) Mcps. Hence, at standard settings the counter covers four orders of magnitude in photon flux. Concerning the integrator, the standard settings yield a minimum integrator current of 19 pA and a maximum current of 45 nA. This amounts to more than three orders of magnitude in dynamic range. Still, this upper limit is significantly lower than the 200 nA, which were measured in the electric tests of the ASIC in section 4.3.2. The crucial difference between these two measurements of the integrator's dynamic range is that the X-ray measurement was performed in the simultaneous counting and integrating mode whereas the electrical tests used a direct injection into the integrator. The simultaneous counting and integrating has consequences for the dynamic range as the design error, mentioned in section 3.3.6, prevents the use of a leakage compensation mode. Therefore all currents for the integrator have to be generated by the first differential pair. This circuit can at most deliver half of the I_{Fb} current into one branch of the differential pair. At an I_{Fb} current

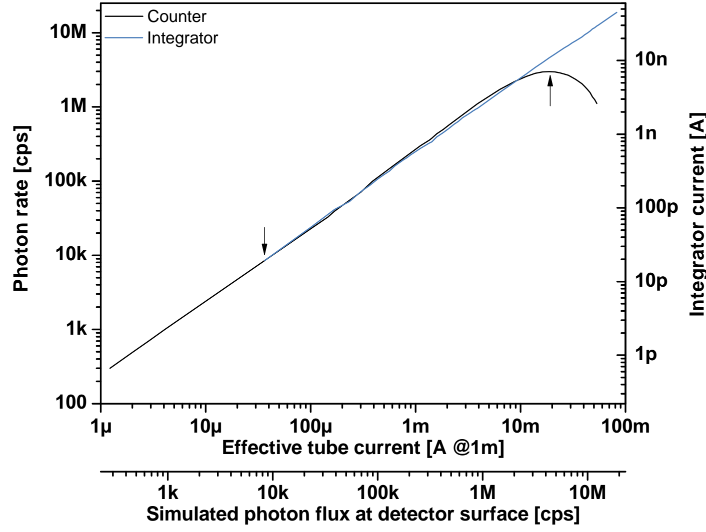

Fig. 7.1: Dynamic range of the CIX 0.2 detector under X-ray irradiation. The measurement was performed with a 3 mm thick CdZnTe sensor (CZT04) at 900 V bias, an X-ray endpoint energy of 90 keV and at varying tube currents and focal spot to detector distances. The chip was operated at standard settings, i.e. at 3 ms frame duration, 10 keV threshold, 20 fC integrator charge pump size and an integrator clock frequency of 10 MHz. The 60dB overlap region in tube currents between counter and integrator is indicated by the arrows in the figure. Note that the minimum focal spot to detector distance and the maximum tube current set an upper boundary for the largest integrator signals that can be achieved with the X-ray test setup.

of 91 nA this sets an upper limit to the integrator current of 45 nA, which nicely agrees with the observation. This maximum is reached at a normalized tube current of 82 mA at 1 m. Extrapolating this value to an integrator current of 200 nA then yields that, given a large enough feedback current, the integrator can in principle work up to a tube current of 360 mA. Photon fluxes of this intensity can not be generated by the X-ray tube in the experimental setup used in this work.
Summarizing the above, the combined dynamic range of the CIX 0.2 ASIC under X-ray irradiation and at standard chip settings covers approximately five orders of magnitude in photon flux or tube current. At the same time the overlap between counter and integrator spans three orders of magnitude.

	Counter		Integrator	
	[Mcps]	[Mcps/mm^2]	[nA/pixel]	[nA/mm^2]
Min	$300 \cdot 10^{-6}$	$2.4 \cdot 10^{-3}$	0.019	0.152
Tube [mA at 1 m]	0.001		0.036	
Max	3.3	26.4	45	360
Tube [mA at 1 m]	19		82.6	

Tab. 7.1: Table of the CIX 0.2 dynamic range measured with the best performing CdZnTe module (CZT04). Module settings are identical to the ones given in Fig. 7.1. Tube settings refer to the normalized tube currents at which the minimum and maximum values were measured.

7.1.1 Counter dynamic range

Fig. 7.1 showed the characteristic dynamic range of the CIX 0.2 system. In order to generalize this result, it has to be analyzed with respect to the theoretically expected maximum count rate, the impact of the detector bias on the maximum rate and potential limitations of the counter design.

Maximum count rate

The previous section stated that at 10 keV threshold and maximum feedback settings ($I_{Fb} = 91$ nA), the system's maximum count rate lies at 3.3 Mcps. This value was measured at a tube voltage of 90 keV, which, according to section 6.4.3, corresponds to an average measured photon energy of approximately 29 keV. A direct crosscheck of this result with the internal charge injection circuits of CIX 0.2 is not possible because the average pulse size of 29 keV lies below the minimum input charge of 1.1 fC (32 keV) that the test circuits can deliver (see section 4.2.1). Nevertheless, the expected maximum count rate at 29 keV pulse size can be extrapolated from the maximum count rate measurements presented in section 4.3.1. Fig. 4.8 showed the maximum count rate for different pulse sizes at two different threshold settings. Extrapolating the curve at 10 keV threshold setting to a pulse size of 29 keV gives a maximum pulser rate of (8.8 ± 0.2) MHz. However, as the time interval between individual photons in the X-ray beam is not constant but rather Poisson-distributed, the value of 8.8 MHz is too large. Section 3.3.1 stated that the count rate behavior of a paralyzable counter, if exposed to monoenergetic Poisson-distributed pulses, is given by (3.2). Replacing the incident photon spectrum by a Poisson-distributed series of monoenergetic photons at exactly the spectrum's average energy yields:

$$N_{Meas}^{Max} = (8.8 \pm 0.2)\ MHz \cdot e^{-1} = (3.24 \pm 0.08)\ Mcps \tag{7.1}$$

As the X-ray measurements yielded a maximum rate of (3.3 ± 0.13) Mcps, this shows that the electrical test and the X-ray measurements are in excellent agreement.

Bias-dependence

Besides the discriminator setting and the spectral distribution of the input pulses, the maximum count rate in a direct converting semiconductor sensor is also influenced by the applied bias. Hence, the maximum count rate of different CIX 0.2 modules equipped with CdTe and CdZnTe sensors was evaluated at various bias settings. Note that the very low X-ray absorption probability of Si does not allow a similar measurement for the Si module as the ASIC's maximum count rate can not be reached with the available X-ray tube. Therefore Fig. 7.2 only contains the results for the Cd-based sensor materials.
The measurements show that at low bias values the maximum count rate increases with the bias voltage in all sensor samples. This is a direct consequence of the higher electric field inside the sensor, which reduces the transit time of the generated charge carriers and therefore the pulse width and the comparator dead time. In the case of the 1 mm thick CdTe sample, the maximum count rates are comparable to those of CZT04. However, unlike CdZnTe the optimum bias value is not equal to the highest safely achievable voltage across the detector. Instead, a bias of 300 V offers the highest count rate capability. The reason for this is the photon flux-dependent current, which manifests itself in the CdTe samples and causes a baseline shift at the preamplifier output (see sections 6.1.3).
In addition, Fig. 7.2 also illustrates that the performance among the CdZnTe samples varies greatly. The previous section showed that the maximum count rate of the CZT04

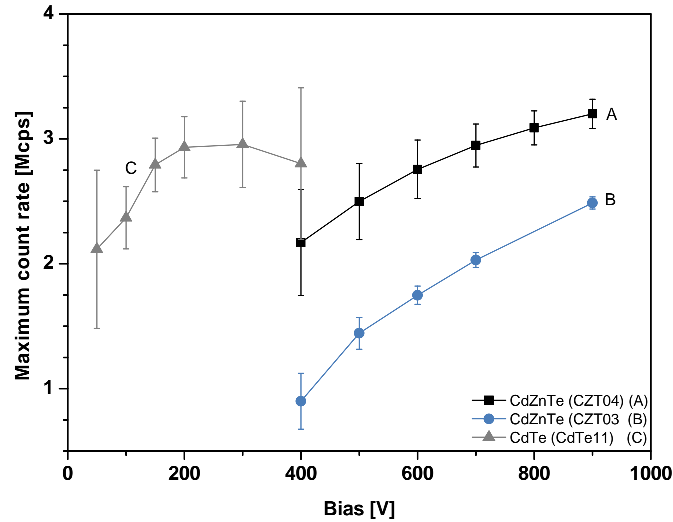

Fig. 7.2: Average maximum count rate per detector module for 1 mm CdTe (CdTe11) and 3 mm CdZnTe samples (CZT03, CZT04) as a function of the detector bias. The error bars indicate the module-wide spread. The measurements were performed at standard chip settings with a 90 kVp tube spectrum.

sample agrees very well with the value obtained in electrical tests of the chip performance. In contrast to this, the second CdZnTe sample shown in Fig. 7.2 has much lower maximum count rates.
Here, the simultaneous counting and integrating concept can again offer some valuable insights into the origin of the observed effects. Figs. 7.3(a) - 7.5(b) show different views of the simultaneously measured counter and integrator data. Considering first the integrator current as a function of the tube current (see Figs. 7.3(a) and 7.3(b)), it can be observed that the expected linear increase of the integrator data is only reproduced by CZT04 (right graph). In CZT03 (left graph) the curves all exhibit a kink in the slope, i.e. above a certain tube current the slope of the measured currents changes abruptly. The

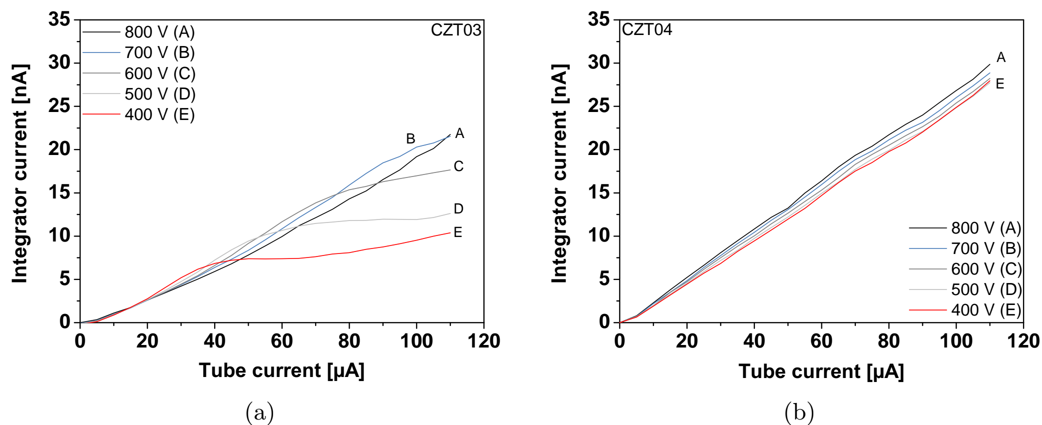

Fig. 7.3: Integrator current versus tube current in two CdZnTe modules at standard chip settings. (a): CZT03; (b): CZT04. The tube voltage was in both cases 90 kV and the focal spot to detector distances were 6.5 cm and 4.5 cm for CZT03 and CZT04, respectively. Note that sample CZT03 reacts much stronger to changes in the detector bias.

point at which this happens depends on the bias voltage.
Furthermore, the measurement on CZT04 shows that at 110 μA tube current the integrator current rises by approximately 10 % if the bias is doubled. This current increase agrees nicely with the 12 % increase in the charge collection efficiency (CCE) between 400 V and 800 V reported in section 6.4.2. This section also showed that the CCEs of the two CdZnTe samples are virtually identical at the low photon fluxes generated by the ^{241}Am source. At large photon fluxes (110 μA tube current) the measured current in CZT03 more than doubles between 400 V and 800 V bias. Hence, a first conclusion of this analysis is that, depending on the sensor sample, the photon flux can influence the sensor's CCE.
Moving on to the counter results in Figs. 7.4(a) and 7.4(b), it is found that the behavior of the two samples is again very different. While the maximum count rate in CZT04 is always registered at roughly the same tube current, the maximum rates in CZT03 occur at very different tube currents depending on the applied bias. In general, a larger bias has two opposing effects on the maximum count rate. On the one hand it increases the CCE thereby reducing the maximum count rate but on the other hand it also shortens the pulse duration and thus allows higher count rates. The constant tube current at which the count rate maxima in Fig. 7.4(b) occur then implies that the two opposing effects compensate each other in CZT04. Moreover, the different behavior of CZT03 indicates that the charge carrier transit in the samples is likely to be different.
This difference becomes even more evident if the counter results are plotted as a function of the integrator current (compare Figs. 7.5(a) and 7.5(b)). The resulting maximum count rates and the integrator currents at those maximum rates are also summarized in Tab. 7.2. Consider for example that the integrator current at which CZT03 reaches its maximum count rate at 400 V bias is 5.8 nA , while the same value for CZT04 lies at 10.7 nA. Doubling the bias to 800 V results in an integrator current at maximum count rate of 12.5 nA in CZT03. This amounts to a 215 % increase. Simultaneously the current at the maximum count rate increases by only 14 % in CZT04.
The different behavior of the two samples is consistent with a model, which assumes a flux-dependent polarization of the detectors. It has been reported [43] that CdZnTe shows a critical flux behavior, meaning that above a certain flux limit the accumulated trapped charges inside the crystal cancel the externally applied electric field and the maximum

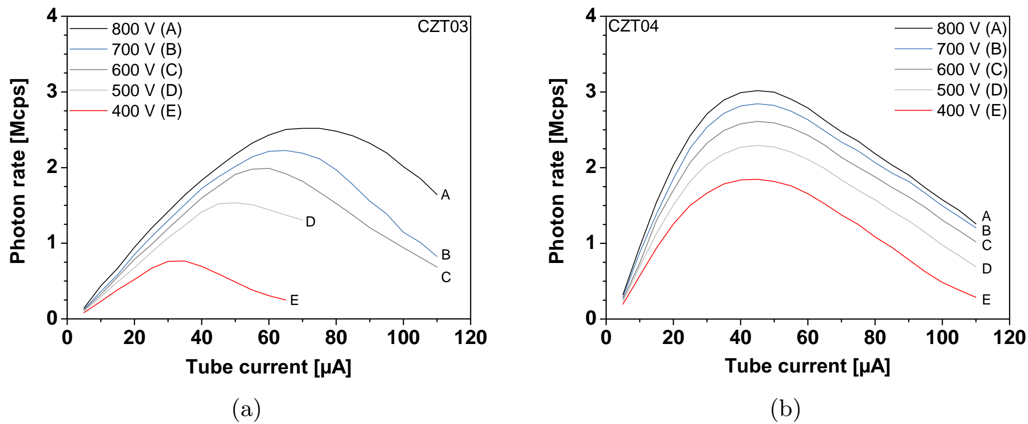

(a) (b)

Fig. 7.4: Photon count rate versus tube current in two CdZnTe modules at standard chip settings. (a): CZT03; (b): CZT04. The data were acquired simultaneously with the ones in Figs. 7.3(a) and 7.3(b).

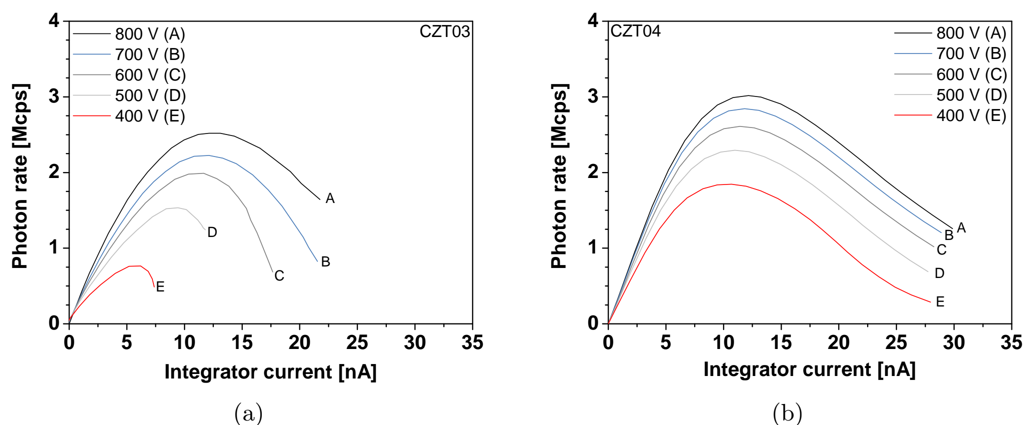

Fig. 7.5: Photon count rate versus integrator in two CdZnTe modules. (a): CZT03; (b): CZT04.

count rate is reduced, i.e. the sample polarizes. The absolute value of this critical photon flux is mainly determined by the hole mobility of the sample because CdZnTe with lower $\mu\tau$-products accumulates larger space-charges and therefore polarizes at lower fluxes. This critical flux behavior can be seen in both the counter and the integrator data obtained with CZT03. Apart from variations between individual samples according to their $\mu\tau$-products, the critical photon flux also depends on the applied bias. This is expected because the electric field inside the sensor, which has to be compensated by polarization, is directly influenced by the bias. While one sample (CZT04) shows an increase in integrator current, which can readily be explained by an increased CCE, the other sample (CZT03) heavily reacts to changes in the applied bias. This is a strong indication for a photon-induced breakdown of the internal electric field in CZT03. At the same time it is not possible to assess the critical photon flux behavior of the CZT04 sample because any potential flux limit lies outside the photon flux that can be generated by the X-ray tube.
These observations on the maximum count rate lead to the conclusion that high rate counting applications need as high a bias as possible in order to balance potential polarization effects in the sensors. This demand for a high bias is in direct conflict with the observations on the long-term stability of the sensor signals, which called for a reduced bias (see section 6.2.1).

	CZT03		CZT04	
Bias	Cntr. [Mcps]	Int. [nA]	Cntr. [Mcps]	Int. [nA]
400 V	0.8	5.8	1.8	10.7
500 V	1.5	9.3	2.3	11.0
600 V	2.0	11.2	2.6	11.4
700 V	2.2	12.0	2.8	11.8
800 V	2.5	12.5	3.0	12.2

Tab. 7.2: Maximum count rate as a function of the bias for two CdZnTe modules (CZT03, CZT04). The integrator currents refer to the values which are measured at the maximum photon count rate. In contrast to CZT04, CZT03 shows a strong bias-dependence of the integrator current at maximum count rate. The measurements were performed with a 90 kVp tube spectrum.

Stability

The particular design of the CIX 0.2 feedback circuit has some implications for the counter performance. One of these is that a large leakage current can decrease the maximum count rate since the current necessary to compensate the leakage component is not available for the discharge of the feedback capacitor C_{Fb}. Thus, the return to baseline at high leakage currents is prolonged.
This effect is illustrated in Fig. 7.6(a). The figure shows 1.6 fC pulses ($ICurrInj = 5$ at 15 ns; 46 keV CdZnTe equivalent), which were measured by connecting the peamplifier output of a pixel to the analog output buffer of the ASIC. In this measurement an additional leakage current was simulated with the on-chip $ILeakSim$ current source. All four pulses in Fig. 7.6(a) are offset corrected, with the exact offset voltages given in the legend. As expected, the preamplifier reacts to an increased constant current with a larger offset. Furthermore, it is evident that high additional currents (>15 nA) increase the pulse duration. This is illustrated in Tab. 7.3, which contains the pulse durations for a 10 keV threshold setting. Note that these time over thresholds are larger than the typical pulse durations stated in section 4.3.1. This is because of the low pass filtering of the preamplifier by the analog buffer.
The increase in the pulse duration is also visible in the maximum count rate shown in Fig. 7.6(b). Here, the average count rate of a CdZnTe module is shown as a function of the tube current. The data indicate that a higher constant input current reduces the maximum count rate as described above.

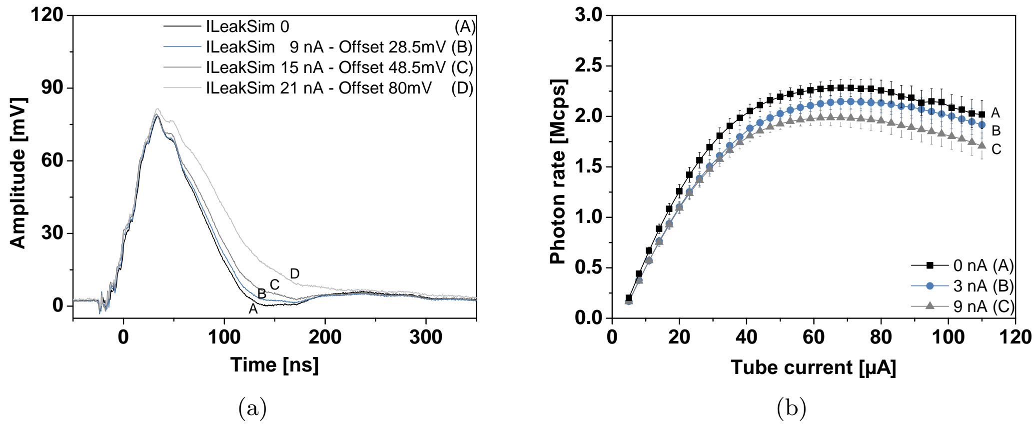

(a) (b)

Fig. 7.6: Changes in the photon counter performance due to constant currents. (a): Preamplifier output pulses measured with the analog output of the ASIC. Large $ILeakSim$ constant currents increase the pulse duration at the preamplifier output. (b): Average photon count rate as a function of the tube current for different additional $ILeakSim$ currents. Higher currents reduce the maximum count rate. The measurement was performed with a CdZnTe (CZT03) module at standard settings under irradiation at 90 kVp and at 6.5 cm focal spot to detector distance.

$ILeakSim$ current	0 nA	15 nA	21 nA
Time over threshold	104 ns	115 ns	144 ns

Tab. 7.3: Time over thresholds (Tot) for 1.6 fC pulses (46 keV CdZnTe equivalent) at a 10 keV threshold with different additional $ILeakSim$ constant currents. The Tot was measured directly at the preamplifier output with an analog output buffer. Note that the buffer's bandwidth imposes a low pass filtering on the signal.

However, with leakage currents on the order of 340 pA per pixel in CdZnTe, the impact of the leakage current on the maximum count rate is negligible. In case of CdTe, this effect gains importance because the average leakage currents are ten times larger than in CdZnTe.
Nevertheless, the count rate performance of the CdTe modules is dominated by a different effect. Fig. 7.7 shows this effect using the example of the count rate measured with a CdTe module under irradiation with the X-ray tube set to 90 kVp at a focal spot to detector distance of 6.5 cm. Some pixels feature the typical response of a paralyzable counter but a significant number of pixels deviates from this well understood behavior. In these pixels the count rate suddenly increases drastically and then exhibits a sharp breakdown. This is a direct result of a large shift of the preamplifier baseline. It has already been mentioned that this increase in the preamplifier output potential acts as an effective threshold lowering. In CdTe it can get so large that the discriminator is triggered frequently by the preamplifier noise, which causes the step-like increase in the count rate of some pixels. If the baseline shift gets too large and the preamplifier baseline is constantly above the discriminator threshold, the counter is paralyzed and the count rate drops to zero.
Starting from these observations, the baseline shift in CdTe and CdZnTe is quantified by measuring integral X-ray tube spectra under various levels of irradiation. Figs. 7.8(a) and 7.8(b) show the results for a CdTe (CdTe11) and a CdZnTe (CZT03) module. The preamplifier baseline can be identified easily by the single peak in the measurement without X-rays, i.e. at 0 μA tube current. As the tube current is increased, the count rates above this noise peak rise and the tube spectrum becomes visible. Ideally, the position of the noise peak should remain unchanged. However, this is not the case for the CdTe detector, where the system shows a significant baseline shift that moves the whole spectrum to higher energies (see Fig. 7.8(a)). Identical measurements on a CdZnTe module do not reveal an equally strong baseline shift. In fact, any potential baseline shift is so small that the high occupancy of the pixels obscures it. Furthermore, at low tube currents, where

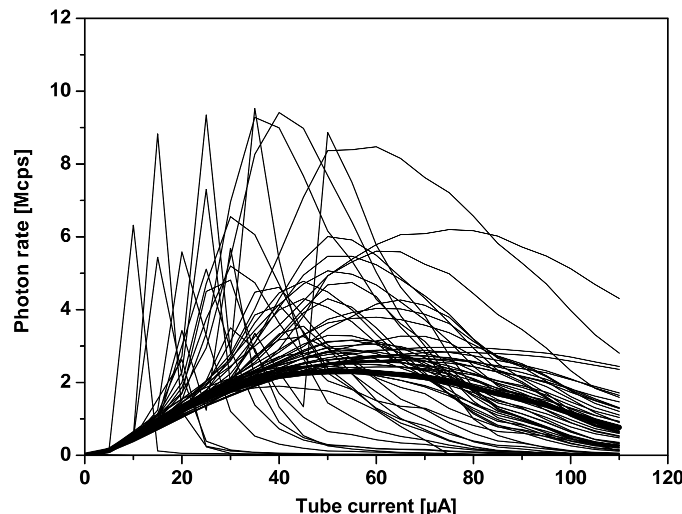

Fig. 7.7: Photon count rate as a function of the tube current in a CdTe (CdTe11) module at standard chip settings. In some pixels the high photon flux causes such a large baseline shift that the discriminator is triggered by noise events. This is the reason for the sharp spikes in the count rates. The measurement was performed at 90 kVp and at 6.5 cm focal spot to detector distance.

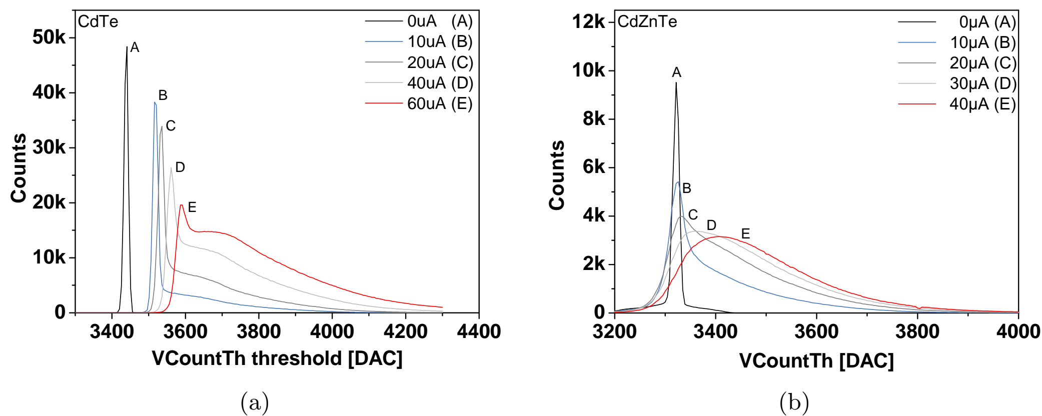

Fig. 7.8: CIX 0.2 preamplifier baseline shift under X-ray irradiation measured with (a) a CdTe (CdTe11) and (b) a CdZnTe (CZT03) module at standard settings. The figures display integral X-ray tube spectra. The noise peak on the left side of the CdTe spectra is shifted to higher $VCountTh$ values (energies) at higher X-ray fluxes. CdZnTe does not show a similar shift. The measurements were performed at 90 kVp and at 6.5 cm focal spot to detector distance.

the noise peak in CdZnTe can still be identified, its position remains virtually unchanged compared to the 0 μA measurement. This is a second confirmation that the baseline shift in CdZnTe can indeed be neglected. These aforementioned results are supported by cross-checks on two other CdTe and CdZnTe samples.

With the effects of the baseline shift characterized, the final aspect which remains is the origin of this shift in CdTe. Fig. 7.9 displays the baseline shift simultaneously to the global detector current under irradiation. As the baseline shift follows the change in the global

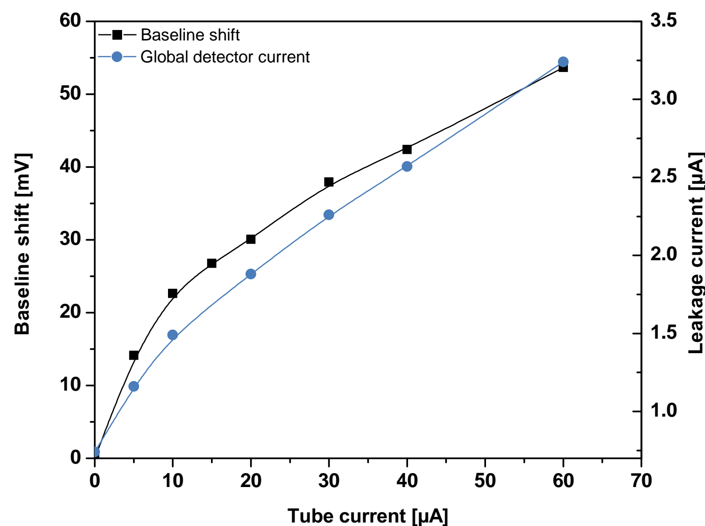

Fig. 7.9: Quantitative analysis of the baseline shift and the sensor current in CdTe (CdTe11) at standard settings. The baseline shift mirrors the behavior of the global detector current under irradiation. Hence, the photon flux dependent additional current in the samples is the likely origin of the baseline shift. The measurement was performed at 90 kVp and at 6.5 cm focal spot to detector distance.

detector current, it can be inferred that the baseline shift is dominated by the photon-flux dependent additional DC-current component in the CdTe sensors (see section 6.1.3). The large difference between CdTe and CdZnTe is therefore the consequence of the very different leakage current behavior.
In summary, the CdZnTe sensors offer a significantly better counting performance than the CdTe ones with respect to the maximum rate (low leakage current) and noise induced breakdowns of the count rate (no baseline shift observed).

7.1.2 Integrator dynamic range

This section concludes the discussion of the dynamic range in terms of the integrator linearity. For this assessment, the integrator current was measured as a function of the X-ray tube current during 3 ms frame intervals (see Fig. 7.10). The linearity was quantified by fitting the integrator data and calculating the relative residuals of the fit with respect to the measurement data. The residuals in Fig. 7.10 show that the deviation of the measured integrator current from the fitted linear relation is 0 % on average with a relative standard deviation of 1.3 %. The maximum deviation of approximately 2.5 % is observed at the smallest input current (36 pA).
This result has to be compared to the relative residuals, which were measured in the *ILeakSim* constant current measurements in Fig. 4.3.2. In that case the currents were not routed through the feedback but directly to the integrator. Even without the additional influence of the feedback, the system yielded relative residuals of approximately 8 % at 4 nA.
Hence, the linearity measurement in Fig. 4.3.2 was limited by that of the *ILeakSim* current source. So, assuming that the X-ray tube generates a photon flux, which scales linearly with the tube current, Fig. 7.10 implies that the integrator achieves a very good linearity under measurement conditions.

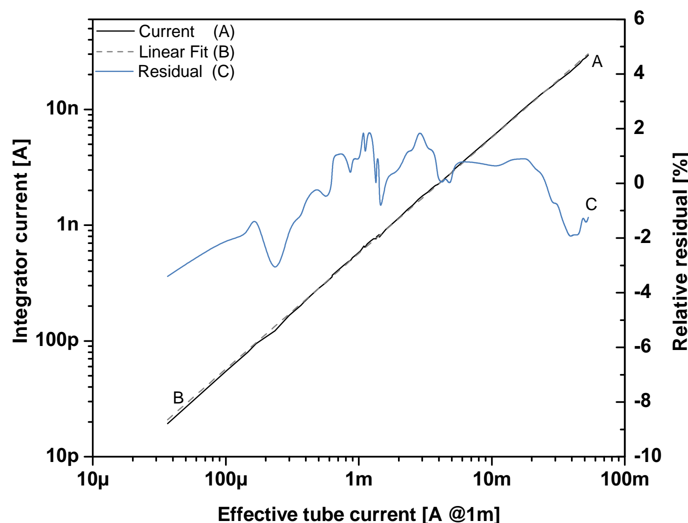

Fig. 7.10: Integrator linearity under X-ray irradiation measured with a CdZnTe module (CZT04) at standard settings. The measured data were fitted with a linear function and the relative residuals calculated (right axis). On average the measured relative residuals are zero and the relative standard deviation of these residuals is 1.3 %. The measurement was performed at 90 kVp and at varying focal spot to detector distances.

7.2 Noise

A second advantage of the CIX 0.2 system, apart from the large dynamic range, is the high correlation between the photon counter noise and the integrator noise. In order to assess this quality, the noise of both channels will be evaluated individually before discussing the performance of the joint signal processing concept.

7.2.1 Counter noise

Fig. 7.11(a) shows the measured and simulated photon count rate fluctuations under homogeneous X-ray irradiation with a 90 kVp spectrum. The measurement data for the CdZnTe and Si modules (solid lines) were obtained by step-wise increasing the photon flux and sampling the photon rate 100 times at each flux. Calculating the standard deviation of these 100 individual measurements per pixel and averaging over all 64 pixels yields the photon number fluctuations.
The first observation is that the results for the Si (Si03) and the CdZnTe (CZT04) modules agree very well. This is to be expected as the photon noise is displayed as a function of the photon rate. Therefore the different absorption spectra (see section 6.4.3) have no influence on this plot.
Apart from the measurement data, Fig. 7.11(a) also includes a simulation of the quantum noise ($\sqrt{n}$). In detail, the simulation is based on the assumption that the impinging X-ray spectrum can be replaced by a number of monoenergetic (30 keV), Poisson-distributed pulses, which deposit exactly the same amount of charge inside the detector in a 3 ms frame as the original spectrum. The 30 keV photon energy was chosen, because it reflects the average photon energy in the absorption spectrum measured with a CdZnTe detector. Comparing simulation and measurement, it can be seen that the measured photon number fluctuations below 1 Mcps input rate are very close to the expected values. The difference

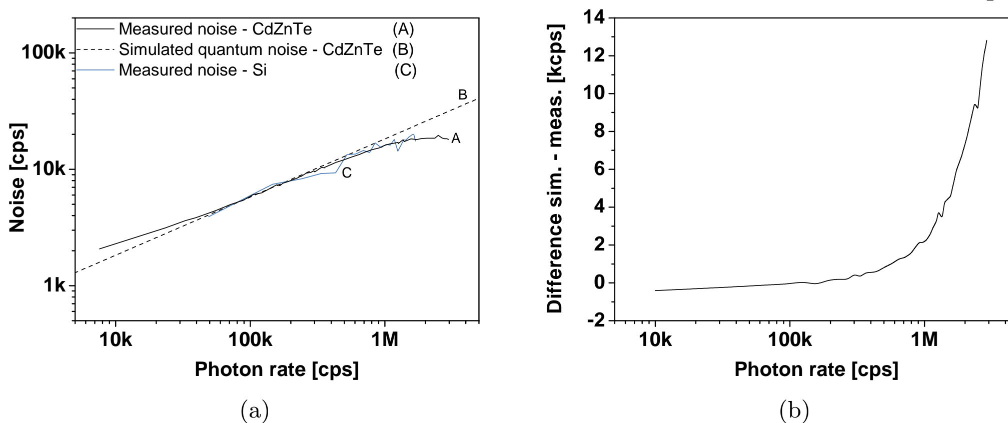

(a) (b)

Fig. 7.11: (a): Simulated and measured photon rate fluctuations as a function of the measured photon rates in a CdZnTe (CZT04) and a Si (Si03) module at standard settings. The noise measurement is based on 100 consecutive samples of the photon rate at a given tube setting and a subsequent calculation of the standard deviation of these 100 individual data points. (b): Difference in cps between simulated and measured noise in the CdZnTe module. The tube was operated at 90 kVp. The simulation data were obtained by assuming a monoenergetic 30 keV, Poisson-distributed spectrum. The photon rate was set such that this simplified, monoenergetic spectrum deposits the same amount of charge as the original tube spectrum.

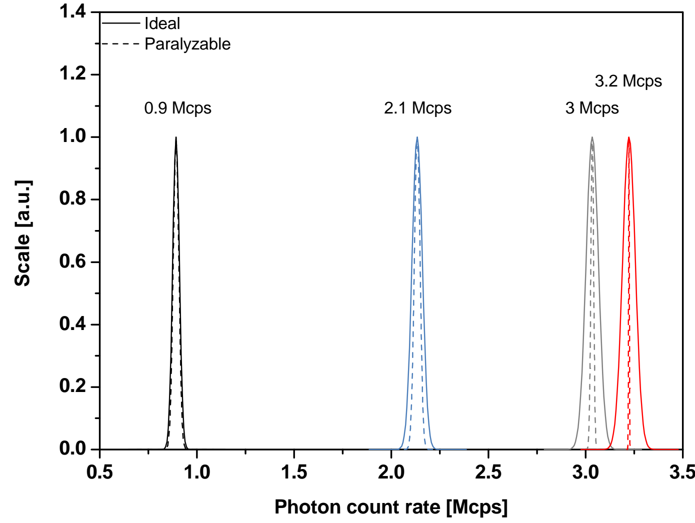

Fig. 7.12: Simulated photon fluctuations at three different measured count rates for an ideal counter (solid lines) and a paralyzable counter (dashed lines). Note the decreased standard deviations as well as the asymmetry of the distributions in case of the paralyzable counter. These two features are an effect of the shallow measured versus true count rate relation at high rates (see section 3.3.1).

between simulation and measurement (see right axis of Fig. 7.11(a)) increases slightly from 400 cps at 10 kcps input rate up to 1 kcps deviation at a rate of 600 kcps.
Beyond this input rate the measured fluctuations are significantly smaller than the simulated ones and the difference increases rapidly. This can be understood by considering the counter behavior at high rates. Assume for example, that the system is exposed to a train of Poisson-distributed 30 keV pulses at a rate N_{True}. This means that n_{True} photons are hitting the detector during the frame duration t_{Frame}.

$$n_{True} = N_{true} \cdot t_{Frame} \tag{7.2}$$

The expected statistical fluctuation of the photons per frame can be obtained from:

$$\sigma(n_{True}) = \sqrt{n_{True}} \tag{7.3}$$

The solid lines in Fig 7.12 show the resulting statistical fluctuations of the photon rate for a 3 ms frame at four different rates N_{True}. Returning to a real, paralyzable counter the measured rate N_{Meas} at a given input rate N_{True} is described by (compare (3.2)):

$$N_{Meas} = N_{True} \cdot exp\left(-\frac{N_{True}}{N_{Max}}\right) \tag{7.4}$$

It can be concluded that, due to the paralyzable operation of the counter, the detected photon flux does not follow the Poisson statistics any more and therefore the statistical variance is reduced (see dashed lines in Fig. 7.12). Furthermore, this also means that the counter is going to react differently to an increase in the number of photons per frame than to a decrease. In other words, the distribution becomes asymmetric. At the end of this section Tab. 7.4 summarizes the observed measured and simulated signal-to-noise ratios at a few measured photon rates.

SNR	10 kcps	100 kcps	500 kcps	1 Mcps	3 Mcps
Sim.	5	17	39	55	95
Meas.	5	17	41	61	166

Tab. 7.4: Signal-to-noise ratios (SNR) at different measured photon rates n_{Meas} for the aforementioned simulation and measurement data (3 ms frames). The data represent the average of all 64 pixels of the CIX 0.2 ASIC. The SNRs of the measurement increase with respect to the simulation as the limited maximum count rate affects the photon rate fluctuations.

7.2.2 Integrator noise

The integrator noise measurement follows the same principle as the determination of the count rate fluctuations. This means that the chip-wide average of the standard deviation of 100 successive frames is taken as a measure for the signal variations at a given integrator current. The resulting data are displayed in Fig. 7.13. They show that the Si (Si03) module has a slightly higher noise than the CdZnTe (CZT04) detector. This is contrary to expectation because the noise is displayed as a function of the integrator input signal. At a given integrator current the signal in a Si module consists of more photons due to the lower average energy of the absorption spectrum and therefore the total statistical fluctuations should be smaller. However, as the Si module suffers from a low bump yield this deviation is likely the result of a worse electrical performance of this particular module. In addition, Fig. 7.13 illustrates that above 1 nA the simulated quantum noise (see previous section) and the measured fluctuations in CdZnTe are in good agreement. Below 1 nA a significant deviation due to a constant noise floor of approximately 10 pA can be identified.

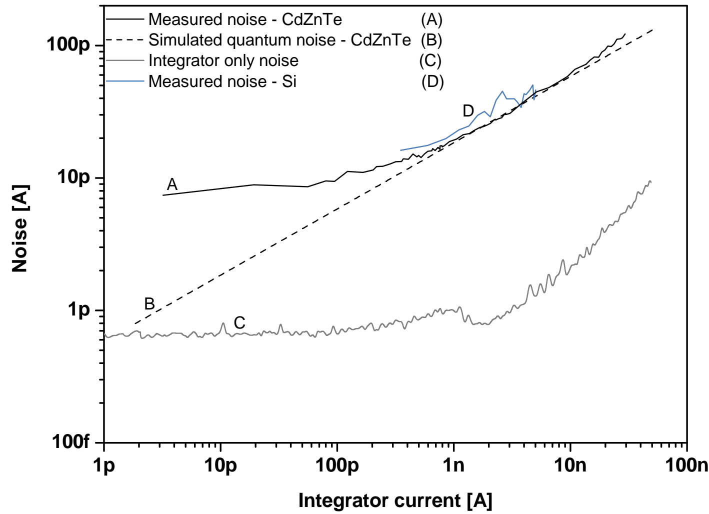

Fig. 7.13: Simulated and measured integrator current fluctuations as a function of the measured integrator currents in a CdZnTe (CZT04) and a Si (Si03) module at standard settings. The noise measurement is based on 100 consecutive samples of the photon rate at any given tube setting and a subsequent averaging of the standard deviations of these 100 individual data points over all pixels. The tube was operated at 90 kVp and varying focal-spot to detector distances. The simulation data were obtained by assuming a monoenergetic 30 keV, Poisson-distributed spectrum. The rate was set such that this simplified spectrum deposits the same amount of charge as the original tube spectrum.

This floor has two major noise contributions, namely:

- Integrator noise at 3 ms frame duration with $IntBiasI$: 0.7 pA
- Feedback noise without leakage current compensation: 5 pA

A quadratic addition of these noise terms (approx. 5 pA) is in reasonable agreement with the measured value of the noise floor (7.3 pA). Above approximately 100 pA input signal, the quantum fluctuations gain significance as indicated by the increase in the measured integrator noise.
In order to compare these results with the electrical performance of the ASIC presented in section 4.4.2, Fig. 7.13 contains a copy of the integrator noise measurement at identical settings, i.e. 3 ms frame duration with an additional $IntBiasI$ bias current. It can be seen that the shape of the curve in the electrical tests matches the one of the X-ray measurement with the difference that the noise is approximately a factor 10 smaller. Note that the electrical tests were performed without using the feedback, whose current noise (5 pA) accounts for almost 70 % of the noise at small input signals under irradiation (7.3 pA). The observed increase in the system's noise due to the feedback is also supported by measurements on unbumped ASICs. It was reported that routing the integrator input signals through the feedback increases the integrator noise by a factor of 3 - 5 [1].
Hence it can be concluded that the integrator behaves as expected. An overview of the integrator's signal-to-noise performance is given in Tab. 7.5.

SNR	10 pA	100 pA	1 nA	10 nA	30 nA
Sim.	6	17	54	171	300
Meas.	1	10	51	163	244

Tab. 7.5: Simulated and measured signal-to-noise ratios (SNR) at different measured integrator currents. The data represent the average of all 64 pixels of the CIX 0.2 ASIC.

7.2.3 Noise correlations

Section 2.6 introduced the principle of dual energy imaging, which can be used in order to reconstruct the photoelectric and the Compton component of the photon-matter interaction. This approach requires two spectroscopically distinct measurements for the material basis decomposition. Depending on the detector concept, these two measurements are either obtained subsequently or simultaneously. Considering these different approaches, it is evident that in the simultaneous data acquisition, statistical fluctuations in the photon beam lead to correlated fluctuations in both data sets. In contrast to this, subsequent measurements show no correlation. As detailed in [50], the positive correlations in the simultaneous data acquisition are beneficial for X-ray imaging since they can be used to reduce the image noise.
It was therefore analyzed wether the CIX 0.2 counter and integrator data are indeed correlated and how strong these correlations are. For this, a series of 1000 simultaneous counter and integrator measurements under X-ray irradiation at various discriminator threshold settings have been performed. The X-ray tube was operated at an acceleration voltage of 90 kV, a current of 50 μA and a focal spot to detector distance of 12.5 cm. Long-term variation in the detector signals were kept to a minimum by starting the measurement only after the detector had already been irradiated for 100 s.
Fig. 7.14 shows the resulting correlation plot of the counter and integrator noise. In both cases, the average count rate or the average integrator current have been subtracted such

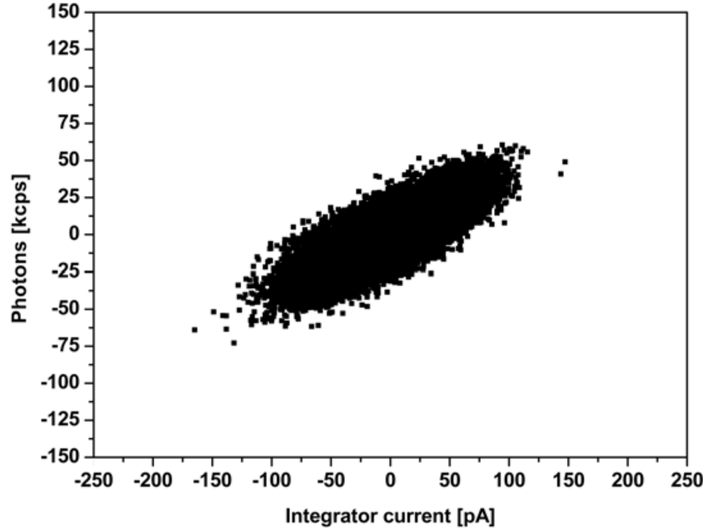

Fig. 7.14: Correlation plot of the photon counter and integrator fluctuations under X-ray irradiation measured with a CdZnTe module (CZT04) at standard chip settings. The average photon rate and integrator current were subtracted from the data in the figure. The measurement was performed at 90 kVp, 50 μA and at 12.5cm focal spot to detector distances. The discriminator threshold was set to 10 keV.

that the data in the figure illustrate the variations between successive measurements. A numerical measure for the correlation between the photon rate N and the integrator current I can be obtained from the correlation coefficient κ.

$$\kappa = \frac{cov(N, I)}{\sigma(N) \cdot \sigma(I)} \tag{7.5}$$

The term cov refers to the covariance of N and I and σ represents the standard deviation of the same variables. Based on this definition, Tab. 7.6 summarizes the correlation coefficients measured at five different counter threshold settings. The table shows that the coefficient drops from 0.79 at 10 keV threshold to 0.44 at 50 keV threshold. This implies that the integrator and counter measurements are highly correlated at low thresholds. The reduction of the correlation coefficient at higher thresholds is explained by the fact that a higher threshold automatically reduces the chance that a fluctuation, which is registered by the integrator, is also seen by the counter.

Discriminator threshold [keV]	κ	$\sigma(\kappa)$
10	0.79	0.04
20	0.77	0.06
30	0.68	0.05
40	0.55	0.06
50	0.44	0.06

Tab. 7.6: Average and standard deviation σ of the correlation coefficient κ of the counter and integrator data of all 64 CIX 0.2 pixels. The data were obtained at 90 kVp, 50 μA and at 12.5cm focal spot to detector distances for different threshold settings.

7.3 Average photon energy

The third key feature of CIX 0.2 is its ability to measure the average energy of the absorbed spectrum. In order to evaluate this characteristic, the average photon energy reconstruction was tested on a homogeneous wedge-shaped aluminum absorber. Like this it is possible to exactly simulate the transmission spectrum behind the absorber as well as the resulting absorption spectrum in the detector. The simulation used for this purpose is the same as in section 6.4.
Fig. 7.15 shows the average photon energy behind the absorber as a function of the Al thickness for a Si (a) and a CdZnTe (b) module. The two plots contain simulation data as well as measurement results.
Starting with the simulations, the topmost curves in Fig. 7.15 show the simulated average photon energy of the transmission spectrum behind the Al absorber. In this context the term average energy is defined as the average energy of those photons with energies above 10 keV. The 10 keV lower limit reflects the fact that the impinging X-ray spectrum does not contain any photons below this value due to the filters installed in the X-ray setup (see simulated tube spectrum in Fig. 6.24). The definition furthermore gives a measure of the average energy, independent of the large number of low energy hits introduced by charge sharing and electronic noise. In a perfectly absorbing sensor, these average photon energies should be reproduced by the measurement. However, it has been mentioned before that Si suffers from a low X-ray absorption coefficient at higher X-ray energies. The low X-ray absorption of the Si sensors is reflected by the triangular data markers in Fig. 7.15(a)

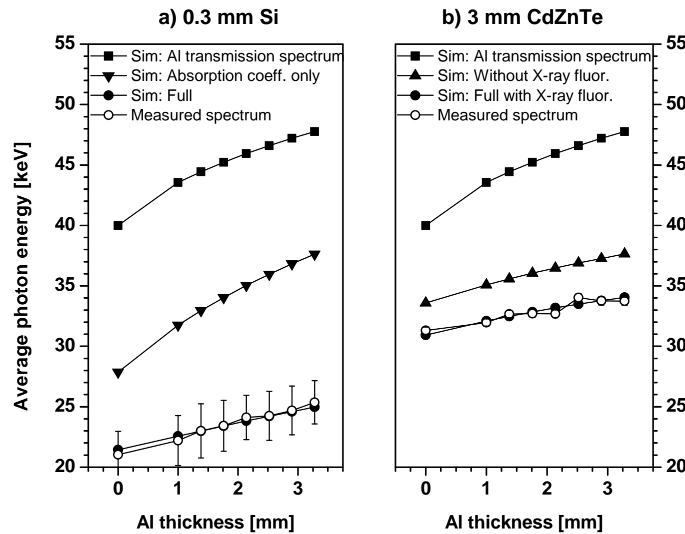

Fig. 7.15: Average simulated (filled symbols) and measured (open symbols) photon energy reconstruction measured on an Al-absorber of varying thickness. (a): 300 μm Si sensor (Si03). (b): 3 mm CdZnTe sensor (CZT04). The modules were irradiated at a focal spot to detector distance of 12.5 cm, a tube endpoint energy of 90 keV and tube currents of 100 μA and 50 μA for Si and CdZnTe, respectively. In the simulation, photons with energies below 10 keV have been ignored in order to be independent of charge sharing and detector effects like electronic noise. The measured average energies were calculated from the deposited charge (integrator) and the number of detected photons (counter) obtained at standard chip settings. For Si and CdZnTe two different constant scaling factors are used to reduce the integrator current and thereby correct for the low energy hits registered by the integrator. The error bars show the error of the module-wide average.

corresponding to the "*no interpixel coupling*" data in Tab. 7.7. If interpixel coupling is included into the simulation, the average photon energies are further reduced, e.g. instead of an average energy of 47.8 keV the Si simulation only yields 25 keV behind 3 mm of Al. A very similar situation arises for the CdZnTe detectors where the average photon energy is reduced from 47.8 keV to 34 keV. However, due to the fact that these sensors absorb the impinging X-ray spectrum almost completely, the shift of the average photon energy is not as large as in Si. The impact of X-ray fluorescence on the average photon energy can also be identified in Fig. 7.15(b). Owing to the relatively high energetic K-edges of Cd and Te, this effect reduces the average photon energy in the discussed example by another 3 keV. This amounts to approximately 7 % of the average energy of the impinging transmission spectrum. X-ray fluorescence therefore introduces a significant change in the absorption spectrum of a CdTe or CdZnTe sensor.
These simulations have to be compared with the average photon energy as measured with CIX 0.2. Section 3.1 stated that a simultaneously counting and integrating detector can measure the average photon energy according to the following formula:

$$\overline{E} = \frac{I_{Int} \cdot E_{e/h}}{N_{Photons} \cdot t_{Frame}^{-1} \cdot e} \tag{7.6}$$

It is important to note that with this formula, the measured average photon energy is generally overestimated compared to the aforementioned simulation. The reason for this is that the low energy charge sharing events are registered by the integrator but at the same time they are ignored by the photon counter due to the applied 10 keV threshold. Hence, both the Si and the CdZnTe measurement data have been corrected by constant scaling factors which reduce the measured currents. These two scaling factors were determined empirically by averaging the measured integrator currents at different absorber thicknesses and dividing the result by the respective average of the simulation results. The problem with this normalization is that the scaling factors are influenced by the imaged object. It is evident that the number of low energy entries below 10 keV depends on the impinging spectrum. Thus, a quantitatively correct reconstruction of the average energy of the absorber spectrum requires the precise knowledge of the material composition of the absorber. Alternatively, it would be necessary to calibrate the detector results with various absorber materials and to use a look-up table to link the measured data to the correct average photon energies.
Fig. 7.15 shows that by using constant scaling factors for Si and for CdZnTe, it is pos-

Si		
Simulation type	E (0 mm) [keV]	E (3 mm) [keV]
Transmission only	40.0	47.8
No interpixel coupling	27.9	37.6
Full	21.4	25.0
CdZnTe		
Simulation type	E (0 mm) [keV]	E (3 mm) [keV]
Transmission only	40.0	47.8
No X-ray fluorescence	33.6	37.6
Full	30.9	34.0

Tab. 7.7: Simulated average photon energies in a CIX 0.2 Si and a CdZnTe sensor with and without an additional absorber 3 mm thick Al absorber. The different simulations are described in the text.

sible to reproduce the simulation results. The important point of this measurement is that the relative changes in the average photon energy introduced by the absorber are in good agreement with the simulation. This implies that when imaging an unknown object, CIX 0.2 is not able to determine the absolute value of the average photon energy but it still reproduces relative changes correctly.
The relatively large errors in the Si data in Fig. 7.15 compared to CdZnTe are caused by the low bump yield of the Si module as all data points are average values over the CIX pixel matrix.
The aforementioned results prove that despite the influence of the detector geometry and the fluorescence properties of the sensors, the average photon energy reconstruction with CIX 0.2 can be successfully performed. Equipped with a CdZnTe module, CIX 0.2 can achieve a relative average photon energy resolution of approximately 0.3 keV at standard chip settings.
The final aspect which remains to be addressed is the dynamic range in which the average photon energy reconstruction is possible and which precision this measurement achieves. Fig. 7.16 shows the result of the average photon energy reconstruction of an unattenuated X-ray tube spectrum with a CdZnTe module (CZT04) in the overlap region between counter and integrator. The average photon energy and its error were calculated based on the data of Figs. 7.1, 7.11(a) and 7.13, i.e. the measured count rates, integrator currents and their respective noise at various photon fluxes. In contrast to the previous measurement no averaging over the whole module was performed and thus Fig. 7.16 illustrates the precision of a single average photon energy measurement with CIX 0.2. It is found that the standard deviation between successive measurements at identical photon fluxes drops below 1 keV if the photon flux at the sensor surface exceeds 350 kcps. At higher photon fluxes the measurement precision improves to approximately 0.4 keV. Nevertheless, if the photon fluxes come close to the maximum count rate of the system, count rate

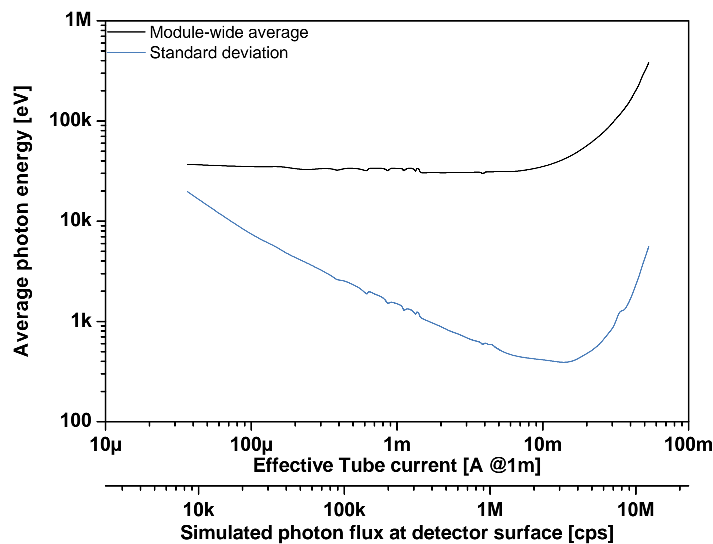

Fig. 7.16: Precision of the average photon energy reconstruction at standard chip settings as a function of the photon flux at the detector surface. The measurement was performed with a 3 mm thick CdZnTe sensor (CZT04) at 900 V bias, an X-ray endpoint energy of 90 keV and at varying tube currents and focal spot to detector distances. Relative measurement precisions better than 3 % are obtained between approximately 350 kcps and 1.7 Mcps.

inefficiencies cause a decrease in the measurement precision. Furthermore the count rate losses of the paralyzable counter introduce a systematic error in the average photon energy reconstruction. Significant changes (> 10 %) in the average photon energy measurement are observed at photon fluxes above 2.4 Mcps.
It can therefore be concluded, that at standard chip settings the optimal photon fluxes for the average photon energy reconstruction (relative precision better than 3 %) are between approximately 350 kcps and 1.7 Mcps.

8. X-ray images

8.1 Raw data and flatfield corrections

When taking an X-ray image with CIX 0.2, the system delivers its information in the form of raw data. Figs. 8.1(a) and 8.1(c) show such counter and integrator raw data, which were acquired simultaneously. The full view of the imaged CIX 0.2 adapter board was reconstructed from 26 x 16 individual snapshots. According to the standard imaging conditions established in the previous chapter, the X-ray tube was operated at 90 kVp with an additional 1 mm Al filter to block the lowest energy photons in the spectrum. The

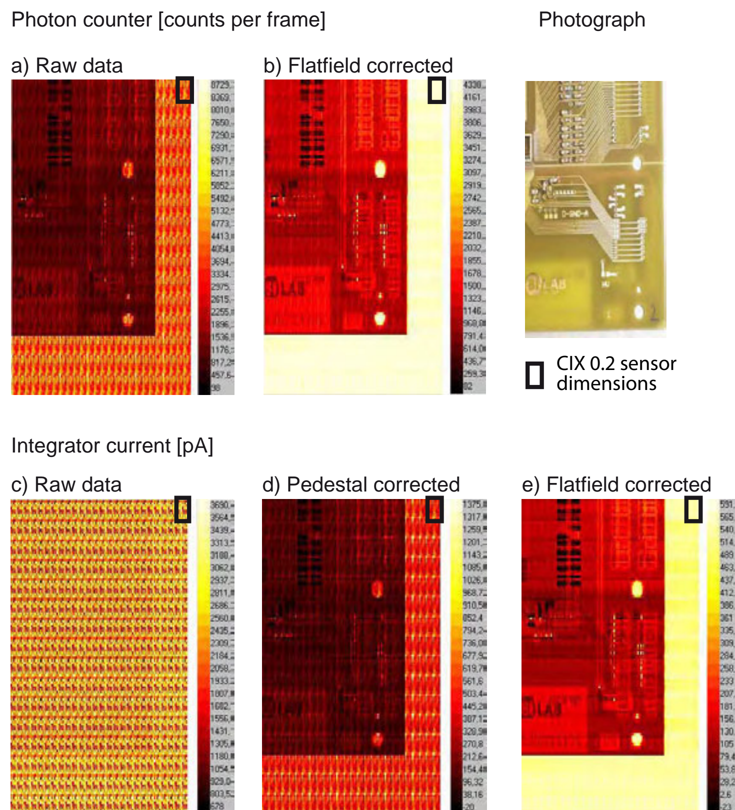

Fig. 8.1: Photon counter (a, b) and integrator (c - e) views of a CIX 0.2 adapter board measured under irradiation with a 90 kVp tube spectrum at 100 μA and approximately 10 cm focal spot to detector distance. The different images illustrate the effects of different image enhancement concepts. Figs. 8.1(a) and 8.1(c) show raw detector data. Only after the subtraction of constant pedestal currents from the integrator data does this channel yield comparable results to the photon counter raw data (see Fig. 8.1(d)). The best images are obtained if a flatfield correction is applied (Figs. 8.1(b) and 8.1(e)). In this example the flatfield corrections were taken under unattenuated irradiation (air calibration). The CdZnTe module (CZT03) was operated at standard chip settings. A reduced bias of 600 V was applied in order to reduce the impact of the bias-dependent long-term variations.

images were taken with a CdZnTe module (CZT03) at a focal spot to detector distance of approximately 10 cm and a counter threshold of 24 keV. Furthermore, in order to reduce long-term fluctuations in the detector signals, the scan was started only after the tube had been operated continuously for 100 s at 100 μA. In this way the initial rapid amplitude changes observed in section 6.2 had already occurred before the 26 x 16 scan was started. It is evident that although the PCB can already be identified in the photon counter, the integrator data do not readily reveal the object. This is because the relatively small signal currents are obscured by the large mismatch currents in the integrator (see section 3.3.6). Hence, the first improvement of the image quality is obtained from an offline subtraction of these pedestal currents (feedback mismatch and leakage current). Fig. 8.1(d) shows the integrator X-ray image after the offset correction. Here, the PCB can clearly be identified, but this image still shows unwanted inhomogeneities.
An effective way of eliminating these inhomogeneities is the application of a *flatfield correction* or *fixed pattern correction*. A flatfield correction is an offline method to increase the detector homogeneity. It is performed by measuring the detector response under homogeneous irradiation. Based on this, a correction factor for each pixel is calculated and stored offline. When scanning an object, the resulting pixel values are multiplied by this correction factor, thereby increasing the homogeneity of the detector response. The major limitation of this method lies in the fact that the correction factors depend on the photon flux and the impinging spectrum. So, when aiming for an optimal result, the flatfield correction has to be performed at irradiation conditions, which are similar to the object that is to be imaged.
Figs. 8.1(b) and 8.1(e) show the effect of a flatfield correction taken at high intensity, i.e. without any absorber between tube and detector. This type of flatfield correction is also called an *air calibration* because the detector's response to the full unattenuated X-ray

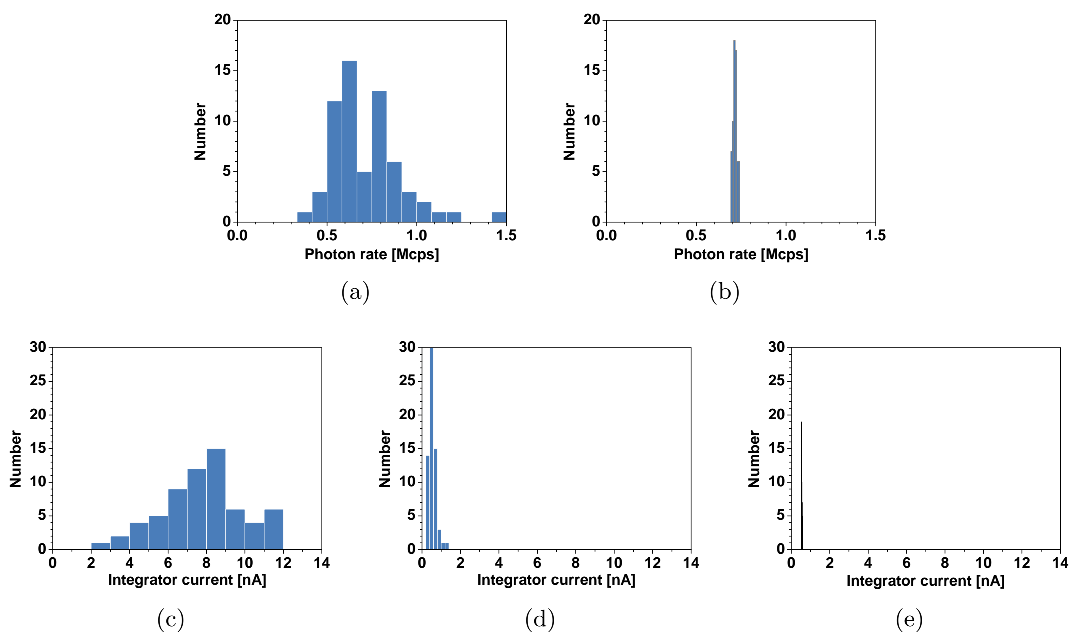

Fig. 8.2: Histograms of the photon counter and the integrator data of 64 pixels under homogeneous, unattenuated irradiation. (a): Photon counter raw data; (b): Photon counter flatfield corrected; (c): Integrator raw data; (d): Integrator pedestal corrected; (e): Integrator flatfield corrected.

beam is sampled and subsequently used to correct the measurement data during the scan. The flatfield corrected photon counter and integrator views illustrate that basically all artifacts are eliminated by this method. In the image the coupling capacitors and even the gold contact pads on the backside of the PCB can easily be identified. The Silab logo on the front is also reproduced in good quality.
The effect of the flatfield correction is quantified by calculating the standard deviation of all 64 of the chip's pixels (see areas marked by the rectangles in Fig. 8.1). Fig. 8.2 shows the resulting distributions and Tab. 8.1 summarizes the averages and the standard deviations. It is found that the flatfield correction reduces the spread between the individual pixel results from approximately 30 % down to roughly 2 %. This proves that despite the inhomogeneities introduced by the sensor (see section 6.3) as well as the ASIC (see section 3.3.6), the corrections lead to a significant improvement of the image quality.

Counter	Raw data	Pedestal corr.	Flatfield corr.
Average	716 kcps	-	716 kcps
Std. dev.	189 kcps	-	11 kcps
Relative. std. dev.	27 %	-	1.5 %
Integrator	Raw data	Pedestal corr.	Flatfield corr.
Avgerage	7.77 nA	547 pA	547 pA
Std. dev.	2.11 nA	187 pA	15 pA
Relative std. dev.	27 %	34 %	2.7 %

Tab. 8.1: Average measurement results and their chip-wide standard deviations in the photon counter and integrator of a CdZnTe module (CZT03) under irradiation. The values were taken inside the rectangular sections of Fig. 8.1. Apart from the raw data, the table also contains the pedestal corrected as well as the flatfield corrected data. For the photon counter no pedestal correction is necessary.

8.2 Beam hardening

Beam hardening in an object is an issue for X-ray imaging because it leads to a systematic underestimation of the absorption coefficient. With its simultaneous counting and integrating approach the CIX 0.2 system can in principle directly measure the beam hardening and indicate the respective regions in an image. Fig. 8.3 illustrates this effect using the example of a copper paper clip. The images were taken with a CdTe module (CdTe10) at 90 kVp tube voltage, 50 μA current and a focal spot to detector distance of approximately 10 cm. Fig. 8.3(a) displays the average photon energies, which were measured on the paper clip. The average energy scale is not normalized and therefore only describes relative changes in the average photon energy. Nevertheless, a significant change in the average photon energy can be observed in the lower left corner, where two of the paper clip's arms overlap.
Furthermore, Fig. 8.3(b) and 8.3(c) contain the flatfield corrected photon counter and integrator images, which were used to calculate the average photon energy. The flatfield correction was performed again on the unattenuated beam such that the homogeneity outside the paper clip is very good. Inside the object, the validity of the flatfield correction factors is reduced because the metal clip causes significant changes in the spectrum and in the signal amplitude. This limitation of the flatfield correction is best seen in the integrator where dark, low current regions can be identified in the metal phantom. The likely reason as to why these artifacts are especially pronounced in the integrator is the

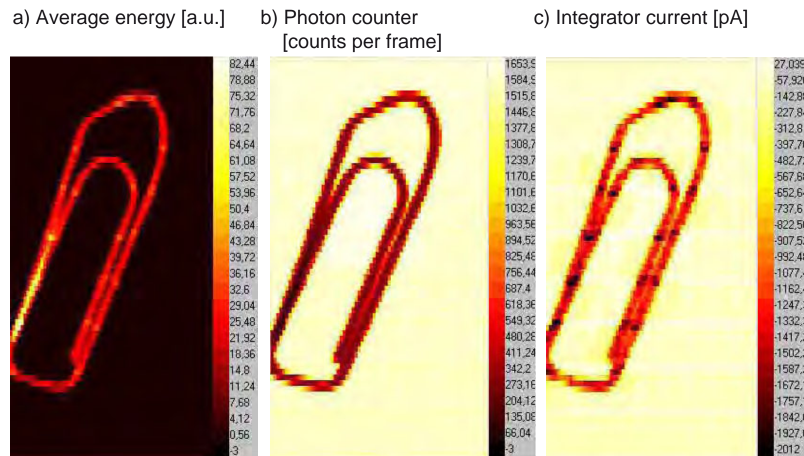

Fig. 8.3: Illustration of beam hardening inside a metal object. The average photon energy image (a) shows the beam hardening in the region where the two arms of the paper clip overlap. Note that the detector data are not calibrated and therefore the average energy is given in arbitrary units (a.u.). The object was imaged with a CdTe module (CdTe10) under irradiation with a 90 kVp tube spectrum at 50 μA and approximately 10 cm focal spot to detector distance. A low bias of 200 V was used in order to reduce the bias-dependent long-term variations. At the same time the reduced bias also guaranteed the best counting performance as it keept the baseline shift caused by the CdTe sensor small. The two other plots show the flatfield corrected photon counter (b) and integrator (c) images, from which the average photon energies were computed.

non-linearity in the signal current, which was discussed in section 6.1.3. As the flatfield correction assumes a linear relation between the photon flux and the resulting signal, it actually underestimates the signal amplitudes at low photon fluxes. Therefore the flatfield corrected signal currents are systematically too low. The effect is more pronounced in some pixels, which results in the regularly appearing dark pixels. In general, this can be remedied by performing the flatfield correction on a homogeneous object with similar absorption properties as the imaged object. However, if both the beam hardening and the amplitude changes, introduced by different regions of a compound object, are very different, a decrease of the image quality cannot be avoided.

8.3 Oversampling

In this section the response of an ideal detector system is emulated and tested. This analysis is based on an 8 x 8 oversampling of the actual X-ray image, which means that the object is scanned 64 times. Each time the start position of the scan is shifted by one pixel and thereby every point in the object is seen by every pixel of the detector. Thus, all remaining inhomogeneities due to different pixel responses are averaged out. A shortcoming of this method is of course that it increases the radiation dose and the scan duration by the number of pixels. While this method cannot be applied in medical imaging, it still offers valuable insights into how future detectors with better sensors could perform.
Fig. 8.4 shows one such oversampled object. The object in question is a human molar featuring a large metal filling in the upper section. Compared to the regular, not oversampled views, the oversampled pictures show a vastly increased image quality. In both the counter and the integrator images the root of the tooth can be identified (see Figs. 8.4(a) and 8.4(b)). Still, the upper part of the tooth in these two images does not reveal any structure because it is encapsulated in a metal filling. A better view can be found in

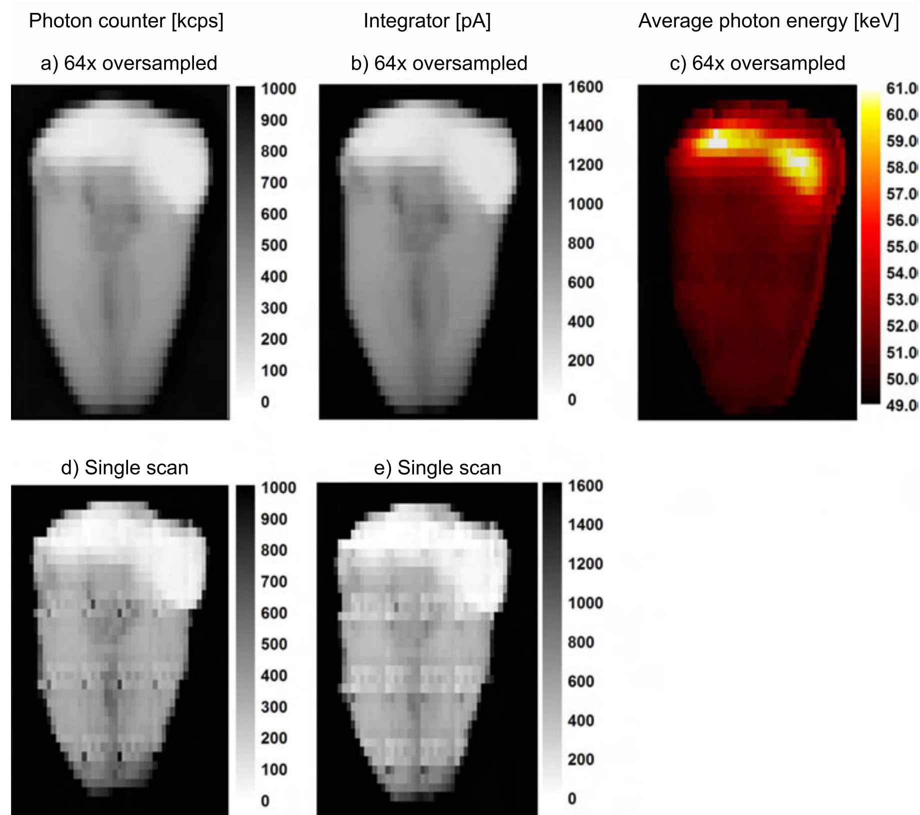

Fig. 8.4: 64x oversampled (a - c) and single scan (d, e) photon counter and integrator X-ray images of a human tooth with a metal filling. Note that the scale is inverted compared to the previous X-ray images. All images are flatfield corrected (air calibration). The images were taken with a CdZnTe module (CZT03) at 90 kVp, 90 μA, a focal spot to detector distance of approximately 10 cm and a reduced bias of 600 V. The average photon energy image (c) is not normalized and therefore only given in arbitrary units (a.u.).

Fig. 8.4(c), which shows the average photon energies (in a.u.). Here, some impression of the shape and thickness of the filling can be obtained. If future sensor crystals can indeed achieve better homogeneities due to less or at least more homogeneously distributed defects, direct converting semiconductor sensors might offer very good imaging capabilities.

8.4 Average photon energy and contrast enhancement

The previous sections showed that with its simultaneously counting and integrating concept, CIX 0.2 is sensitive to relative changes in the average photon energy. At the end of this chapter, a critical assessment of the benefits of the average photon energy measurements in terms of a potential contrast enhancement concludes the treatment of the detector's imaging performance.

On a first glimpse it seems intuitive that the average photon energy channel does not feature a better contrast than the counter or the integrator images from which the average energy is derived. To test this intuitive approach, a low contrast phantom consisting of a 1 mm thick Al sheet and a 10 cm long PMMA[1] wedge with a minimum thickness of 1 mm on one side and a maximum thickness of 20 mm on the other side was fabricated.

[1] Poly(methyl methacrylate)

By placing a different section of the PMMA wedge next to the Al sheet, the contrast in the phantom can be adjusted. Note that because of the similar absorption properties of Al and PMMA to human tissue, this selection of the absorber materials simulates a thin bone (Al) placed next to a thicker muscle (PMMA).
First of all the number of photons per second, the integrator current and the absorbed spectrum behind 1 mm Al and 1 mm to 10 mm PMMA were simulated. The impinging X-ray spectrum in the simulation was chosen such that it corresponds to the spectrum of the Hamamatsu X-ray tube at 90 kVp, including the additional low energy filter consisting of 1 mm of Al. From these simulation data, the image contrast C can be calculated according to the following definition:

$$C = \frac{A_{PMMA} - A_{Al}}{A_{PMMA} + A_{Al}} \tag{8.1}$$

The variables A_{PMMA} and A_{Al} represent the signal amplitudes behind the PMMA wedge and the Al sheet. Fig. 8.5 shows the resulting simulated contrasts. It is evident that the contrast in both counter and integrator has a minimum around (5.5 - 6.0) mm. This is because at approximately 5.8 mm PMMA thickness the integrator measures the same currents behind the PMMA and Al absorbers. At roughly 6 mm PMMA thickness the contrast in the counter vanishes as both absorbers show the same number of photons per second.
Apart from these two graphs, the figure also contains two simulations of the contrast based on the average photon energy. In the simulation labeled "*Avg. energy - Int >10 keV - Cnt >10 keV*" the absorption spectrum above 10 keV was used to calculate the average photon energies. This corresponds to the measurements presented in section 7.3, i.e. a

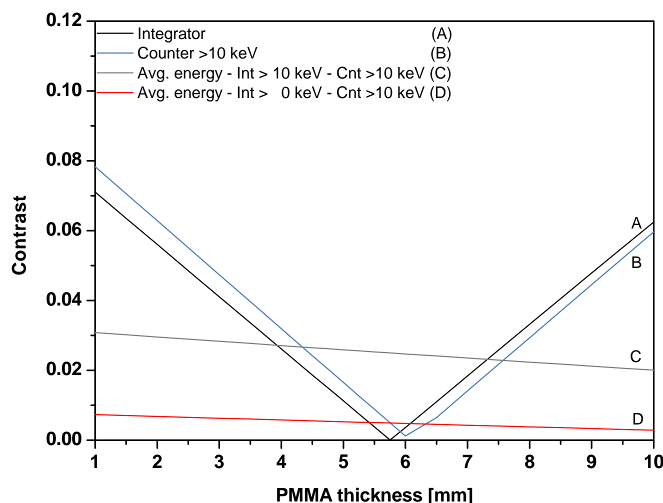

Fig. 8.5: Simulated image contrast in a low contrast PMMA-Al phantom. The phantom consists of a 1 mm thick Al sheet placed next to a wedge-shaped PMMA absorber with thicknesses between 1 mm and 10 mm. The average photon energy contrast was calculated using two different approaches. Once it was derived from the simulated photon spectra with a 10 keV lower threshold to exclude low energy charge sharing hits. The second curve was calculated according to (7.6). At a PMMA thickness of approximately 6 mm the average photon energy measurement should offer a better contrast than the counter or the integrator measurements.

measurement suppressing the large number of low energy photons seen by the integrator. Secondly, Fig. 8.5 also includes a simulation of the average photon energy contrast based solely on the simulated integrator and counter data (*Avg. energy - Int >0 keV - Cnt >10 keV*). This mirrors the direct CIX 0.2 average energy measurement. Both curves show a section in which the average photon energy contrast is better than the contrast in the counter or the integrator alone. Hence, in very special circumstances, the average photon energy measurement can in principle give information beyond that of the two individual CIX 0.2 channels.

This simulation was tested on the PMMA-Al phantom (see Fig. 8.6). Figs. 8.7(a) and 8.7(b) show flatfield corrected images of the low contrast phantom taken simultaneously with the counter and the integrator of a CdZnTe module (CZT04) at 600 V bias and a tube voltage of 90 kV. The frame duration was 6 ms. The Al sheet can be identified in the upper part of the image next to a small section without any absorber ("air"). In the

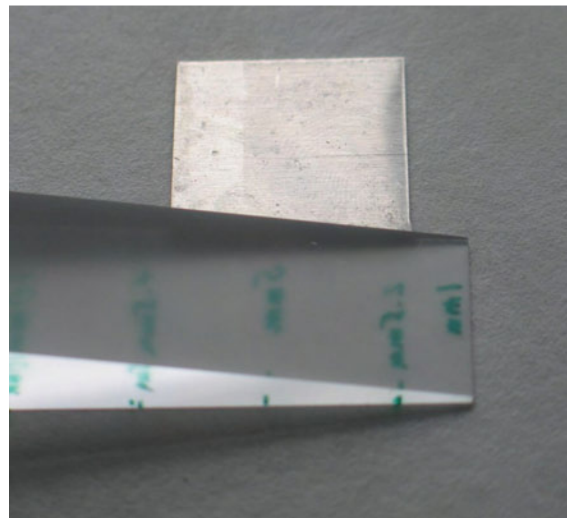

Fig. 8.6: Photograph of the PMMA-Al low contrast phantom.

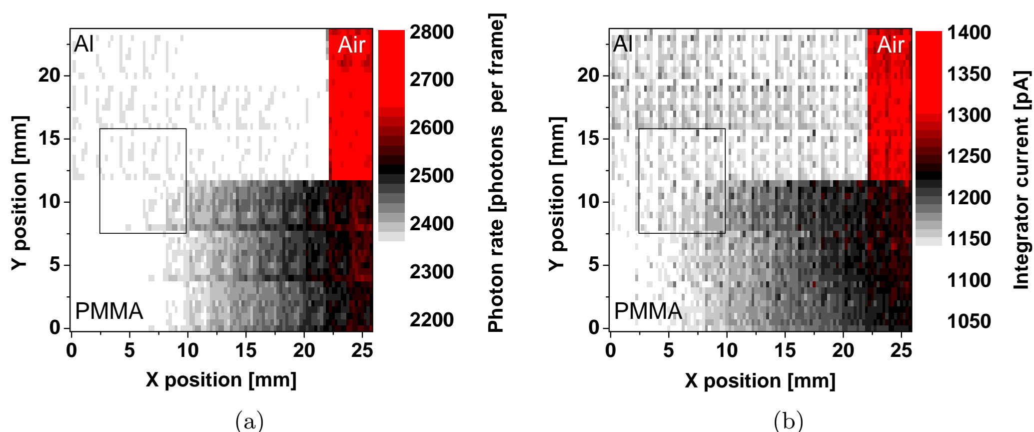

Fig. 8.7: Photon counter (a) and integrator (b) views of a low contrast PMMA-Al phantom taken with a CdZnTe module (CZT04) at 600 V bias and a tube voltage of 90 kV. The tube current was set to 50 μA and the focal spot to detector distance was 16.5 cm. The rectangular marker indicates the region in which the image contrast vanishes. This position corresponds to a thickness of the PMMA wedge of approximately 6 mm.

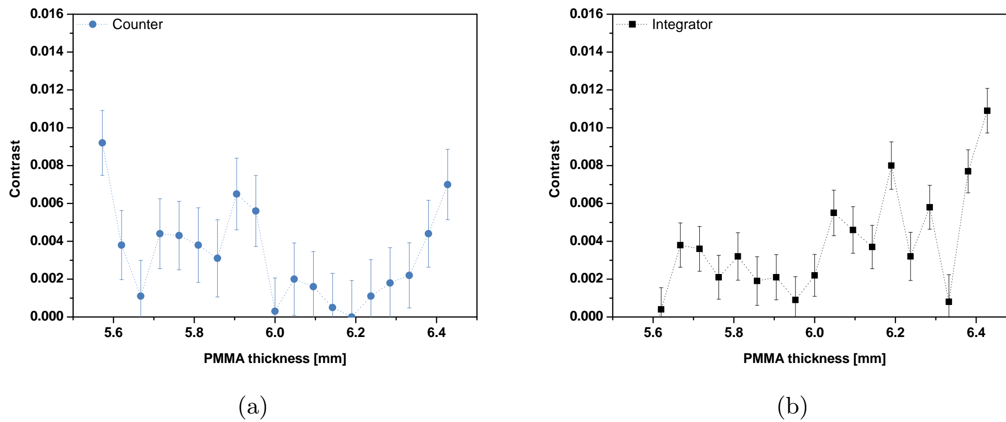

(a) (b)

Fig. 8.8: Measured average photon counter (a) and integrator (b) image contrast of a 1 mm Al sheet placed next to a wedge-shaped PMMA absorber. The measurements were performed with a CdZnTe module (CZT04) at 600 V bias, a tube voltage of 90 kV, 50 μA and a focal spot to detector distance of 16.5 cm. The data points show the average of 100 consecutive measurements. Accordingly the error bars indicate the error on the average.

figures, an x-position of approximately 7 mm corresponds to a thickness of the PMMA wedge of roughly 6 mm. At exactly this position, the image contrast between PMMA and Al vanishes (see rectangular markers in Figs. 8.7(a) and 8.7(b)).
Figs. 8.8(a) and 8.8(b) show the measured contrast in the rectangular sections of Figs. 8.7(a) and 8.7(b), respectively. Note that these values represent the average over 100 subsequent measurements, i.e. at each position the count rate and integrator current were measured 100 times. The error bars show the error of the average value instead of the standard deviation of the 100 successive measurements. The averaging is necessary as a contrast of 0.005 implies for example a difference in the recorded photon number of only 1 % between PMMA and Al. So for the quantum fluctuations to be smaller than 1 % at least 1.7 Mcps (10,000 photons in 6ms) must be registered by the pixels. At this count rate count inefficiencies in the counter start to have an impact on the measurement precision and thus the measurements were performed at only approximately one fifth of the required photon flux. Despite the relatively large error bars, the measurements are in agreement with the

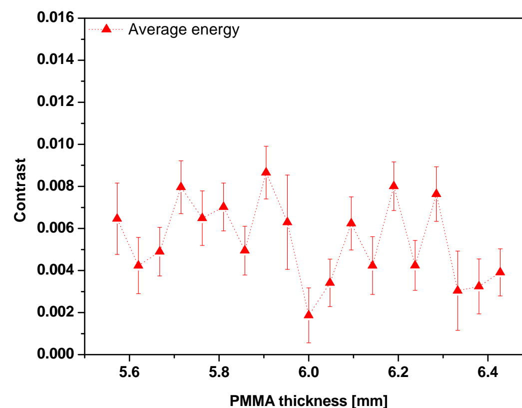

Fig. 8.9: Measured average photon energy image contrast of a 1 mm Al sheet placed next to a wedge-shaped PMMA absorber. The settings are identical to Figs. 8.8(a) and 8.8(b).

simulation, i.e. that the counter and integrator contrast vanishes at PMMA thicknesses of around 5.5 mm to 6 mm. Furthermore, the average photon energy contrast (see Fig. 8.9) is indeed slightly higher than the counter and integrator results but it is generally on the same order of magnitude. These findings prove the validity of the assumptions made in the previous simulation. Furthermore the data also indicate that the average photon energy measurement can in some special circumstances provide an improved image contrast.

9. Conclusion and outlook

9.1 Conclusion

Within this work the first direct converting simultaneously counting and integrating hybrid pixel X-ray detector for high rate X-ray imaging applications has been successfully assembled and characterized. A previous work [1] had already given a very detailed characterization of the ASIC's electrical performance, such that the focus of this work was placed on the description of the module performance under X-ray irradiation. For this a total of 22 CIX 0.2 detector modules were assembled. Out of these 22 modules four were characterized in detail with respect to four different aspects.

Electrical performance

After the successful connection of sensor and ASIC the influence of this sensor connection on the ASIC's electric performance was studied using on-chip test circuits. The following major results were obtained with the best performing module:

- **Maximum count rate:** Typical maximum count rates at the fastest feedback settings, at 0.3 fC discriminator threshold and at 1.4 fC input pulses are approximately 8.5 MHz.
- **Integrator dynamic range:** At standard integrator settings, i.e. 10 MHz integrator clock and 20 fC charge pump size the integrator achieves a linearity of better than 5 % in the range between 10 nA and its maximum input current of 200 nA.
- **Counter ENC:** The counters equivalent noise charge is approximately 300 e^- at maximum feedback settings. This value is roughly 200 e^- higher than the value measured on unbumped ASICs.
- **Integrator noise:** Depending on the duration of a measurement frame, the integrator current noise ranges from 25 pA (50 μs) to 1 pA (3 ms).
- **Discriminator dead time:** A simple estimation of the discriminator dead time at maximum feedback settings yields a value of approximately 70 ns.

Sensor performance

The CIX 0.2 ASIC was connected to different CdTe and CdZnTe sensors. Therefore a detailed analysis of the sensors properties and their suitability for high flux X-ray imaging was performed. At the same time Si n+ in p sensors with their well understood behavior were used as reference devices to qualify the observed effects. Note that the description of the material properties of CdTe and CdZnTe is only a momentary assessment of the quality of the sensors, which were on the market around 2006. Nevertheless, recent publications still show basically identical behaviors of the samples such that it can be concluded that the material quality has not improved significantly until the end of 2008.

- **Sensor leakage currents:** With approximately 350 pA per pixel at 900 V the leakage current in the CdZnTe sensors is roughly a factor 10 smaller than the current in CdTe at identical electric field strengths. The factor 10 is also found in the temperature dependence of the observed leakage currents. Measurements of the photon flux dependent increase in the detector current revealed a non-linear behavior of the CdTe samples. In detail, these sensors show much higher currents than expected. Considering the sensors as a black box, this additional photon flux dependent current can be treated as a photon induced change in the sensor's resistivity.

- **Temporal response:** An analysis of the temporal stability of the detector signals revealed that both CdTe and CdZnTe suffer from variations on a time scale of minutes. These changes are present during and after irradiation and can not be explained by a thermal heating of the sensors. A simple contact model has been applied in order to explain the observed changes based on the accumulation of space-charges and the subsequent modification of the current injection through the electrodes. Keeping computed tomography in mind as a potential application of the CIX detector, the short-term response of the detectors was also evaluated. Tests with a quickly rotating (80 Hz) mechanical beam chopper yield amplitude variations in the CdTe detector current under irradiation on the order of 30 %. Within the measurement precision similar variations could not be observed on the CdZnTe samples, making these the better choice as sensor material.

- **Spatial homogeneity:** Measurements of the CdZnTe module's response to a homogeneous X-ray irradiation revealed standard deviations of the pixel count rates and integrator currents of approximately 40 % with respect to the chip-wide average. It could be established that these variations originate in an inhomogeneous distribution of local defects. These defects change the local electric field through the accumulation of trapped charge and thereby introduce a spatial variation in the effective pixel sizes. In this regard the simultaneous counting and integrating concept produced valuable insights through the normalization of the photon count rate as a function of the integrator current instead of the applied photon flux, i.e. tube current.

- **Spectroscopic performance:** The spectroscopic performance of the system was assessed using a radioactive ^{241}Am source and a 90 kVp tube spectrum. In parallel the sensor response including charge sharing, trapping, X-ray fluorescence and Compton scattering was simulated by [56]. The comparison of measurement and simulation shows the large importance of said interpixel coupling effects for the spectroscopic performance. In detail this means that the average photon energy of the absorbed spectrum is strongly shifted to lower energies. Still, a very good agreement between simulation and measurement in terms of the qualitative as well as the quantitative description is obtained.

Module performance

Apart from this sensor-focussed work, the detector system was evaluated with respect to its three main advantages.

- **Dynamic range:** In CIX 0.2 the combined counting and integrating approach offers a dynamic range of five orders of magnitude. This is achieved by relying on the counter data at very low photon rates and focussing on the integrator measurement

at photon fluxes beyond the counter's maximum limit. At the fastest feedback settings the counter achieves a maximum count rate of 3.3 Mcps, corresponding to a true input rate of 8.8 Mcps. Using 3 ms frames, an integrator clock frequency of 10 MHz, 20 fC charge pump size and routing the signal current through the differential feedback, the integrator can measure currents between 20 pA and 45 nA. The linearity of this measurement is better than 1.3 % in terms of the relative residuals.

- **Noise correlations:** The noise of both the counting and the integrating channel was measured using a 90 kVp X-ray tube spectrum. It is found that the system is quantum noise limited over almost the full dynamic range. The achieved signal-to-noise ratios range from 1 to roughly 200 over the system's dynamic range. In addition to the extension of the dynamic range, the simultaneous measurement of photon rate and current offers the benefit of noise correlations in the two channels. At low (10 keV) threshold settings a correlation coefficient of 0.79 signals a very high correlation between the data. This can be used to increase the image quality in the dual energy imaging method compared to imaging systems which acquire the necessary two views separately [50].

- **Average energy resolution:** The average energy resolution was tested on a homogeneous wedge-shaped Al absorber. The study yields that the system's average energy resolution at standard chip settings is approximately 0.3 keV. Nevertheless, the data also shows that the significant charge-sharing contribution in the absorption spectrum necessitates a normalization of the energy measurement as these low energy hits are mostly below the counter's threshold.

Imaging performance

Finally, a number of X-ray images have been taken. These illustrate the imaging quality that can be achieved with a simultaneously counting and integrating Cd-based X-ray detector at the time of writing. The CIX concept gives a direct handle on the beam hardening, which happens inside an absorber. In principle the average photon energy measurement could even in some cases offer an improved image contrast. However, it has to be determined if this small contrast enhancement has a large impact on medical imaging. Apart from these measurements of the intrinsic properties of the CIX concept, the response of a CdZnTe detector with an ideal, homogeneous response was emulated. This oversampling approach shows the potential image quality that could in principle be obtained with a completely homogeneous sensor sample.

9.2 Outlook

Future steps regarding the simultaneous counting and integrating detector could involve the design of a larger ASIC with a significantly increased number of pixels. This would allow to better evaluate the imaging performance of the system free of the temporal artifacts that are introduced when scanning larger objects. Apart from a correction of the sampling mechanism, which would then permit a real on-chip leakage current subtraction, this future chip should also feature a multi-threshold counter. This would open up new possibilities in terms of contrast agent imaging.

One of the major results of this work is that the available CdTe and CdZnTe sensors introduce many artifacts, which all have to be considered in an imaging application. In

principle a mathematical correction of the sensor's temporal behavior might be possible, but the mathematical and simulation effort might prove to be too large.

Appendix

A. Differential current logic

The digital part of CIX 0.2 is implemented in a low noise current based logic family called differential current steering logic (DCL). This logic concept has been introduced in [59]. In contrast to the widely used CMOS[1] logic it is a differential concept, i.e. instead of using single line signal transmission DCL uses the difference between two lines to carry the signals.
Inherently, this concept produces less cross-talk in mixed analog-digital circuits as interferences cancel out due to the differential nature of the switching. Furthermore, DCL is more robust in terms of common-mode noise as these disturbances do not influence the difference between the two lines but introduce only a common offset. It also has a constant power consumption and does not introduce voltage spikes on the supply lines. This is a problem for CMOS circuits because when these circuits switch between states, both transistors are conducting for a short moment and this current can cause instabilities in the power supplies.
However, the constant power consumption also has its disadvantage as the current flows even when the elements are not switching from one state to another. Furthermore, the design is more complex and therefore demands more space on the chip. Finally, the imbalance between two branches of one such differential pair, caused by the mismatch of the transistors or load circuits can introduce imbalances in the output signals.

[1] "Complimentary metal-oxide semiconductor"

B. CIX 0.2 readout

The readout scheme of CIX 0.2 was designed to allow a continuous readout of the chip even while taking data. In order to achieve this, the chip features a double bank of bus receivers at the end of the 8 pixel rows as well as four readout latches in each pixel cell (see Fig. B.1). When being read out, the values of the photon counter, the pump counter and the time first and time last latches are saved in four 16-bit readout latches at the end of each measurement frame. Depending on the number of latches the user wants to read, some of these latches subsequently get access to the readout bus and for every latch type, the bus receivers take the 8 16-bit words of one row and add a header for the later identification (row address and latch type). The addressing of the individual pixel rows is done via an address sequencer, which activates the bus drivers in the 8 pixel rows. Once the data are stored in the bus receiver, the receiver bank is switched from parallel storage mode to output mode and the data are clocked out serially through 8 LVDS outputs of the chip. At the same time the first memory bank switches from storage to output mode, the second, identical bank switches from output to the storage state and receives the data of the next group of latches. In this way the system can achieve frame rates, which are basically only limited by the frame duration itself, i.e. if operating at a very short frame duration of 50 μs the system can achieve rates of 20 kHz. A detailed scheme of the memory elements and the control signals necessary to operate the dead time free readout is given in [1].

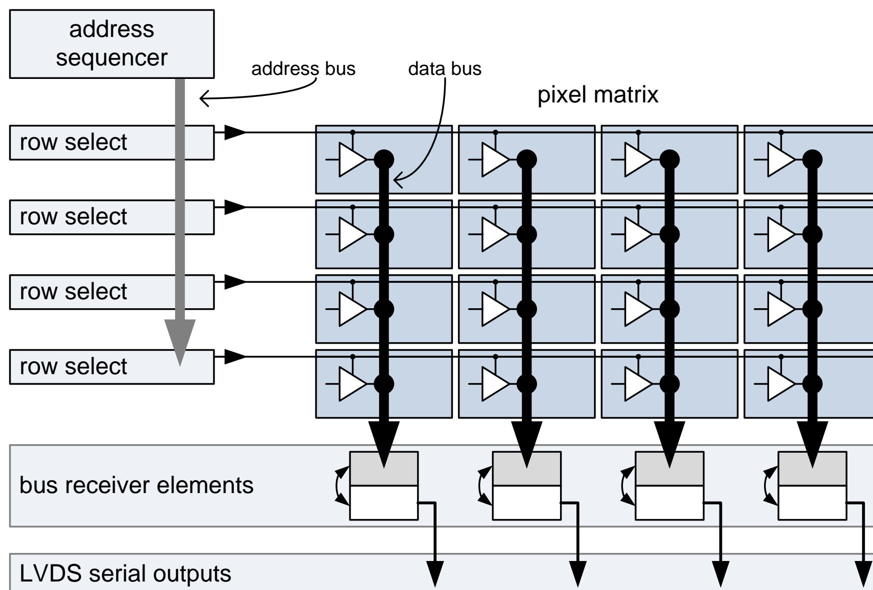

Fig. B.1: CIX 0.2 readout scheme. When enabled by the *row select*, the pixel latches of one row send their contents to one bank of the *bus receivers*. At the same time, the second bank of the receiver elements is read out serially via the LVDS outputs of the ASIC.

C. Threshold scans and tuning

A threshold scan is a basic tool for calibrating the discriminator threshold of a counting detector in terms of the injected charge Q_{Inj}. It is performed by counting the number of hits that are produced by a fixed number of charge packets of constant size Q_{Inj} as a function of the discriminator threshold Q_{Thr}. Ideally the response r to this threshold sweep should be the step-function Θ (see also the dashed line in Fig. C.1).

$$r(Q_{Inj}) = \Theta\left(Q_{Inj} - Q_{Thr}\right) \tag{C.1}$$

The figure shows, that the counter should register every injected pulse (100 % hit probability) up to the point where the amplitude of the preamplifier signals falls below the $V_{CountTh}$ margin. Higher threshold settings should always yield a count rate of zero. The $V_{CountTh}$ value at which the hit probability drops from 100 % to 0 % is called the threshold and it is directly proportional to the injected charge because a larger Q_{Inj} results in a larger signal at the preamplifier output. Like this it is possible to precisely determine at which $V_{CountTh}$ value a certain pixel has to be operated in order to have its threshold at a charge Q_{Inj}. However, as the preamplifier output is modulated by the systems's electronic noise, the response of a real counter deviates from the ideal step-like behavior. Therefore a real threshold curve has an s-shaped form (see solid line in Fig. C.1) and it can be described by a convolution of the ideal step-function and the Gaussian distribution of the electronic noise with the standard deviation σ_{Noise} (shaded area in the plot).

$$\begin{aligned} r(Q_{Inj}) =& \Theta\left(Q_{Inj} - Q_{Thr}\right) \star \frac{1}{\sqrt{2\pi}\sigma_{Noise}} e^{-Q^2/\sigma^2_{Noise}} \\ =& \frac{1}{\sqrt{2\pi}} \int_0^{\frac{Q_{Inj}-Q_{Thr}}{\sigma_{Noise}}} e^{-\frac{x^2}{2}}\, dx + \frac{1}{2} \end{aligned} \tag{C.2}$$

In the case of this so-called Gaussian error function the threshold value is defined as that $V_{CountTh}$ or Q_{Thr} setting at which the hit probability is exactly 50 %.
A further complication of a real counting device is that, because of process variations on the chip as well as slight mismatches in the differential feedbacks, the effective threshold values vary from pixel to pixel. In other words, the pixel thresholds do not coincide with the globally set threshold but show individual deviations. Accordingly, if several untuned counters are exposed to a continuous pulse spectrum, the different thresholds yield different count rates in the pixels since the minimum size for a pulse to be registered varies from pixel to pixel. Therefore it is mandatory to reduce the threshold variations by a method called *threshold tuning*. The threshold tuning procedure entails first determining the individual thresholds of all pixels at a certain pulse size Q_{Inj} and then moving the obtained thresholds closer to the common mean value. For this, CIX 0.2 features a 6-bit *Tune* DAC in every pixel, which can change the globally applied $V_{CountTh}$ discriminator voltage. The step-size of the 6-bit *Tune* DAC is determined by a global *Trim* DAC. Hence, by performing a threshold tuning, the minimum integral charge of a current pulse to be registered with a probability of 50 % is set to Q_{Inj} in all pixels. It has been demonstrated

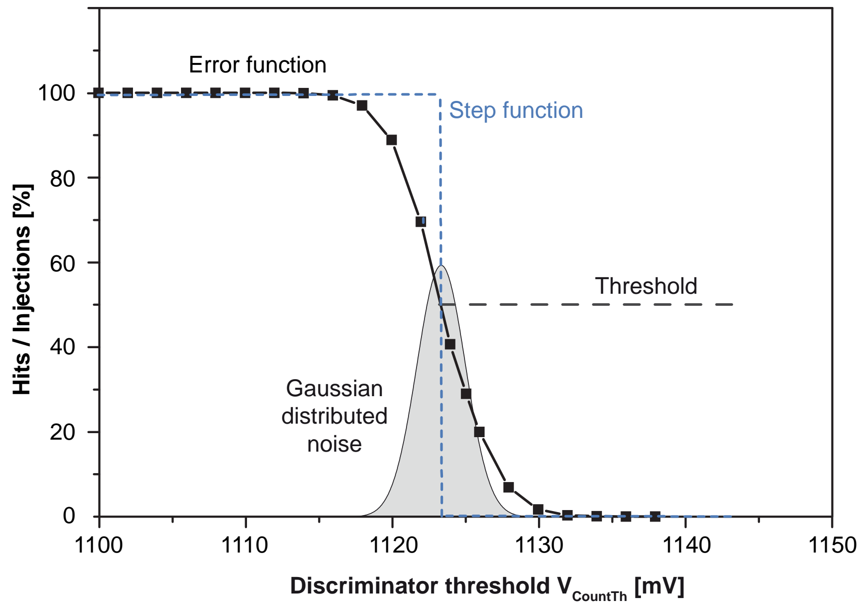

Fig. C.1: Schematic view of a threshold curve. The graph shows the number of registered hits for 100 injections at a fixed pulse size Q_{Inj} as a function of the discriminator threshold. An ideal detector would show a step-like behavior (dashed blue line). However, due to the presence of electronic noise at the preamplifier output, this step function is smeared out, yielding an s-shaped threshold curve (solid line). The distribution of the noise is indicated by the shaded area in the middle of the plot. The threshold lies at the 50 % mark of the error function.

that the threshold tuning can reduce the threshold dispersion in a CIX 0.2 module from 1153 e^- to 36 e^-, which is roughly a factor of 32 [1].

Bibliography

[1] E. Kraft, *Counting and integrating microelectronics development for direct conversion X-ray imaging.* PhD thesis, University of Bonn, 2007.

[2] J. Fink, H. Krüger, P. Lodomez, and N. Wermes, "Characterization of charge collection in CdTe and CZT using the transient current technique," *Nucl. Instr. Meth. A*, vol. 560, pp. 435–443, 2006.

[3] J. Fink, H. Krüger, P. Lodomez, H. Pernegger, P. Weilhammer, and N. Wermes, "TCT characterization of different semiconductor materials for particle detection," *Nucl. Instr. Meth. A*, vol. 565, pp. 227–233, 2006.

[4] M. Overdick, C. Bäumer, K. J. Engel, C. Herrmann, M. Simon, R. Steadman, G. Zeitler, J. Fink, and H. Krüger, "Towards direct conversion detectors for medical imaging with X-rays," *IEEE Nuclear Science Symposium Conference Record, IEEE NSS 2008*, p. 1527.

[5] H. Krüger *et al.*, "CIX - A Detector for spectral enhanced X-ray Imaging by simultaneous Counting and Integrating," *Proc. SPIE*, vol. 6913, 2008.

[6] J. H. Hubbell and S. M. Seltzer, "Tables of X-Ray mass attenuation coefficients and mass energy-absorption coefficients (version 1.4)." `http://physics.nist.gov/xaamdi`, 2009. Database.

[7] W. Heitler, *The quantum theory of radiation.* Clarendon Press, Oxford, 1954.

[8] J. M. Lifschitz and L. D. Landau, *Quantenelektrodynamik. Lehrbuch der theoretischen Physik*, vol. 4. Verlag Harri Deutsch, 7 ed., 1991.

[9] T. Mayer-Kuckuk, *Atomphysik.* Teubner, 1997.

[10] S. Chu, L. Ekström, and Firestone, "The LUND/LBNL Nuclear Data Search." `http://nucleardata.nuclear.lu.se/nucleardata/toi/index.asp`, 1999.

[11] O. Klein and Y. Nishina, "Über die Streuung von Strahlung durch freie Elektronen nach der neuen relativistischen Quantenmechanik nach Dirac," *Z. f. Phys.*, vol. 52, pp. 853–868, 1929.

[12] Philips Healthcare, "Philips DigitalDiagnost product overview." `http://www.medical.philips.com/main/products/xray/products/radiography/digital/digitaldiagnost/`, 2009.

[13] R. Mather, "The next revolution: 256-slice CT." Toshiba America Medical Systems, Inc., 2006.

[14] Philips Healthcare, "Philips Brilliance CT 40-channel product overview." `http://www.medical.philips.com/main/products/ct/products/ct_brilliance_40_channel`, 2009.

[15] "Photograph of an open CT - 2006 model." http://de.wikipedia.org/w/index.php?title=Datei:Ct-internals.jpg, 2006.

[16] C. Guy and D. Ffychte, *An introduction to the principles of medical imaging.* Imperial College Press, 2005.

[17] S. Webb, *Physics of medical imaging.* CRC Press, 2000.

[18] T. Mertelsmeier, "Medical imaging: From data to images." International Workshop on Radiation Imaging Detectors, 2000. Talk.

[19] C. Greskovich and S. Duclos, "Ceramic scintillators," *Annu. Rev. Mater. Sci.*, vol. 27, pp. 69–88, 1997.

[20] Hilger Crystals, "Chemical, physical, optical and scintillation properties of Hilger Crystals materials." http://www.hilger-crystals.co.uk/materials.asp, 2009. Datasheet.

[21] P. K. Soltani, D. Wysnewski, and K. Swartz, "Amorphous selenium direct radiography for industrial imaging," *DGZfP Proceedings.*

[22] Marresearch, "mar555 flatpanel detector datasheet." http://www.marresearch.com/products.mar555.html, 2009. Datasheet.

[23] M. Lachaine and B. G. Fallone, "Monte carlo simulations of X-ray induced recombination in amorphous selenium," *J. Phys. D*, vol. 33, pp. 1417–1423, 2000.

[24] L. Tlustos *et al.*, "Imaging properties of the Medipix2 system exploiting single and dual energy thresholds," *IEEE Trans. Nucl. Sci.*, vol. 53, no. 1, pp. 367–372, 2006.

[25] M. Löcker, P. Fischer, S. Krimmel, H. Krüger, M. Lindner, K. Nakazawa, T. Takahashi, and N. Wermes, "Single photon counting X-ray imaging with Si and CdTe single chip pixel detectors and multichip pixel modules," *IEEE Trans. Nucl. Sci.*, vol. 51, no. 4, pp. 1717–1723, 2004.

[26] E. Kraft, P. Fischer, M. Karagounis, M. Koch, H. Krüger, I. Peric, N. Wermes, C. Herrmann, A. Nascetti, M. Overdick, and W. Rütten, "Counting and integrating readout for direct conversion X-ray imaging: Concept, realization and first prototype measurements," *IEEE Trans. Nucl. Sci.*, vol. 54, no. 2, pp. 383–390, 2007.

[27] K. Spartiotis, J. Havulinna, A. Leppänen, T. Pantsar, K. Puhakka, J. Pyyhtiä, and T. Schulman, "A CdTe real time X-ray imaging sensor and system," *Nucl. Instr. Meth. A*, vol. 527, no. 3, pp. 478–486, 2004.

[28] Z. He, "Review of the Shockley-Ramo theorem and its application in semiconductor gamma-ray detectors," *Nucl. Instrum. Methods A*, vol. 463, pp. 250 – 267, 2001.

[29] L. Rossi, T. Rohe, P. Fischer, and N. Wermes, *Pixel detectors - From fundamentals to applications.* Springer, 2006.

[30] M. Chu, S. Terterian, and D. Ting, "Role of Zinc in CdZnTe Radiation Detectors: Why Zinc? How much?," vol. 51, pp. 2405 – 2411, 2004.

[31] S. A. Soldner, A. J. Narvett, D. E. Covalt, and C. Szeles, "Characterization of the charge transport uniformity of CdZnTe crystals for large-volume nuclear detector applications," *IEEE Trans. Nucl. Sci.*, vol. 51, no. 5, pp. 2443–2447, 2004.

[32] A. E. Bolotnikov *et al.*, “Studies of extended defects in CdZnTe radiation detectors.” IEEE Nuclear Science Symposium Conference Record, IEEE NSS 2008, 2008.

[33] M. Chu, S. Terterian, D. Ting, C. C. Wang, H. K. Gurgenian, and S. Mesropian, “Tellurium antisites in CdZnTe,” *Appl. Phys. Lett.*, vol. 79, no. 11.

[34] R. Tribulet, K. Phan Van, and G. Didier, “Cold traveling heater method, a novel technique of synthesis, purification and growth of CdTe and ZnTe,” *J. Crystal Growth*, vol. 101, pp. 216–220, 1990.

[35] C. Szeles and M. C. Driver, “Growth and properties of semi-insulating CdZnTe for radiation detector applications,” *Proc. SPIE*, vol. 3446, no. 1, pp. 2–9, 1998.

[36] A. Castaldini, A. Cavallini, B. Fraboni, P. Fernandez, and J. Piqueras, “Deep energy levels in CdTe and CdZnTe,” *J. Appl. Phys.*, vol. 83, no. 4, pp. 2121 – 2126, 1998.

[37] T. Takahashi, B. Paul, K. Hirose, C. Matsumoto, R. Ohno, T. Ozaki, K. Mori, and Y. Tomita, “High resolution Schottky CdTe diode for hard X-ray and gamma-ray astronomy,” *Nucl. Instrum. Methods A*, vol. 436, pp. 111 – 119, 1999.

[38] K. R. Zanio, W. M. Akutagawa, and R. Kikuchi, “Transient Currents in Semi-Insulating CdTe Characteristic of Deep Traps,” *J. Appl. Phys.*, vol. 39, no. 6, pp. 2818 – 2828, 1968.

[39] G. Lutz, *Semiconductor radiation detectors.* Springer, 1999.

[40] C. Canali, M. Martini, G. Ottaviani, and K. R. Zanio, “Transport properties in CdTe,” *Phys. Rev. B*, vol. 4, no. 2, pp. 422 – 431, 1971.

[41] J. Fink, “Untersuchungen zur Ladungssammlung in verschiedenen Halbleitermaterialien mittels der ”Transient Current Technique”,” 2004. Diploma thesis - University of Bonn.

[42] G. Prekas *et al.*, “Investigation of the internal electric field distribution on CdZnTe samples under in-situ X-ray irradiation by means of the Pockel’s Effect.” Conference contribution IEEE NSS MIC 2008 conference, 2008. Talk.

[43] D. S. Bale and C. Szeles, “Nature of polarization in wide-bandgap semiconductor detectors under high-flux irradiation: Application to semi-insulating Cd1-xZnxTe,” *Phys. Rev. B*, vol. 77, no. 3, 2008.

[44] T. Takahashi *et al.*, “High resolution Schottky CdTe diode detector,” *IEEE Trans. Nucl. Sci.*, vol. 49, no. 3, pp. 1297 – 1303, 2002.

[45] S. A. Soldner, D. S. Bale, and C. Szeles, “Dynamic lateral polarization in CdZnTe under high flux X-ray irradiation,” *IEEE Trans. Nucl. Sci.*, vol. 54, no. 5, pp. 1723–1727, 2007.

[46] R. Alvarez and A. Macovski, “Energy-selective reconstructions in X-ray computerized tomography,” *Phys. Med. Biol.*, vol. 21, pp. 733–744, 1976.

[47] T. G. Flohr, C. H. McCollough, H. Bruder, M. Petersilka, K. Gruber, *et al.*, “First performance evaluation of a dual-source CT (DSCT) system,” *Eur. Radiol.*, vol. 16, no. 2, pp. 256–268, 2005.

[48] R. Carmi, G. Naveh, and A. Altman, "Material separation with dual-layer CT," *IEEE Medical Imaging Conference Record, IEEE MIC 2005*, pp. 1876–1878, 2005.

[49] E. Roessl and R. Proksa, "K-edge imaging in X-ray computed tomography using multi-bin photon counting detectors," *Phys. Med. Biol.*, vol. 52, pp. 4679–4696, 2007.

[50] E. Roessl, A. Ziegler, and R. Proksa, "On the influence of noise correlations in measurement data on basis image noise in dual-energy like X-ray imaging," *Med. Phys.*, vol. 34, no. 3, pp. 959–966, 2007.

[51] G. F. Knoll, *Radiation detection and measurement.* John Wiley and Sons, 2000.

[52] S. Ebinuma, "Private communication," 2006. Acrorad Jp.

[53] M. Prokesch, D. Bale, and C. Szeles, "Temporal response of CdZnTe detectors under high-flux X-ray exposure." Conference contribution IEEE NSS MIC 2008 conference, 2008. Talk.

[54] S. Ricq, F. Glasser, and M. Garcin, "Study of CdTe and CdZnTe detectors for X-ray computed tomography," *Nucl. Instr. Meth. A*, vol. 458, no. 1, pp. 534–543, 2001.

[55] Y. Du, J. LeBlanc, G. E. Possin, B. D. Yanoff, and S. Bogdanovich, "Temporal response of CZT detectors under intense Irradiation," *IEEE Trans. Nucl. Sci.*, vol. 50, no. 4, pp. 1031–1035, 2003.

[56] K. J. Engel, "Simulation of sensor response." Private communication, 2008. Monte Carlo simulation data.

[57] A. G. Kozorezov, J. K. Wigmore, A. Owens, R. den Hartog, and A. Peacock, "Analytical model for the spatial and spectral resolution of pixellated semiconducting detectors of high-energy photons," *Journal of Applied Physics*, vol. 97, pp. 1–4, 2005.

[58] J. Wiegert, "Simulation of Hamamatsu microfocus X-ray tube spectrum," 2005. Private communication.

[59] P. Fischer and E. Kraft, "Low swing differential logic for mixed signal applications," *Nucl. Instr. Meth. A*, vol. 518, pp. 511–514, 2004.

Acknowledgements

Looking back at my time at the University of Bonn, I would like to thank a number of people without which this work would not have been possible.
First and foremost I would like to thank my PhD supervisor Prof. Dr. Norbert Wermes who on the one hand gave me all the freedom one could want in a research project and at the same time offered valuable guidance for the outcome of this work.
Secondly, I would like to thank my supervisors Dr. Hans Krüger and Dr. Fabian Hügging who supported my research through their helpful advice and who did the proofreading of this thesis.
Furthermore, I would like to thank the X-ray imager group at Philips research in Aachen, who funded my work and who gave me the opportunity to work at the forefront of medical research. Among those, my special thanks belong to Dr. Christoph Herrmann for his constant interest and valuable feedback. I would also like to thank Dr. Klaus-Jürgen Engel and Dr. Jens Wiegert for the simulations of the detector response and the X-ray spectra.
It goes without saying that a project like CIX cannot be handled by a single person. Therefore I would like to thank my colleagues Dr. Edgar Kraft, Dr. Ivan Peric and Manuel Koch who did such a splendid job in designing the CIX ASIC. My special thanks belong to Dr. Edgar Kraft who supervised the CIX activities in Bonn and who handed over a very sophisticated and cleverly designed platform on which I was able to build my work. Thanks for the many ideas and recommendations as well as the many fruitful discussions we had on the tests of our detector!
During this work a number of detector modules were assembled and thus I would like to say thank you to Wolfgang Dietsche and Walter Ockenfels for all their expert work on single die wire and stud bonding.
In general, the five years in the Silab at the University of Bonn would not have been anywhere near as nice without the above and a whole lot of other fantastic colleagues. Thank you guys for the joint but finally futile attempts at solving the world's problems over a cup of coffee, for our shared interest in the fine things they do with barley in Scotland and simply for all the time we spent together!
A special thanks belongs to the people who enabled me to study physics in the first place - my parents and my family. Thank you for everything you did and do!
Last but not least I wish to thank my wife Daniela. Without your constant love and support I could not have done it. Thanks for being the way you are!